

https://dspace.org/

Evaluation of climate model simulations of boundary layers in the Southern hemisphere

Lekoloane, Lesetja Ephraim

2022
https://hdl.handle.net/10539/36969

Downloaded from a DSpace repository. https://dspace.org/



Evaluation of Climate Model Simulations of Boundary Layers in the Southern Hemisphere

by

Lesetja Ephraim Lekoloane

(597635)

Dissertation

Submitted in fulfilment of the requirements for the degree

Master of Science

in

Geography

in the Faculty of Science, University of the Witwatersrand, Johannesburg, South Africa

Supervisor: Prof. Francois A. Engelbrecht

Co-supervisor: Dr Mary-Jane M. Bopape

September 2022

Declaration

I hereby declare that this dissertation is my own unaided and original work except where acknowledged. It is being submitted for the Degree of MSc to the University of the Witwatersrand, Johannesburg. I have not submitted this work before for any degree or examination at any other university.



Lesetja Ephraim Lekoloane

13 September 2022

Date

ABSTRACT

There is a constant need to improve the simulations of weather and climate across different timescales. In this study we evaluate the simulations of Southern Hemispheric boundary layers by a variable-resolution global atmospheric model named the conformal-cubic atmospheric model (CCAM). To do the evaluation, we firstly determine a climatology of present-day ABL attributes from atmospheric soundings at three weather stations located in the high-latitudes (Syowa), mid-latitudes (Marion Island), and subtropical continent (Irene). We then proceed to evaluate how the CCAM simulates attributes of the ABL climatology over the three locations.

Observational radiosonde data indicates that there persistently exists a temperature inversion over Irene at 00h00 UTC, throughout all the months of the year. It was found that this inversion is more intense during the autumn and winter seasons, while it is not as pronounced during the spring and summer seasons. Stability analysis over Marion Island indicated that the near-surface atmosphere is neutrally stratified during all the seasons at 12h00 UTC. The radiosonde data over Syowa also indicated the presence of surface-based inversion at 00h00 UTC for all the months of the year. The surface-based inversion was also observed for 12h00 during all the months except the summer months, May, October and November.

It was also found that monthly variability within the different seasons are prominently observed during the transitional seasons of autumn and spring, especially for thermodynamic variables. An interesting feature which was also observed over Irene and Syowa throughout all the seasons is a bulge in relative humidity above the surface. For Irene this is true for all the months of the year at 12h00 UTC, while for Syowa this bulge is observed for both 00h00 UTC and 12h00 UTC for all the months of the year. It is currently not known why this bulge exists, but a hypothesise is that it is due to the presence of low-level jet (LLJ).

In terms of the model evaluations, it was also found that there is persistent positive bias of moisture variables – dewpoint temperature and relative humidity. This is especially true for the spring and summer months over Irene, while autumn and winter months indicate pronounced negative bias near the surface. Over Marion Island the positive bias of relative humidity is even more pronounced and persists throughout the four seasons at both 00h00 UTC and 12h00 UTC hours. This may be an indicator that the CCAM model is too moist above the surface over the two stations.

Irene ABLH values based on calculations from observations were found to be lower than values simulated by the CCAM at 12h00 UTC throughout the four seasons, with an overestimation of more than 900 m during spring. On the contrary, the CCAM underestimated

ABLH values at 00h00 UTC for all the four seasons over Irene, with differences being only as much as 210 m for the winter season. Over Marion Island, CCAM consistently underestimated values of the ABLH for both 00h00 UTC and 12h00 UTC. An exception occurred at 00h00 UTC during the winter season, which indicates an overestimation of the ABLH by 550 m. Over Syowa, the differences between modelled and observed ABLH were not as pronounced as in both Irene and Marion Island. The smaller differences can be attributed to the presence of the surface-based inversion CCAM depicts fairly well.

ACKNOWLEDGEMENTS

"Soli Deo Gloria"

I wish to express my appreciation to the following persons and organisations, who made the completion of this dissertation possible:

- My supervisors, Professor Francois A. Engelbrecht and Dr Mary-Jane Bopape, for their support, encouragement, patience and guidance during the course of this study. Special thanks to Dr Mary-Jane Bopape for her mentorship and guidance through my early career years.
- My family, and especially my mother, for encouraging me to pursue knowledge from a very young age.
- All thanks to the many new friends from the University of Venda, University of Cape Town, North West University, the CSIR, and the Global Change Institute at Wits University, gained through the SOCCESM project. The many hours we spent trying to motivate each other toward completing our researches kept me going.
- Thanks to the South African Weather Service for allowing me to study, and to the many colleagues who gave me advice when I needed it.
- Special thanks to Karin and Anastasia, librarians at the South African Weather Service, for helping me find many interest articles for this study.
- I would like to also thank and acknowledge the funding from NRF Earth System Science Research Programme, through Grant 118598 "First AfricaN-Based Earth System Model and the Southern Ocean".
- Special thanks to my girlfriend, Asisipo, who agreed to become the wife of my youth during the course of this study. Thank you for the encouragement to keep going, and for allowing me the space to seat behind a computer for very long hours.
- Above all things, I would like to thank God for giving me the strength, health and desire to pursue this study.

TABLE OF CONTENTS

ABSTRACT *3*

ACKNOWLEDGEMENTS *5*

TABLE OF CONTENTS *6*

LIST OF FIGURES *8*

LIST OF TABLES *16*

LIST OF ABBREVIATIONS *17*

CHAPTER 1: INTRODUCTION *20*

1.1. BACKGROUND **20**

1.2. CLIMATE MODELLING AND CLIMATE MODEL DEVELOPMENT **20**

1.2.1. Climate and Earth System Modelling 21

1.2.2. Model Evaluation and the Development of Climate Models in South Africa 22

1.3. INTRODUCTION TO THE BOUNDARY LAYER AND ITS PARAMETERISATION **23**

1.3.1. Boundary Layer Processes 24

1.3.2. The Boundary Layer Parameterisation in Atmospheric Models 25

1.3.2.1. Zero and half-order schemes 26

1.3.2.2. First-order schemes (K-theory schemes) 26

1.3.2.3. 1.5-order schemes (TKE schemes) 26

1.3.2.4. Second and third-order schemes 26

1.3.3. The Boundary Layer Height 27

1.3.4. Overview of Studies on Boundary Layer Simulations in South Africa 27

1.4. AIMS AND OBJECTIVES **28**

1.5. STRUCTURE OF THE REPORT **29**

CHAPTER 2: LITERATURE REVIEW *30*

2.1. INTRODUCTION **30**

2.2. STUDIES OF THE BOUNDARY LAYER AND THE CLIMATOLOGY OF ITS HEIGHT **33**

2.2.1. Convective boundary layers 35

2.2.2. Stable boundary layers 36

2.2.3. ABL height climatology 38

2.3. HOW WEATHER AND CLIMATE MODELS SIMULATES THE BOUNDARY LAYER **40**

CHAPTER 3: ESTABLISHING A PRESENT-DAY SEASONAL CLIMATOLOGY OF ABL ATTRIBUTES IN THE SOUTHERN HERMISPHERE *43*

3.1. INTRODUCTION **43**

3.2. DATA AND METHODS **43**

3.2.1. IGRA 2 Dataset 43

3.2.2. Study Area 44

3.2.3. Deriving Additional Parameters 45

3.2.4. Quality Control Algorithm 47

3.2.5. Vertical Interpolation of the Quality Controlled Data 50

3.2.6. Computation of the ABLH and its Climatological and Seasonal Variability 53

3.3. RESULTS **54**

3.3.1. Irene Station 54

3.3.2. Marion Island Station 72

3.3.3. Syowa Station 89

3.4. SUMMARY OF THE RESULTS 100

CHAPTER 4: EVALUATING THE CCAM IN SIMULATING PRESENT-DAY ABL HEIGHT AND ATTRIBUTES 102

4.1. INTRODUCTION 102

4.2. DATA AND METHODS 102

4.2.1. CCAM Variable-Resolution Global Atmospheric Model 102

4.2.2. Simulating the Boundary Layer with the CCAM 102

4.2.3. Data Post-Processing 106

4.3. RESULTS 106

4.3.1. Irene Station 106

4.3.2. Marion Island Station 116

4.3.3. Syowa Station 124

4.4. SUMMARY OF THE RESULTS 131

CHAPTER 5: SUMMARY AND CONCLUSION 133

5.1. CLIMATOLOGICAL ANALYSIS FROM THE RADIOSONDE OBSERVATIONS 134

5.2. CLIMATOLOGICAL ANALYSIS FROM THE CCAM AND BIAS 135

5.3. A COMPARISON OF BOUNDARY LAYER HEIGHTS FROM SIMULATIONS AND OBSERVATIONS . 136

5.4. RECOMMENDATIONS AND FUTURE WORK 136

LIST OF REFERENCES 138

LIST OF FIGURES

Figure 1.1: The structure of the boundary layer during a typical diurnal cycle, showing different layers present according to atmospheric stability and time of day (Stull 1988, page 11)..... **24**

Figure 2.1: A summary of some major developments in boundary layer research based on literature. The expanded text on some of these is contained in Section 2.1.. .....**30**

Figure 2.2: Schematic of synoptic-scale variation of boundary layer depth between centres of surface high (H) and low (L) pressure. The dotted line shows the maximum height reached by surface-modified air during one hour. The solid line encloses the shaded region, which is most studied by boundary layer meteorologists. (From Stull 1988, page 9) **33**

Figure 2.3: Idealised ABL based on LES. (a),(b) Based on ‘‘Shear’’ and ‘‘Convective’’ ABL figure from Moeng and Sullivan (1994). Shear-driven ABL has neutral stratification; convective ABL has $-z_i/L = 18$. (c) The idealised CBL, which can be traced back to Lilly (1968), is based on the schematic from Conzemius and Fedorovich (2006). In the right panel, the red lines correspond to the idealised mixed layer and the jump atop the mixed layer, associated with the so-called zero-order or jump model; U is along the geostrophic wind. (From LeMone et al. 2019) **35**

Figure 2.4: A greatly simplified division of boundary layers into (a) the weakly stable regime and (b) the strongly stable regime. (a) Plausible vertical structure corresponding to the relatively well-defined weakly stable regime. The grey zones delineate idealised horizontal layers. The entrainment zone is definable only for the weakest stability. The dashed blue curve depicts the typical height dependence of the TKE. The solid red line represents the general structure of both the potential temperature, θ, and the wind speed, V. The gradient arrow indicates the usual direction of the vertical transport of turbulence energy. (b) One of numerous different vertical structures for the very stable boundary layer. The red solid curve represents the potential temperature, and the orange solid curve represents the wind speed for the case of a near-surface wind maximum. For very stable conditions, various vertical structures are possible, and the vertical structure is generally nonstationary. In reality, the very stable boundary layer is typically an order of magnitude thinner than the weakly stable boundary layer. (From Mahrt 2014) **36**

Figure 2.5: (a) Average values (over all stations) of yearly median planetary boundary layer heights estimated using seven different methods. (top to bottom) Results for morning, midday, afternoon, and night-time. The number of stations used to compute each average (n_{stn}) is shown; the first value applies to six methods and the second applies to surface-based inversions. (b) Effect of sounding vertical resolution on estimated ABL heights (m) at Koror Island, Republic of Palau (7°N, 134°E), for the 1200 UTC sounding of 21 February 2007. Standard-resolution and high-resolution (black and red curves, respectively) (left) temperature (K) and (right) relative humidity (%) soundings are shown, along with the ABL heights identified by six methods. For the parcel, elevated inversion, and RH gradient methods, estimated heights differ for the high-resolution and standard resolution cases. For the q, N, and θ gradient methods, estimated ABL heights are the same. (from Seidel et al. 2010) **38**

Figure 3.1: Spatial map showing stations where radiosonde data is obtained for our study… **46**

Figure 3.2: Flowchart summarising our ABLH computation algorithm, including QC checks done..... **48**

Figure 3.3: Radiosonde data which was flagged by QC check used to determine if the sonde's upper air data points below 500 hPa are less than 10. This is an example of a sonde which was flagged as bad and therefore excluded in our interpolation and ABLH calculations. This sonde is from Irene station and dated 00h00 UTC 3 January 1979 ..... **49**

Figure 3.4: This is an example of radiosonde data which was flagged as bad by our QC check algorithm and therefore excluded in our interpolation and ABLH calculations. This illustrates that analysing data below 500 hPa and ABL will be difficult as there are only 2 data points below this level. This sonde is from Irene station and dated 00h00 UTC 3 January 1979…… **50**

Figure 3.5: Radiosonde data from Marion Island dated 14 January 1979 at 12h00 UTC. This is one of the radiosondes data which passed our QC checks and therefore used in our study. **52**

Figure 3.6: The Figure shows plots of data before being interpolated (as in Figure 3.5), and the data after being interpolated using the linear interpolation method as represented by Equation 3.5 and the three other popular interpolation techniques commonly used to interpolate 1-Dimensional functions – quadratic, cubic and nearest-neighbour interpolation schemes…..... **53**

Figure 3.7: Irene radiosonde observation climatologies for the months of September, October and November (austral spring) at 00h00 UTC. The seasonal mean is also included for each parameter..... **56**

Figure 3.8: Irene radiosonde observation climatologies for the months of September, October and November (austral spring) at 12h00 UTC. The seasonal mean is also included for each parameter.....**58**

Figure 3.9: Irene radiosonde observation climatologies for the months of December, January and February (austral summer) at 00h00 UTC. The seasonal mean is also included for each parameter.....**60**

Figure 3.10: Irene radiosonde observation climatologies for the months of December, January and February (austral summer) at 12h00 UTC. The seasonal mean is also included for each parameter.....**62**

Figure 3.11: Irene radiosonde observation climatologies for the months of March, April, and May (austral autumn) at 00h00 UTC. The seasonal mean is also included for each parameter..... **64**

Figure 3.12: Irene radiosonde observation climatologies for the months of March, April, and May (austral autumn) at 12h00 UTC. The seasonal mean is also included for each parameter..... **65**

Figure 3.13: Irene radiosonde observation climatologies for the months of June, July, and August (austral winter) at 00h00 UTC. The seasonal mean is also included for each parameter..... **67**

Figure 3.14: Irene radiosonde observation climatologies for the months of June, July, and August (austral winter) at 12h00 UTC. The seasonal mean is also included for each parameter..... **69**

Figure 3.15: Monthly climatologies of the ABLH for 00h00 UTC (blue) and 12h00 UTC (orange) over Irene..... **70**

Figure 3.16: Seasonal climatologies of the ABLH for 00h00 UTC (blue) and 12h00 UTC (orange) over Irene..... **71**

Figure 3.17: Marion Island radiosonde observation climatologies for the months of September, October, and November (austral spring) at 00h00 UTC. The seasonal mean is also included for each parameter **73**

Figure 3.18: Marion Island radiosonde observation climatologies for the months of September, October, and November (austral spring) at 12h00 UTC. The seasonal mean is also included for each parameter **75**

Figure 3.19: Marion Island radiosonde observation climatologies for the months of December, January, and February (austral summer) at 00h00 UTC. The seasonal mean is also included for each parameter **77**

Figure 3.20: Marion Island radiosonde observation climatologies for the months of December, January, and February (austral summer) at 12h00 UTC. The seasonal mean is also included for each parameter **79**

Figure 3.21: Marion Island radiosonde observation climatologies for the months of March, April, and May (austral autumn) at 00h00 UTC. The seasonal mean is also included for each parameter..... **81**

Figure 3.22: Marion Island radiosonde observation climatologies for the months of March, April, and May (austral autumn) at 12h00 UTC. The seasonal mean is also included for each parameter..... **83**

Figure 3.23: Marion Island radiosonde observation climatologies for the months of June, July, and August (austral winter) at 00h00 UTC. The seasonal mean is also included for each parameter..... **85**

Figure 3.24: Marion Island radiosonde observation climatologies for the months of June, July, and August (austral winter) at 12h00 UTC. The seasonal mean is also included for each parameter..... **87**

Figure 3.25: Monthly climatologies of the ABLH for 00h00 UTC (blue) and 12h00 UTC (orange) over Marion Island **88**

Figure 3.26: Seasonal climatologies of the ABLH for 00h00 UTC (blue) and 12h00 UTC (orange) over Marion Island **89**

Figure 3.27: Syowa radiosonde observation climatologies for the months of September, October, and November (austral spring) at 00h00 UTC. The seasonal mean is also included for each parameter **90**

Figure 3.28: Syowa radiosonde observation climatologies for the months of September, October, and November (austral spring) at 12h00 UTC. The seasonal mean is also included for each parameter **91**

Figure 3.29: Syowa radiosonde observation climatologies for the months of December, January, and February (austral summer) at 12h00 UTC. The seasonal mean is also included for each parameter **93**

Figure 3.30: Syowa radiosonde observation climatologies for the months of March, April, and May (austral autumn) at 00h00 UTC. The seasonal mean is also included for each parameter..... **95**

Figure 3.31: Syowa radiosonde observation climatologies for the months of March, April, and May (austral autumn) at 12h00 UTC. The seasonal mean is also included for each parameter..... **96**

Figure 3.32: Syowa radiosonde observation climatologies for the months of June, July, and August (austral winter) at 00h00 UTC. The seasonal mean is also included for each parameter..... **97**

Figure 3.33: Syowa radiosonde observation climatologies for the months of June, July, and August (austral winter) at 12h00 UTC. The seasonal mean is also included for each parameter..... **98**

Figure 3.34: Monthly climatologies of the ABLH for 00h00 UTC (blue) and 12h00 UTC (orange) over Syowa **99**

Figure 3.35: Seasonal climatologies of the ABLH for 00h00 UTC (blue) and 12h00 UTC (orange) over Syowa **100**

Figure 4.1: Irene 00h00 UTC austral spring seasonal mean CCAM and radiosonde vertical profiles, including the CCAM bias, of temperature, dewpoint temperature, potential temperature, lapse-rate, pressure, zonal wind, meridional wind, and relative humidity……**105**

Figure 4.2: Irene 12h00 UTC austral spring seasonal mean CCAM and radiosonde vertical profiles, including the CCAM bias, of temperature, dewpoint temperature, potential temperature, lapse-rate, pressure, zonal wind, meridional wind, and relative humidity……..**106**

Figure 4.3: Irene 00h00 UTC austral summer seasonal mean CCAM and radiosonde vertical profiles, including the CCAM bias, of temperature, dewpoint temperature, potential temperature, lapse-rate, pressure, zonal wind, meridional wind, and relative humidity……**107**

Figure 4.4: Irene 12h00 UTC austral summer seasonal mean CCAM and radiosonde vertical profiles, including the CCAM bias, of temperature, dewpoint temperature, potential temperature, lapse-rate, pressure, zonal wind, meridional wind, and relative humidity……..**108**

Figure 4.5: Irene 00h00 UTC austral autumn seasonal mean CCAM and radiosonde vertical profiles, including the CCAM bias, of temperature, dewpoint temperature, potential temperature, lapse-rate, pressure, zonal wind, meridional wind, and relative humidity……..**109**

Figure 4.6: Irene 12h00 UTC austral autumn seasonal mean CCAM and radiosonde vertical profiles, including the CCAM bias, of temperature, dewpoint temperature, potential temperature, lapse-rate, pressure, zonal wind, meridional wind, and relative humidity……..**110**

Figure 4.7: Irene 00h00 UTC austral winter seasonal mean CCAM and radiosonde vertical profiles, including the CCAM bias, of temperature, dewpoint temperature, potential temperature, lapse-rate, pressure, zonal wind, meridional wind, and relative humidity……..**111**

Figure 4.8: Irene 12h00 UTC austral winter seasonal mean CCAM and radiosonde vertical profiles, including the CCAM bias, of temperature, dewpoint temperature, potential temperature, lapse-rate, pressure, zonal wind, meridional wind, and relative humidity……..**112**

Figure 4.9: CCAM seasonal climatologies of the ABLH for 00h00 UTC (blue) and 12h00 UTC (orange) over Irene **113**

Figure 4.10: CCAM seasonal bias of the ABLH for 00h00 UTC (blue) and 12h00 UTC (orange) over Irene..... **113**

Figure 4.11: Marion Island 00h00 UTC austral spring seasonal mean CCAM and radiosonde vertical profiles, including the CCAM bias, of temperature, dewpoint temperature, potential temperature, lapse-rate, pressure, zonal wind, meridional wind, and relative humidity……..**114**

Figure 4.12: Marion Island 12h00 UTC austral spring seasonal mean CCAM and radiosonde vertical profiles, including the CCAM bias, of temperature, dewpoint temperature, potential temperature, lapse-rate, pressure, zonal wind, meridional wind, and relative humidity……..**115**

Figure 4.13: Marion Island 00h00 UTC austral summer seasonal mean CCAM and radiosonde vertical profiles, including the CCAM bias, of temperature, dewpoint temperature,

potential temperature, lapse-rate, pressure, zonal wind, meridional wind, and relative humidity..... **116**

Figure 4.14: Marion Island 12h00 UTC austral summer seasonal mean CCAM and radiosonde vertical profiles, including the CCAM bias, of temperature, dewpoint temperature, potential temperature, lapse-rate, pressure, zonal wind, meridional wind, and relative humidity..... **117**

Figure 4.15: Marion Island 00h00 UTC austral autumn seasonal mean CCAM and radiosonde vertical profiles, including the CCAM bias, of temperature, dewpoint temperature, potential temperature, lapse-rate, pressure, zonal wind, meridional wind, and relative humidity……..**118**

Figure 4.16: Marion Island 12h00 UTC austral autumn seasonal mean CCAM and radiosonde vertical profiles, including the CCAM bias, of temperature, dewpoint temperature, potential temperature, lapse-rate, pressure, zonal wind, meridional wind, and relative humidity……..**118**

Figure 4.17: Marion Island 00h00 UTC austral winter seasonal mean CCAM and radiosonde vertical profiles, including the CCAM bias, of temperature, dewpoint temperature, potential temperature, lapse-rate, pressure, zonal wind, meridional wind, and relative humidity……..**119**

Figure 4.18: Marion Island 12h00 UTC austral winter seasonal mean CCAM and radiosonde vertical profiles, including the CCAM bias, of temperature, dewpoint temperature, potential temperature, lapse-rate, pressure, zonal wind, meridional wind, and relative humidity……..**120**

Figure 4.19: CCAM seasonal climatologies of the ABLH for 00h00 UTC (blue) and 12h00 UTC (orange) over Marion Island **121**

Figure 4.20: CCAM seasonal bias of the ABLH for 00h00 UTC (blue) and 12h00 UTC (orange) over Marion Island..... **121**

Figure 4.21: Syowa 00h00 UTC austral spring seasonal mean CCAM and radiosonde vertical profiles, including the CCAM bias, of temperature, dewpoint temperature, potential temperature, lapse-rate, pressure, zonal wind, meridional wind, and relative humidity……..**122**

Figure 4.22: Syowa 12h00 UTC austral spring seasonal mean CCAM and radiosonde vertical profiles, including the CCAM bias, of temperature, dewpoint temperature, potential temperature, lapse-rate, pressure, zonal wind, meridional wind, and relative humidity……..**123**

Figure 4.23: Syowa 00h00 UTC austral summer seasonal mean CCAM and radiosonde vertical profiles, including the CCAM bias, of temperature, dewpoint temperature, potential temperature, lapse-rate, pressure, zonal wind, meridional wind, and relative humidity……..**124**

Figure 4.24: Syowa 12h00 UTC austral summer seasonal mean CCAM and radiosonde vertical profiles, including the CCAM bias, of temperature, dewpoint temperature, potential temperature, lapse-rate, pressure, zonal wind, meridional wind, and relative humidity……..**124**

Figure 4.25: Syowa 00h00 UTC austral autumn seasonal mean CCAM and radiosonde vertical profiles, including the CCAM bias, of temperature, dewpoint temperature, potential temperature, lapse-rate, pressure, zonal wind, meridional wind, and relative humidity……..**125**

Figure 4.26: Syowa 12h00 UTC austral autumn seasonal mean CCAM and radiosonde vertical profiles, including the CCAM bias, of temperature, dewpoint temperature, potential temperature, lapse-rate, pressure, zonal wind, meridional wind, and relative humidity……..**126**

Figure 4.27: Syowa 00h00 UTC austral winter seasonal mean CCAM and radiosonde vertical profiles, including the CCAM bias, of temperature, dewpoint temperature, potential temperature, lapse-rate, pressure, zonal wind, meridional wind, and relative humidity……..**127**

Figure 4.28: Syowa 12h00 UTC austral winter seasonal mean CCAM and radiosonde vertical profiles, including the CCAM bias, of temperature, dewpoint temperature, potential temperature, lapse-rate, pressure, zonal wind, meridional wind, and relative humidity……..**127**

Figure 4.29: CCAM seasonal climatologies of the ABLH for 00h00 UTC (blue) and 12h00 UTC (orange) over Syowa.....**128**

Figure 4.30: CCAM seasonal bias of the ABLH for 00h00 UTC (blue) and 12h00 UTC (orange) over Syowa..... **129**

LIST OF TABLES

Table 1.1: A summary of different closure techniques as used by atmospheric numerical models used for weather forecasting and climate projections ...…….....… **28**

Table 3.1: Plausibility limits used in basic validity checks (from Durre (2016)) ...…… **48**

Table 3.2: Data points showing x and y variables. x is the independent variable, and y is the dependent variable ...…… **54**

LIST OF ABBREVIATIONS

ABL: Atmospheric Boundary Layer

ABLH: Atmospheric Boundary Layer Height

ACCESS-C: Australian Community Climate and Earth System Simulator

AMTEX: Air Mass Transformation Experiment

ARW-WRF: Advanced Research Weather Research and Forecasting

BL: Boundary Layer

BLH: Boundary Layer Height

CARDS: Comprehensive Aerological Reference Data Set

CBL: Convective Boundary Layer

CCAM: Conformal-Cubic Atmospheric Model

CMIP: Coupled Model Intercomparison Project

COAMPS: Coupled Ocean-Atmosphere Mesoscale Prediction System

CSIRO: Commonwealth Scientific and Industrial Research Organisation

ECMWF: European Centre for Medium-range Weather Forecasts

ENSO: El Niño Southern Oscillation

ESM: Earth System Model

FA: Free Atmosphere

FIFE: First ISLSCP Field Experiment

GARP: Global Atmospheric Research Programme

GATE: GARP Atlantic Tropical Experiment

GBM: Grenier–Bretherton–McCaa

GCM: Global Circulation Model

GTS: Global Telecommunications System

HAPEX: Hydrologic Atmosphere Pilot Experiment

IGRA 2: Integrated Global Radiosonde Archive Version 2

IGRA: Integrated Global Radiosonde Archive

IGRA: Integrated Global Radiosonde Archive

IPCC: Intergovernmental Panel on Climate Change

ISLSCP: International Satellite Land Surface Climatology Project

ITCZ: Intertropical Convergence Zone

JASIN: Joint Air Sea Interaction

LES: Large Eddy Simulation

LLJ: Low-Level Jet

MYJ: Mellor-Yamada-Janjic

NBL: Nocturnal Boundary Layer

NCDC: National Climatic Data Centre

NCEI: National Centres for Environmental Information

NH: Northern Hemisphere

NOAA: National Oceanic and Atmospheric Administration

NWP: Numerical Weather Prediction

PBL: Planetary Boundary Layer

PDO: Pacific Decadal Oscillation

QC: Quality Control

RCM: Regional Climate Model

SAWS: South African Weather Service

SBI: Surface-Based Inversion

SBL: Stable Boundary Layer

SH: Southern Hemisphere

SO: Southern Ocean

SST: Sea surface temperature

TAPM: The Air Pollution Model

TEMF: Total Energy-Mass Flux

TKE: Turbulence Kinetic Energy

U.S.: United States

UM: Unified Model

UN: United Nations

WCRP: World Climate Research Programme

WMO: World Meteorological Organisation

WRF: Weather Research and Forecasting

CHAPTER 1: INTRODUCTION

1.1. BACKGROUND

The Earth's atmosphere is one of the most basic aspects of our daily lives. It is inconceivable to think of life on Earth as we know it without its presence. Every planet in the solar system has an atmosphere, however, Earth is the only known planet with an atmosphere optimal for human life (Andrews 2010). The Earth's atmosphere can be divided into five major layers. From the lowest to the highest atmosphere, these are named: troposphere, stratosphere, mesosphere, thermosphere, and exosphere. It is within the troposphere that most of human life and activities take place, and where nearly all-weather phenomena occur. The troposphere is on average 10 km thick and can also be subdivided into the atmospheric boundary layer (ABL) making up more or less the lowest 1 km above the Earth's surface, and the free atmosphere (FA) representing the remaining 9 km (Stull 1988). Although on a global scale the ABL is on average close to 1 km, it is variable in time and space and can range from a few metres to several kilometres above the surface under various conditions (Seidel et al. 2012).

The ABL plays an important role in the climate system as it helps to regulate the energy exchange between the various Earth surfaces and the atmosphere (Baede et al. 2001). As a result, it is imperative that weather and climate models include ABL processes. However, due to the turbulent nature of the ABL, often represented by small and large eddies, models struggle to fully represent its properties. The turbulent eddies play a key role in the vertical transport of momentum, heat, and moisture, and are therefore important in the evolution and flow of the atmosphere at all timescales (Sun et al. 2017). Since weather and climate models struggle to explicitly resolve turbulence, the concept of parameterisation is applied to represent ABL processes.

1.2. CLIMATE MODELLING AND CLIMATE MODEL DEVELOPMENT

Atmospheric modelling has become popular in the 21st century. This is especially true in the fields of weather and climate prediction, where numerical methods are typically used to discretise complex mathematical equations representing the evolution and flow of the atmosphere at different timescales (Kalnay 2003). To differentiate between weather and climate timescales, Gettelman and Rood (2016) define climate as a distribution of probable weather, and weather as a given state in that distribution. Predicting how the state of the atmosphere will evolve at these two timescales requires different methods which are also associated with different types of uncertainty.

Numerical weather prediction (NWP) is a mathematical approach to modelling the initial value

problem and is a method applicable to operational weather forecasting. An initial value problem implies that correctly depicting the state of the atmosphere at a given moment in time is of vital importance in accurately predicting its evolution in time. Climate projection is a boundary value problem solved through the use of global climate models (GCMs), which have similar dynamics and physical parameterisations as NWP models. Future climate change depends on external forcing, and particularly on solar radiative forcing and greenhouse gas forcing (termed boundary forcing) (Weller et al. 2010). Initial conditions are of lesser importance in climate projections, although the inertia of long-term cyclic processes such as the Pacific Decadal Oscillation (PDO) can influence predictions for the next decades, and phenomena such as the El Niño Southern Oscillation (ENSO) provide skill to seasonal forecasts.

One essential part of improving models used for weather and climate prediction is their evaluation. In operational weather forecasting, NWP models are regularly evaluated with ease, given that their timescale is within the range of day-to-day observations. Climate models are evaluated by verifying their ability to simulate the climate of the last several decades (referred to as present-day climate) against available observations (Gettelman and Rood 2016), testing their accuracy in representing the trends that can be detected in climate over the last several decades (Engelbrecht et al. 2015) and finally, verifying the realism of their simulations of paleoclimates through the use of proxy observations of the distant past (Engelbrecht et al. 2019). An understanding of the uncertainties associated with climate model simulations is important when considering their projections of future climate change. Rigorous model evaluation is important to describe the uncertainties that stem from model inaccuracies and errors. There are several other uncertainties associated with projections of future climate change, including future climate change mitigation pathways and the resulting emission scenarios (O'Neil et al. 2020).

1.2.1. Climate and Earth System Modelling

While climate is defined as the long-term mean state of the atmosphere, climate variability refers to the variations in that mean state, and climate change refers to the persistent shift and change in that mean state (Folland et al. 2001). The behaviour of the atmosphere is dynamic and nonlinear in nature (Holton and Hakim 2013). However, the behaviour of the climate system does not only depend on atmospheric processes, but also physical, chemical, and biological processes of the Earth system (Wallace and Hobbs 2006). This implies that realistically modelling the climate involves the coupling of different components of the Earth system, namely: atmosphere, hydrosphere, cryosphere, land surface and biosphere (Baede et al. 2001). All the components of the Earth system play a role in directly and indirectly determining the evolution of the climate system, whether its variability or change, and hence

these components all need to be represented in climate and earth system models. Historically, GCMs and downscaled regional climate models (RCMs) couple the atmosphere, ocean, sea ice and land surface (e.g. Delworth et al. 2006). Earth System Models (ESMs) build on top of the model components found in a GCM, the carbon cycle, vegetation, atmospheric chemistry, ocean biogeochemistry, and continental ice sheets, including the feedbacks between all these processes (Döscher et al. 2017).

1.2.2. Model Evaluation and the Development of Climate Models in South Africa

Since its formation by the United Nations (UN) in 1988, the Intergovernmental Panel on Climate Change (IPCC) is seen as being at the forefront of assessments of climate change projections produced by world-leading climate modellers and scientists (Hulme and Mahony 2010). The IPCC Assessment Reports rely largely on the model projections generated through the Coupled Model Intercomparison Project (CMIP) (Eyring et al. 2016), which is administered by the World Climate Research Programme (WCRP). An evaluation of the models used is vital to understanding the feedbacks within the Earth system, biases, and uncertainties of climate change projections.

An evaluation of the CMIP models, and other models used for climate change projections, has shown that most of them have relatively higher uncertainties in simulations of the Southern Hemisphere (SH) in comparison with the Northern Hemisphere (NH), and especially in continental Antarctica and the SO (e.g. Wang et al. 2014; Randall et al. 2007). These high uncertainties present a problem because the SO is known to play a significant role in influencing the climate system, as it accounts for 75% ± 22% ($23 \pm 9 \times 10^{22}$ J) of heat uptake and 43% ± 3% (42 ± 5 Pg C) of anthropogenic CO_2 uptake by the global oceans (Frölicher et al. 2015). One implication of this is that to improve climate change projections in terms of their reliability, there needs to be an improved representation of SH processes, and especially those of the Southern Ocean (SO), which have also been found to influence South African weather patterns (e.g. Blamey and Reason 2007). In previous CMIP simulations, only one ESM developed in the SH was utilised. The latest phase of the intercomparison (i.e. CMIP6) has seen the inclusion of two more ESMs developed in the SH, which improves the simulation of represented southern hemispheric processes as prioritised by local scientists.

To help improve our understanding of processes impacting the SH (including Antarctica and SO), southern Africa, and Africa in general, South African modellers and scientists (in collaboration with their Australian counterparts) are continually developing the first African - based ESM and have also outlined a plan to further develop numerical models for the region (Bopape et al. 2019). Evaluating this model in simulating present-day processes of the SH is

therefore, needed to detect any biases, which may further improve our understanding of uncertainties presented in climate change projections.

Some of the most important processes represented in all atmospheric models (and at all timescales) are those happening in the ABL. An ABL parameterisation is used in the conformal cubic atmospheric model (CCAM), the atmospheric component of the ESM and NWP models under development at the Global Change Institute (GC) of the University of the Witwatersrand and South African Weather Service (SAWS). The evaluation of CCAM in simulating the ABL in the SH is important and will aid understanding of the Earth System's influence on this layer and vice versa. The evaluation of CCAM ABL parameterisations over southern Africa, the SO to the south of South Africa, and Antarctica has never been undertaken before – and there is a general lack of GCMs evaluation in terms of their representations of present-day attributes of the ABL in continental Antarctica, SO, and continental southern Africa. This research project will aim to perform the first verification of the CCAM ABL simulations over the mentioned regions in the SH.

1.3. INTRODUCTION TO THE BOUNDARY LAYER AND ITS PARAMETERISATION

The ABL, PBL, or BL as defined in atmospheric sciences, is that part of the troposphere directly above the Earth's surface where there is a constant turbulent exchange of surface forcings (Beljaars 1994). The presence of the Earth’s surface in this layer directly influences its evolution and modifies it, making it variable in space and time. The turbulent exchange gives it a unique set of characteristics different from the FA. The FA is the layer making up the remainder of the troposphere just above the ABL.

Atmospheric models are computer programs built on mathematical equations representing the evolution of the atmosphere over time. This evolution is represented by the dynamics and physical processes which occur in the atmosphere. The dynamics are modelled using the primitive equations which are a set of nonlinear differential equations (Holton and Hakim 2013) describing the conservation of momentum (Navier-Stokes equations), conservation of mass (the continuity equation) and conservation of energy (thermodynamic equation). Other equations generally included are those describing the conservation of water vapour mixing ratio and the atmosphere as an ideal gas (equation of state).

The dynamical core of the model is traditionally discretised using numerical processes on grid-cells spatial resolutions that are constrained by the computational expense in solving the equations (Kalnay 2003). However, sub-grid processes are left unresolved by the discretised model dynamics and are, therefore, together with other sub-grid features, represented using physical parameterisation schemes.

Different models prioritise parameterising different processes, in different ways, depending on their use. Some of the important processes parameterised include radiation, convection, precipitation, cloud microphysics, aerosols, ABL processes and various surface features. These two fundamental constituents of a typical atmospheric model (dynamical core and physics core) are simulated on high-performance computers to produce numerical weather predictions and future climate projections.

1.3.1. Boundary Layer Processes

The most basic aspect of the ABL is its interaction with the processes occurring on or near the surface. Some of the important parameters, such as daily 2-metre temperature forecasts, are derived from the representations of these interactions in models (Hu et al. 2010). Some weather events, such as convective storm initiation and maintenance, are also directly and indirectly instigated in the ABL (Bèlair et al. 1999); while the FA is also influenced by the Earth's surface through the ABL (Smith 1993). For these reasons, it is of importance to properly represent ABL processes in models for them to accurately predict the evolution of the atmosphere at all timescales.

It is important to note that different types ABLs occur in different climatic regimes across the planet, and that these all exhibit different properties at different spatio-temporal scales, and these are important to consider during parameterisation (see Figure 1.1). The Global Energy and Water Cycle Experiment's study on the ABL identified some of the processes parameterised in models as turbulence, clear air radiation, drainage flow, gravity waves and shear instabilities, fog and dew formation, and the occurrence of low-level jets (Holtslag et al. 2011). All of these are relatively small-scale processes, but they play an important role in the momentum, heat and moisture fluxes below and above the ABL height. The effects of turbulent exchange and transport on the atmospheric flow are parameterised.

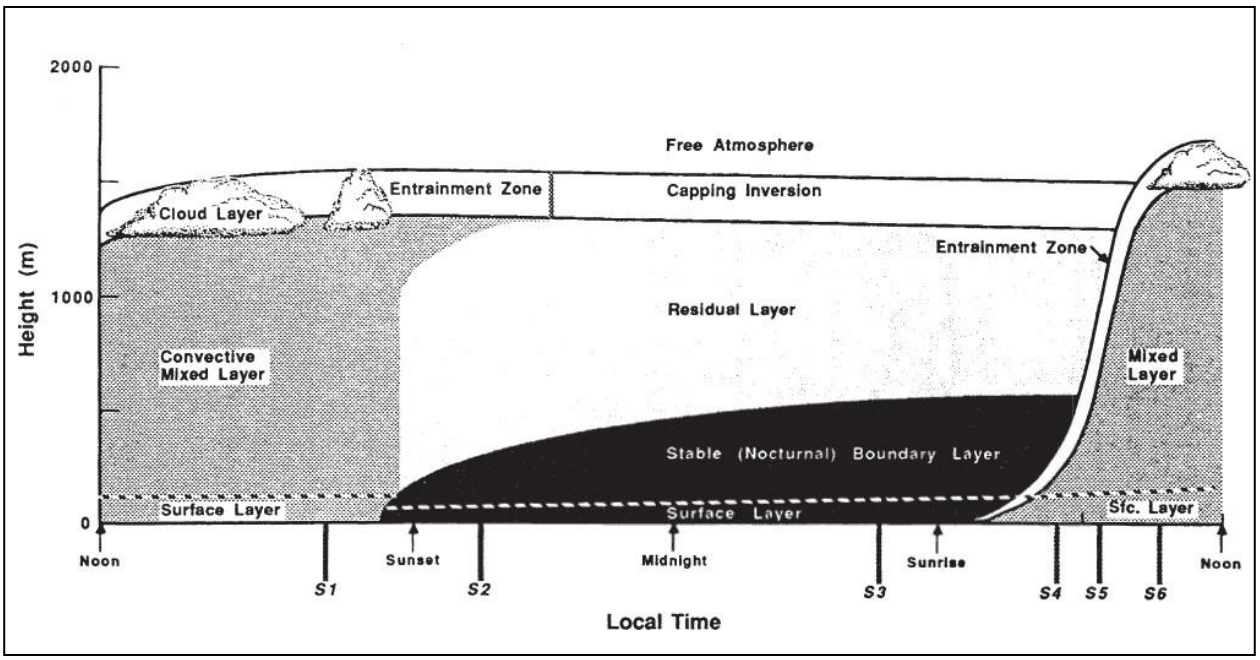

Figure 1.1: The structure of the boundary layer during a typical diurnal cycle, showing different layers present according to atmospheric stability and time of day (Stull 1988, page 11).

1.3.2. The Boundary Layer Parameterisation in Atmospheric Models

Many different ABL parameterisation schemes are used by atmospheric models, from simple NWP models to much more complex ESMs. To use correct parameterisation schemes, there first need to be a recognition of the closure problem resulting from the turbulent nature of the mixing within the ABL (Holt and Raman 1988). This is known as the turbulence closure problem, were deriving a set of closed equations is not possible due to the number of unknowns being larger than the number of equations.

There are two main approaches when it comes to addressing the closure problem. The first approach is that unknown quantities at any point can be parameterised by mean atmospheric values or gradients of known quantities at the same point (Lock et al. 2000). This is known as local closure and is equivalent to molecular diffusion. The second approach, also described by Lock et al. (2000), known as the non-local closure, says that unknown quantities at one point can be parameterised by atmospheric values or gradients of known quantities at the many points in space.

One disadvantage of local closure is the inability to represent the effects of larger eddies. These include a limitation to simulating turbulent mixing within adjacent layers symmetrically (Xie et al. 2012). The non-local approach accounts for these effects of larger eddies and

therefore better represents the evolution of convective well-mixed ABLs (Bèlair et al. 1999). Schemes of a non-local nature are computationally expensive. To counter the expense, some studies have shown that including non-local effects in turbulence schemes based on eddy diffusivity coefficients, help better represent the convective ABLs (e.g. Mailhot and Benoit 1982; Troen and Mahrt 1986). The following are major general ABL schemes originating from the two main philosophies addressing the closure problem already identified.

1.3.2.1. Zero and half-order schemes

Zero-order closure directly parameterises all quantities as a function of space and time, and there is no prognostic equation that is retained including for mean quantities (Stull 1988). Hence, this order is neither local nor non-local since it completely avoids parameterising turbulence. On the other hand, a subset of the first moment equations is used in the half-order closure.

1.3.2.2. First-order schemes (K-theory schemes)

Parameterisation schemes of the first-order could be local or non-local. In the local scheme, eddy diffusivity is often used to relate turbulent fluxes to local mean gradients which is related to local stability (Lock et al. 2000).

1.3.2.3. 1.5-order schemes (TKE schemes)

This closure retains both the prognostic equations for the zero-order statistics and equations for the variances of those variables (Stull 1988). TKE is predicted using the prognostic energy equation.

One of the most widely used 1.5-order schemes is the MYJ scheme (Banks et al. 2016). MYJ is a local closure TKE scheme that considers local vertical mixing (Janjić 2001). Another example of this scheme is the TEMF scheme. TEMF scheme is non-local and uses the concepts of eddy diffusivity and mass flux to estimate vertical mixing, in addition to having the sub-grid scale total energy prognostic and mass-flux-type shallow convection (Banks et al. 2016).

1.3.2.4. Second and third-order schemes

Second-order schemes retain the first two equations and approximate third moments. Similarly, a third-order scheme will retain the first three equations and approximates fourth moments including the pressure correlations and viscous dissipation (Stull 1988). The development and use of higher-order schemes are strongly dependent on computing power,

and the measurements of moments of this order are also difficult in the real atmosphere (Stull 1988).

The table below summarises different closure techniques normally used by NWP models, GCMs and ESMs to parameterise ABL processes (according to Stull 1988, and the latest literature).

Table 1.1: A summary of different closure techniques as used by atmospheric numerical models used for weather forecasting and climate projections.

Order	*Local*	*Non-local*	*Other* *(bulk or similarity methods)*
Zero			X
Half	X	X	X
First	X	X	
One-and-a-half	X	X (*e.g.* Banks et al. 2016)	
Second	X		
Third	X		

1.3.3. The Boundary Layer Height

As a result of different ABL schemes used in different GCMs and ESMs (which use different techniques to parameterise ABL processes), ABL heights from different model simulations may be different. Being able to simulate ABL height is important as it determines the entire ABL mixing volume and aerosol concentration – it can be calculated from different observations, but the method utilising radiosondes observations is popular and well established (Seibert et al. 2000) and can be used for climatological studies (Seidel et al. 2012).

1.3.4. Overview of Studies on Boundary Layer Simulations in South Africa

Studies focusing on the simulations of the ABL over South Africa are limited. Previous research conducted on atmospheric parameterisation is mostly limited to convection (e.g. Crétat et al. 2012; Pohl et al. 2014; Ratna et al. 2014). However, in 2010, Korhonen et al. (2014) conducted the first long-term study of ABL top heights and ABL growth rates in South

Africa. In their study, they compared various observational data collected over 1 year with three atmospheric models, namely: the ECMWF model, the UM from SAWS, and TAPM. They found that the ECMWF model performed best in simulating the ABL height, followed by the UM and TAPM, possibly due to their underestimation of vertical wind speeds. Various parameterisation schemes were also tested when producing the Wind Atlas of South Africa (Hahmann et al, 2015), and de Lange et al. (2021) evaluated the performance of four ABL schemes from simulations by the ARW-WRF model during the winter and spring seasons of 2016. They concluded that the MYJ scheme performs better in simulating meteorological variables during spring and that the local closure scheme is preferred during winter.

ABL simulation studies in the SO are generally limited by a lack of observational data for verification. Perlin et al. (2014) investigated the wind speed response to mesoscale SST variability over the Agulhas Return Current region of the SO using the WRF model and the U.S. Navy COAMPS atmospheric model. They found that the GBM scheme performed better on WRF and Mellor–Yamada parameterisation performed better on COAMPS. Huang et al. (2015) evaluated how the limited-area version of the ACCESS-C performs in simulating the ABL clouds over Tasmania and the adjacent SO. It was found that although the model demonstrates skill in simulating the macrophysical properties of the ABL clouds over the SO, it struggles when it comes to predicting the area cloud fraction of the marine ABL clouds and that the capping inversion over the marine ABL is generally too high.

1.4. AIMS AND OBJECTIVES

Literature indicates that the ABL is understudied in the Southern Hemisphere compared to the Northern Hemisphere, and that most climate models struggle to represent this essential part of the troposphere (Wang et al. 2014). This in turn contributes to uncertainties of future climate change projections (Randall et al. 2007), making it difficult for policy makers to robustly plan for the future. It is for those reasons that the primary aim of this study is to evaluate the simulations of Southern Hemispheric boundary layer by global atmospheric model CCAM. This aim will be achieved through the following objectives:

a) Determine a climatology of present-day ABL attributes from atmospheric soundings across the Southern Hemisphere’s, including high-latitude, mid-latitude, and subtropical continental locations.
b) Evaluate how the atmospheric model CCAM simulates attributes of the ABL climatology over the Southern Hemisphere's high-latitude, mid-latitude, and subtropical continental locations.

1.5. STRUCTURE OF THE REPORT

This section summarises the outline of the report. Chapter 2 surveys the literature on the ABL, including findings from fundamental research, observation technologies and modelling activities. We also include literature on characteristics of the ABL over different latitudes, and on how weather and climate models, and specifically the CCAM, simulate these. In Chapter 3 s a first set of results based on observations (soundings) is presented. These include a description of observation data, and methods used to compute the ABL height climatology and seasonality. A second set of results and discussions based on the CCAM model data is in Chapter 4, which includes an evaluation of the model's ability to represent present-day ABL attributes. Chapter 5 is on conclusions and recommendations emanating from the study.

CHAPTER 2: LITERATURE REVIEW

2.1. INTRODUCTION

The ability to define the boundary layer height is not possible without a proper understanding of the concept of the boundary layer. Although boundary layer studies are not as widespread and extensive in South Africa, literature does show that they span over a century in some parts of the world. Figure 2.1 depicts a summarised timeline of developments in the boundary layer theory which are briefly discussed in this section.

It is interesting to note that the study of the atmosphere and its prediction can be traced as far back as the earliest human species, but the concept, general theory and quantitative understanding of the boundary layer was non-existent until Ludwig Prandtl proposed it in 1904. The beginning of this century was marked by the seminal paper Prandtl (1905) which theorised that the effect of friction due to the presence of the surface, or object, causes the fluids' flow near that surface to drag, and therefore have a near-zero velocity relative to the flow not in direct contact with the surface. The thin layer near the surface where this phenomenon occurs was named the boundary layer, which in essence acts as a boundary, and separates the surface and the free flow on the other end of the layer. Prandtl (1905) was only eight pages long and was published as a companion to a conference presentation made by Ludwig Prandtl a year before, in early August 1904, and Anderson (2005) describes it as one of the most important papers ever written in the field of fluid dynamics. The conceptualisation of the boundary layer theory by Prandtl (1905) is the birthplace of the modern field of Boundary-Layer Meteorology and has revolutionised the modelling and prediction of the entire atmospheric system, both at the weather and climate timescales.

It was not long after Ludwig Prandtl published his work, that Vagn Walfrid Ekman made public his hypothesis emerging from the intersection between the past understanding of the concept of friction, turbulence and the Earth’s rotation. The original paper (Ekman 1905) described this for the upper ocean but was soon modified for application in the atmosphere in a subsequent paper (Ekman 1906). What Vagn Walfrid Ekman's papers hypothesised was that there exists a layer just near the surface (originally upper ocean surface) where the frictional force is balanced by Coriolis force. This layer is commonly referred to as the Ekman Layer and helps in our understanding of

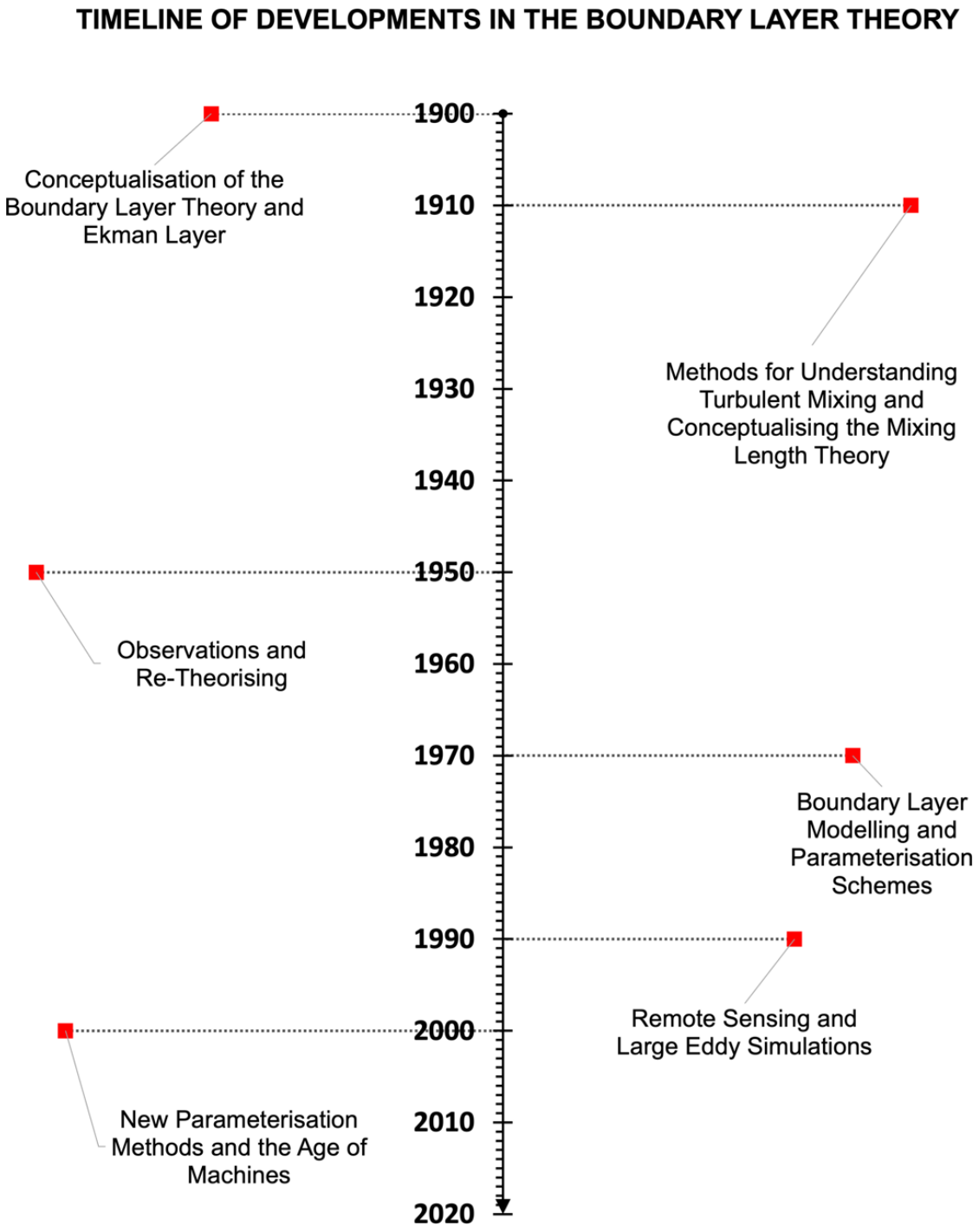

Figure 2.1: A summary of some major developments in boundary layer research based on literature. The expanded text on some of these is contained in Section 2.1.

the geophysical fluids' flow in the boundary layer; and in essence explains why near the surface there is ageostrophic flow associated with friction and small eddies. The presence of eddies effectively redistributes fluid parcels through turbulence diffusivity. To a large extent, the Ekman Layer accounts for why the fluids' flow is ageostrophic at the bottom of the boundary layer and geostrophic at the top.

A British mathematician and physicist named Geoffrey Taylor, published a paper in 1915 (Taylor 1915) where he advanced the idea of the turbulent exchange in the atmosphere being a "process like molecular conduction but much more vigorous" (Wyngaard 2010). He argued that through turbulence, there is a vertical movement and mixing of airmasses over a certain distance. This distance is commonly known as the mixing length. The idea of mixing length was later used to develop semiempirical turbulence theories from which von Kámán (1931) developed logarithmic profiles describing the flow of neutrally stratified air as a function of height. Richardson (1920) developed the so-called Richardson number, which is a criterion for turbulence breakdown in sheared and stratified fluid and is currently commonly used in atmospheric modelling. In 1922, Lewis Richardson also hypothesised that turbulent flows are composed of eddies of different sizes and that the kinetic energy of the flow cascades from large to small scale eddies (Lemone et al. 2019). It was, however, Kolmogorov (1941a,b) and Obukhov (1941) who mathematically described our modern understanding of energy transfer processes in a turbulent flow.

Much of our understanding of the boundary layer comes from observations made both in the field and in laboratory settings. Not only are observations important in our understanding of boundary layer processes, but they are also important in the development of parameterisation schemes and in validating models. Some of the most important observations which helped advance boundary layer meteorology include, the Scilly Isles field experiment of Sheppard et al. (1952) focusing on the ABL over the ocean and the U.S. Great Plains observations (Lettau and Davidson 1957) which focused on the land. Others include the Wangara and Koorin observations in Australia (Clarke et al. 1971, Clarke and Brook 1979) and the Minnesota experiment in the U.S. (Izumi and Caughey 1976). However, major breakthroughs and the re-theorising, or calibration, of some boundary layer concepts were made when international observation efforts were undertaken. These include the BOMEX in 1969 (Kuettner and Holland 1969), GATE in 1974 (Kuettner and Parker 1976), AMTEX in 1974 and 1975 (Lenschow and Agee 1976), JASIN in 1978 (Charnock and Pollard 1983), HAPEX in 1986 (Andre et al. 1986) and FIFE in 1987 (Sellers et al. 1988).

The development of computers in the middle of the 20th century allowed the introduction of NWP and GCM models, starting with dynamical cores and later introducing parameterisation

schemes (e.g. Charney et al. 1950, Hinkelmann 1951, Charney and Phillips 1953, Bolin 1955, Lorenz 1960, Charney 1962, Bushby and Timpson 1967, Shuman and Hovermale 1968). But, as already mentioned, the size of the eddies in the ABL differs from a few kilometres to a few millimetres, and there is a cascade of energy from large to small eddies. This means that these models were still not enough to resolve ABL turbulence, and even the most advanced computers today cannot fully resolve them. Hence, the design of an LES model from the late 1960s by James W. Deardorff and Douglas K. Lilly at NCAR has supplemented the use of observations in advancing model development (Kanak 2004). From the 1990s and 2000s, improved observation methods and resolution, have helped in the development of new parameterisation schemes. With the advent of quantum computers, the use of artificial intelligence (and machine learning in particular) is picking up momentum. Artificial intelligence seems to be important in the future of model development, albeit with much debate on whether it is scientific enough to replace traditional Earth System and Climate Models.

2.2. STUDIES OF THE BOUNDARY LAYER AND THE CLIMATOLOGY OF ITS HEIGHT

Historically, most boundary layer studies have been concentrated in the Northern Hemisphere – especially the Soviet Union (particularly Russia), the continental United States of America, Europe, and the Arctic (Lemone et al. 2019). The Northern Hemispheric concentration of boundary layer studies can be attributed to the advances in the atmospheric observing systems, and instrumentations developed both in the field and laboratory settings of the North American, European, and Soviet Union countries (Stith et al. 2019). Some of these studies were partly initiated due to some knowledge from other fields such as agriculture. For example, farmers knew that most crop-threatening frosts at night were most likely at low-lying elevations (McAdie 1915) and that there is a relationship between temperature and height at different times of the day (Dines 1882). Nonetheless, in recent decades, there has been an interest in understanding boundary layers in the Southern Hemisphere, especially as they do influence the control of the global climate system and its subsequent modelling.

As already stated in Chapter 1, the boundary layer essentially links the surface and the atmosphere. The depth of this layer is important in the vertical distribution of energy and the characteristics of the layer itself. Depending on the time of day, the structure of the boundary layer will vary mainly due to the solar energy from the sun, or lack thereof. This variation causes the depth of the boundary layer to also vary throughout the day and night. The parameter defining this depth is often referred to as the boundary layer height or mixing height. In this section, we look at literature concerning the boundary layer height climatology.

The surface underlying the boundary layer plays a crucial role in its depth. For example, over oceans, the diurnal variation of the boundary layer height is not as pronounced as over deserts. This is because surface temperature changes little over the ocean compared to land surfaces since water has a large heat capacity. Therefore, a slow-changing sea surface temperature means a slowly varying forcing into the bottom of the boundary layer; and a quickly changing land surface temperature (e.g., over deserts) means a quickly varying forcing into the bottom of the boundary layer (Stull 1988). As a result, unlike over lands where surface temperatures are important in determining the depth of the boundary layer, over oceans significant changes are mostly driven by synoptic and mesoscale processes such as fronts and convection. This does not imply that synoptic and mesoscale processes are not important over lands, rather they play a more crucial role in influencing the marine boundary layers. Stull (1988) also affirms that the boundary layer depth tends to be thinner over high-pressure surfaces, compared to low-pressure surfaces. This is because subsidence dominates high-pressure regions, while upward motion dominates low-pressure regions. Figure 2.2 demonstrates this general concept.

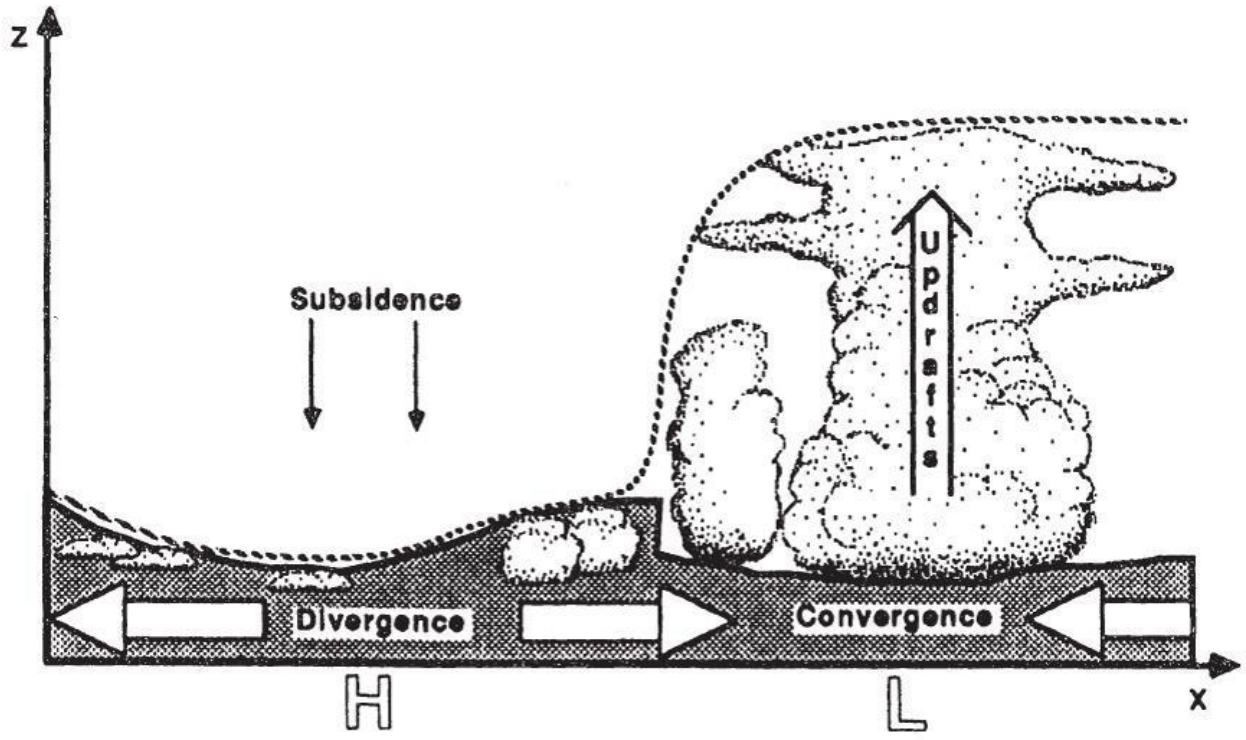

Figure 2.2: Schematic of synoptic-scale variation of boundary layer depth between centres of surface high (H) and low (L) pressure. The dotted line shows the maximum height reached by surface-modified air during one hour. The solid line encloses the shaded region, which is most studied by boundary layer meteorologists. (From Stull 1988, page 9)

Literature preferably categorises the determination and modelling of boundary layer heights into two main types based on the layer's stability. These are often referred to as convective boundary layer and stable boundary layer.

2.2.1. Convective boundary layers

From the beginning of the 20th century, until the 1970s, mean wind profiles were thought to be similar to the Leipzig wind profile as described by Lettau (1950). Although temperature profiles were constructed using observed dry-adiabatic lapse rates, wind profiles under convective conditions were thought to resemble the "Ekman spiral" (Ekman 1905). It was not until the late 1960s and 1970s that it was found that the stabilities of the Ekman spiral influenced the wind profiles (Faller 1963, Faller and Kaylor 1966, Lilly 1966, Brown 1970, Brown 1978). This was also characterised by LES implementations in the 1970s, and advanced atmospheric measurements, which made it possible to verify that under unstable conditions, thermodynamic variables play a fundamental role in determining the boundary layer height (Deardorff 1970a,b, 1974). The LES approach to studying the boundary layer was also used by Moeng and Sullivan (1994), whose analysis indicated that strongly convective flows within the boundary layer are primarily dominated by buoyancy-driven updrafts whose size is of the order of the boundary layer depth. In boundary layer studies, these are typically referred to as large eddies, which play an important role in the mixing of mean fields, and in weather and climate models are parameterised using non-local closure schemes. On the contrary, they also found that unlike with shear-driven boundary layers, which have an Ekman-like profile, CBL almost has no winds turning with height except near the surface and above the boundary layer height. This is illustrated by Figure 2.3 from LeMone et al. (2019), where Figure 2.3 (a) and (b) are adapted from Moeng and Sullivan (1994) and Figure 2.2 (c) from idealised studies by Conzemius and Fedorovich (2006).

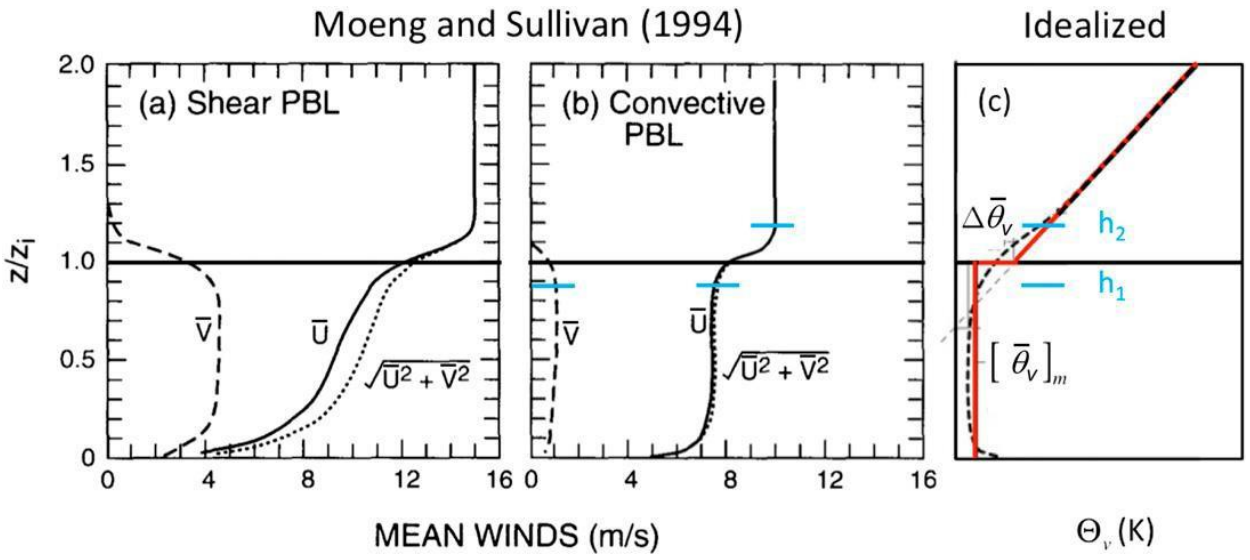

Figure 2.3: Idealised ABL based on LES. (a),(b) Based on ‘‘Shear’’ and ‘‘Convective’’ ABL figure from Moeng and Sullivan (1994). Shear-driven ABL has neutral stratification; convective ABL has $-z_i/L = 18$. (c) The idealised CBL, which can be traced back to Lilly (1968), is based on the schematic from Conzemius and Fedorovich (2006). In the right panel, the red lines correspond to the idealised mixed layer and the jump atop the mixed layer, associated with the so-called zero-order or jump model; U is along the geostrophic wind. (From LeMone et al. 2019)

Figure 2.3 summarises the current understanding of fair-weather CBL. Figure 2.3 (a) indicates mean winds of sheared boundary layers where the wind is constantly turning with height, unlike with the CBL in Figure 2.3 (b) which is marked by constant winds throughout the layer. Figure 2.3 (c) is an idealised CBL thermodynamic structure which shows the often-used definition of the height of the CBL h_1 – where the mean potential temperature starts to increase with height. Figure 2.3 generally indicates the surface layer which corresponds to where potential temperature and winds change with height; the mixed-layer above the surface layer has almost constant values; the transition layer is between h_1 and h_2 where values start to change again to mark the beginning of the free atmosphere. This idealised understanding of CBL agrees well with observation studies by Kaimal et al. (1976) and Clarke et al. (1971) and is universally accepted as representative of the CBL.

2.2.2. Stable boundary layers

SBLs are typically generated during clear-sky night-times or when there is advection of warmer air over a colder surface (Stull 1988). The SBL is sometimes referred to as the nocturnal boundary layer because it mostly occurs during nocturnal stably stratified conditions. In contrast to CBLs, where turbulence is prevalent throughout the boundary layer, and the large eddies help define the boundary layer depth and structure, SBLs have weaker turbulence prevailing at smaller scales and is very sensitive to terrain (Garratt 1994). This has made SBL difficult to observe, study and model – and its subsequent understanding consequently lagged compared to that of the CBL (LeMone et al. 2019). However, in recent decades, there has been an increasing number of observational and modelling studies focusing on the SBL (e.g. Poulos et al. 2002, Persson et al. 2002; Grachev et al. 2005, Mason and Thomson 1992, Sullivan et al. 1994, Bou-Zeid et al. 2005, Chow et al. 2005). Findings from these studies indicate that the SBL can be divided into two main regimes according to the stability of turbulence therein: weakly stable boundary layers and very stable boundary layers. This classification is mainly designed to simplify the understanding of SBL which is otherwise complex and not yet fully understood. Figure 2.4 below illustrates this classification from Mahrt (2014).

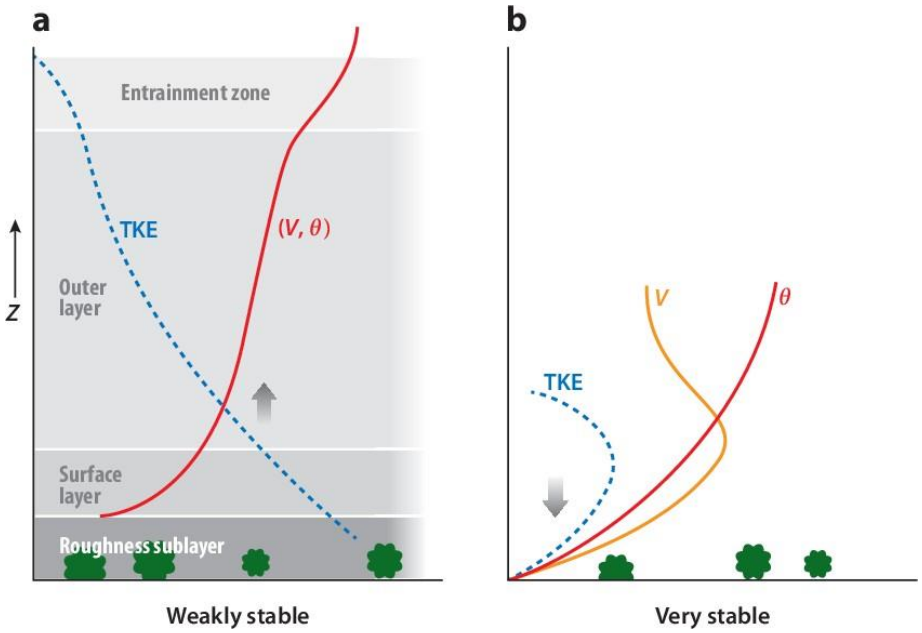

Figure 2.4: A greatly simplified division of boundary layers into (a) the weakly stable regime and (b) the strongly stable regime. (a) Plausible vertical structure corresponding to the relatively well-defined weakly stable regime. The grey zones delineate idealised horizontal layers. The entrainment zone is definable only for the weakest stability. The dashed blue curve depicts the typical height dependence of the TKE. The solid red line represents the general

structure of both the potential temperature, θ, and the wind speed, V. The gradient arrow indicates the usual direction of the vertical transport of turbulence energy. (b) One of numerous different vertical structures for the very stable boundary layer. The red solid curve represents the potential temperature, and the orange solid curve represents the wind speed for the case of a near-surface wind maximum. For very stable conditions, various vertical structures are possible, and the vertical structure is generally nonstationary. In reality, the very stable boundary layer is typically an order of magnitude thinner than the weakly stable boundary layer. (From Mahrt 2014)

As can be seen from Figure 2.4, the weakly stable boundary layer is well defined and can be vertically divided into the roughness sublayer, surface layer, outer layer and the entrainment zone. This is not true for the very stable boundary layer which has an undefined structure, except for the common mean wind and potential temperature profiles. This makes the very stable boundary layer the less understood and the most complex of SBLs.

One important defining feature of the weakly stable boundary layer as seen from Figure 2.4 (a) is the presence of turbulence throughout the layer, which has its maximum near the surface and decreases with height to near-zero at the top of the boundary layer. The near-zero turbulence state at the top of the boundary layer has been found to correspond to the top of the nocturnal inversion and has been used to identify the SBL height (Blackadar 1957). The weakly stable boundary layer typically occurs during cloudy skies and/or significant winds (LeMone et al. 2019). In contrast, the very stable boundary layer typically occurs during clear skies and weak winds, and can be characterised by different vertical structures and scenarios, with turbulence not being statistically well defined (Balsley et al. 2003). However, one important feature frequently seen with very stable boundary layers is the low-level jet often called the nocturnal jet (Figure 2.3(b), Mahrt 2014, Stull 1988).

2.2.3. ABL height climatology

Observation-based global ABL height climatological studies to evaluate weather and climate models are very limited. To the best of our knowledge, Seidel et al. (2010) were the first to attempt such a difficult study on a global scale based on IGRA radiosonde data (Durre et al. 2006). Using seven different methods (i.e. parcel and refractivity methods; and methods based on potential temperature, specific humidity, relative humidity, elevated inversion and surface-based inversion), they computed 10-year climatologies of the ABL height and used these to

quantify uncertainties while also establishing the seasonal and diurnal cycles. Their analyses indicate that standard sounding data resolution tends to yield higher ABL heights compare d to high-resolution data (see Figure 2.5b). This is an indicator that the ABL height parameter is sensitive to the vertical resolution of radiosonde data. Figure 2.5a indicates that the ABL height climatologies they found range between 200 and 2000 m, with potential temperature and relative humidity gradient methods yielding higher ABL heights compared to other methods, and especially the parcel method (and excluding the surface-based inversion which is expected to produce the lowest ABL height compared to all methods), and that the diurnal and seasonal cycles are associated with local climatological events such as tropical convection and night-time radiation inversions.

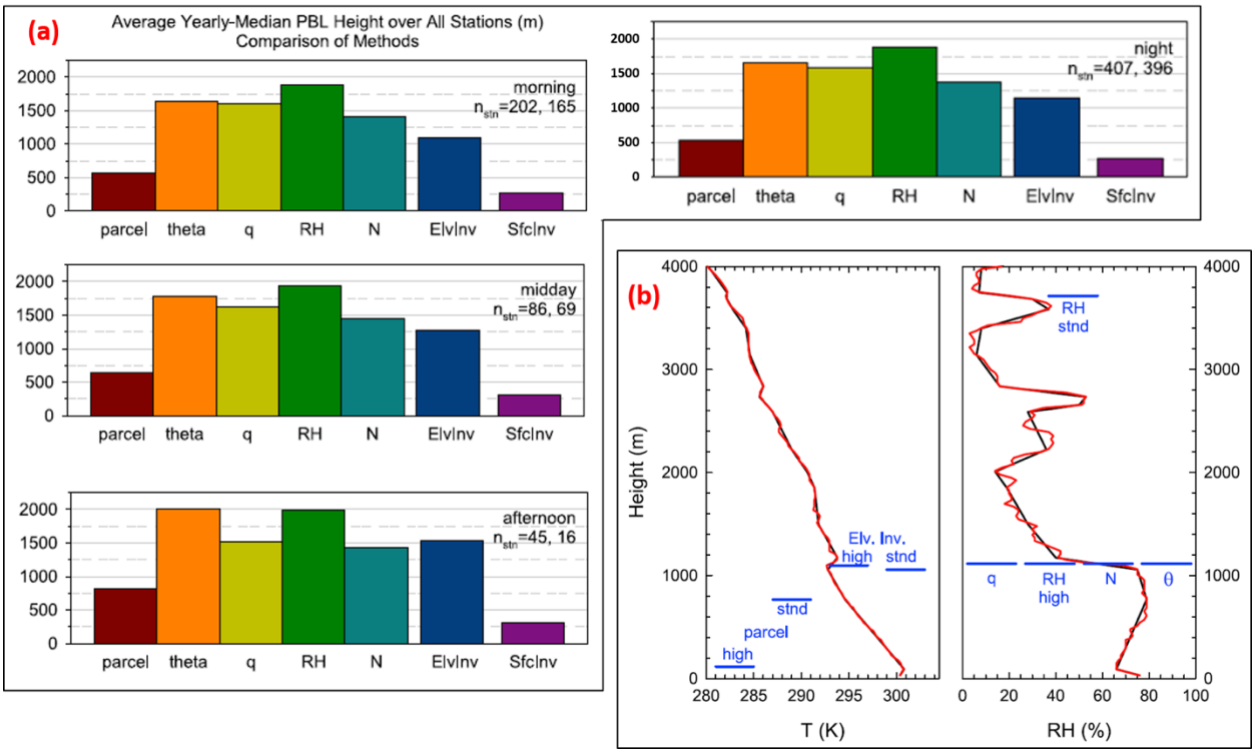

Figure 2.5: (a) Average values (over all stations) of yearly median planetary boundary layer heights estimated using seven different methods. (top to bottom) Results for morning, midday, afternoon, and night-time. The number of stations used to compute each average (n_{stn}) is shown; the first value applies to six methods and the second applies to surface-based inversions. (b) Effect of sounding vertical resolution on estimated ABL heights (m) at Koror Island, Republic of Palau (7°N, 134°E), for the 1200 UTC sounding of 21 February 2007. Standard-resolution and high-resolution (black and red curves, respectively) (left) temperature (K) and (right) relative humidity (%) soundings are shown, along with the ABL heights identified by six methods. For the parcel, elevated inversion, and RH gradient methods, estimated

heights differ for the high-resolution and standard resolution cases. For the q, N, and θ gradient methods, estimated ABL heights are the same. (from Seidel et al. 2010)

Besides the ABL height climatology analyses presented by Seidel et al. (2010) based on global observations, there have been climatological studies of the ABL height conducted on local scales. Some examples include studies by Holzworth (1964, 1967) and Seidel et al. (2013) in the U.S.; Liu et al. (2015), Guo et al. (2016), and Zhang et al. (2018) in Asia; Seidel et al. (2013), Collaud Coen et al. (2014), Pal and Haeffekin (2015) and in Europe; Korhonen et al. (2014) in South Africa and Aryee et al. (2019) in West Africa. Literature indicates that apart from the global study by Seidel et al. (2010), which included stations from South Africa and Southern Ocean, our area of study does not have such extensive climatological characterisation of the boundary layer height.

2.3. HOW WEATHER AND CLIMATE MODELS SIMULATES THE BOUNDARY LAYER

In recent years, weather and climate models have become popular, and somewhat accessible to meteorological and academic institutions in many countries. One direct implication of this accessibility is that, many countries and institutions have developed or modified some of these models to such an extent that each model is typically composed of a unique set of combinations of physics parameterisation schemes. This means that the simulation of the boundary layer itself varies, and depends on the model of choice. Therefore, in this section we only describe literature based on foundational blocks required to simulate the boundary layer.

At a foundational level, boundary layer modelling seeks to represent the evolution and dissipation of turbulence. However, the turbulent mixing within the ABL occurs at short time and length scales (order of minutes and metres) compared to the free atmospheric flow. Therefore the effects of boundary layer turbulence to the resolved model dynamics is parameterised. This is done through modelling various processes occurring within the boundary layer, and those involved in the transport and entrainment at the bottom and top of the layer.

As already mentioned in Chapter 1, the concept of parameterisation is applied to model the ABL because the primitive dynamical equations representing atmospheric circulation do not explicitly resolve turbulence. There are five fundamental equations important for ABL modelling. These are the equation of state, and the conservation equations for mass, momentum, moisture, and heat (Holton and Hakim 2013). Looking at how each of these

governing equations is used in modelling the ABL is beyond the scope of our research. However, to illustrate how weather and climate models typically parameterises the ABL, we use an example of an atmospheric tracer A which can represent any scalar quantity. The conservation of tracer A mass in cartesian coordinates requires that (Stull 1988),

$$\frac{\partial A}{\partial t} + U\frac{\partial A}{\partial x} = v_A\frac{\partial^2 A}{\partial x^2} + S_A \tag{2.1}$$

where v_A represents the molecular diffusivity of tracer A and S_A represents the body source term for the remaining processes not already in the equation. The physical interpretation of Equation (2.1) is similar to those of basic primitive equations. The first, second and third terms respectively represents the storage, advection and molecular diffusion terms. As the example represented by Equation (2.1) is non-specific, It is important to include the fourth term to account for any processes not represented in the equation – such as chemical reactions if tracer A represented a pollutant of some sort. Expanding Equation (2.1) into its mean and turbulent parts, and then applying Reynolds averaging, together with using the turbulent continuity equation to put the turbulent advection term into flux form results in,

$$\frac{\partial \bar{A}}{\partial t} + \frac{\bar{U}\partial \bar{A}}{\partial x} = \frac{\nu_A \partial^2 \bar{A}}{\partial x^2} + \bar{S}_A - \frac{\partial(\bar{\vec{u}}\bar{\vec{a}})}{\partial x} \tag{2.2}$$

where the first to fourth terms have similar interpretations as in Equation (2.1), except that they represent the mean flow. This means that Equation (2.2) represents mean variables of Equation (2.1) in a turbulent flow. Hence after expanding Equation (2.1) into its mean and turbulent parts, a fifth term now appears which represents the divergence of turbulent tracer flux. Equation (2.2) is an example of how a model forecast equation of a variable, like mean moisture, would look like when it includes its turbulent part. The turbulent part is normally ignored in the free atmosphere as it is usually negligible. However, the turbulent part is retained in the ABL as it plays a major role in the vertical transport of heat, moisture and momentum as represented by eddies. This means that the forecast equation of a variable has to also calculate the turbulent state of the atmosphere within the boundary layer.

In theory, the prognostic equation of the turbulent part of the mean variable A, namely a', could be used to calculate it, if accurate initial and boundary conditions are given. However, Stull (1988) notes that the time span over which such a forecast is likely to be accurate is proportional to the lifetime of the eddy itself, which is in the order of a few seconds for the smallest eddy to about 15 minutes for the larger eddies. In an operational environment, this is costly and impractical. Also, the divergence term of turbulent flux, $\bar{\vec{u}}\bar{\vec{a}}$, contained in Equation (2.2) is unknown. If a prognostic equation of this turbulent flux can be found, then it would be

possible to determine the boundary layer mean and turbulence state. However, deriving equations of unknown fluxes leads to further unknown terms. Therefore, the use of turbulence closure technique is essential in boundary layer modelling.

As already mentioned in Chapter 1, there are two approaches to turbulence closure: the local and non-local approaches. In our example, Equation (2.2) indicates that the unknown is a turbulent flux of second statistical moment $\overline{\overline{u}'\overline{a}'}$, which must be parameterised to close the equation. A first order local closure approach from Equation (2.2), in which the sub-grid scale turbulent, kinematic flux of tracer A is taken proportional to the local gradient of the transported quantity is formulated in the vertical as

$$\overline{\overline{w}'\overline{a}'} = -K_A \frac{\partial A}{\partial z} \tag{2.3}$$

where K_A is an eddy diffusivity for A, and typically depends on local gradients of mean wind and mean virtual potential temperature. The non-local formulation of tracer A in Equation (2.2) takes into account the non-local transport γ_A and is formulated as

$$\overline{\overline{w}'\overline{a}'} = -K_A \left(\frac{\partial \overline{A}}{\partial z} - \gamma_A\right) \tag{2.4}$$

In theory, there is an indefinite number of orders from which lower or higher orders of parameterisation schemes can be formulated, but first order (K-theory schemes) and one-and-half order (TKE schemes) parameterisations are often used in weather and climates models (Stull 1988, Lock et al. 2000, Janjić 2001, Banks et al. 2016).

CHAPTER 3: ESTABLISHING A PRESENT-DAY SEASONAL CLIMATOLOGY OF ABL ATTRIBUTES IN THE SOUTHERN HERMISPHERE

3.1. INTRODUCTION

Radiosondes are some of the most important observational measures in the atmospheric sciences as they capture the vertical structure of the atmosphere. They are also the most common source of data for operational determination of the boundary layer height (Seibert et al. 2000). One example of how boundary layer height is computed operationally from radiosondes is from Sivaraman et al. (2013), who routinely determine the mixing height (that is, the boundary layer height) as part of the value-added product of the Atmospheric Radiation Measurement program of the U.S. Department of Energy. Not only are radiosondes data valuable for operational determination of the mixing height (for both weather forecasting and air quality monitoring), they are also important for local and global climatological studies of the boundary layer height as demonstrated by Seidel et al. (2010).

Radiosondes are launched at stations around the globe at least once daily, or twice at 00:00 UTC and 12:00 UTC as mandated by the WMO. As they are launched from the surface and ascend up to the stratosphere, they transmit data back to their release stations where they are processed into pressure, geopotential height, temperature, dewpoint depression, wind speed and direction. These meteorological data are measured at mandatory pressure levels as specified by WMO (1996). These mandatory pressure levels are: 1000, 925, 850, 700, 500, 400, 300, 250, 200, 150, 100, 70, 50, 30, 20, and 10 hPa. Most sondes also measure data at additional levels and significant levels (where there are local thermodynamic and/or wind data extrema). After radiosonde data are received by launching stations, they are compiled into a report and transmitted through the Global Telecommunication System (GTS), as a binary-coded message, to different regional and national meteorological centres around the globe (WMO 1996). To determine a present-day climatology, and seasonality, of the boundary layer height in the Southern Hemisphere, this study uses upper-air sounding data from measurements obtained using radiosondes.

3.2. DATA AND METHODS

3.2.1. IGRA 2 Dataset

The specific global archived radiosonde data we use in this research project are obtained from the IGRA 2 (Durre et al. 2016). There are other global-scale archived radiosonde datasets available from reanalysis projects (e.g. Kalnay et al. 1996, Uppala 2005), and NOAA-NCDC's

CARDS (Eskridge et al. 1995). The University of Wyoming also provides access to their global archive of upper-air sounding data going as far back as 1973 through their Wyoming Weather Web (http://weather.uwyo.edu/upperair/sounding.html). The reason why IGRA 2 datasets were selected over others, is due to their user-friendly format, moreover, they are also easy-to-access and download. Besides their easiness to use, quality control algorithms have also been applied to the IGRA 2 data to remove any gross errors (Durre et al. 2006), making them less tedious to pre-process and quality control for the research. Table 3.1 below summarises the plausibility limits used by the quality assurance algorithms applied to the IGRA 2 dataset.

Table 3.1: Plausibility limits used in basic validity checks (from Durre (2016)).

Item (Field)	**Valid Range**
Elapsed time	0 - 240 min
Pressure	1090 – 0.1 hPa
Geopotential Height	-1000 to 60,000 m
Temperature	-120 to 60 °C
RH	0 - 100%
Dewpoint Depression	0 to 70 °C
Wind Speed	0 – 150 m/s
Wind Direction	0 - 360°

IGRA 2 data is maintained, archived and distributed by NOAA's NCEI, and go as far back as 1905 and are constructed from 33 sources (for a comprehensive list of these sources check Table 3.2 from IGRA 2 dataset description documentation by Durre (2016) currently accessible here: https://www1.ncdc.noaa.gov/pub/data/igra/igra2-dataset-description.docx).

3.2.2. Study Area

The IGRA 2 dataset was obtained for the period starting at 00h00 UTC on 1 January 1979, to 12h00 on 31 December 201,7 for 3 stations in the Southern Hemisphere. This means the data covers 14244 days and 12 hours, which is about 38 years. This time period is sufficient to undertake a comprehensive climatological study. The 3 stations included in our study are Irene in South Africa, Marion Island in the Midlatitude, and Syowa located in the edge of Antarctica and Southern Ocean (See Figure 3.1 for a spatial map showing the stations). These 3 stations

were selected to sample the Southern Hemisphere, stretching from South Africa (low subtropical latitudes) to Antarctica (high latitudes). The reason we chose these three study sites is because we want to study climate model performance in terms of representing climates in three vastly different regions of the Southern Hemisphere. These were selected to be in more or less a zonal line, so that the differences in climates can be mostly explained by latitude (e.g., subtropical vs mid-latitude vs high-latitude).

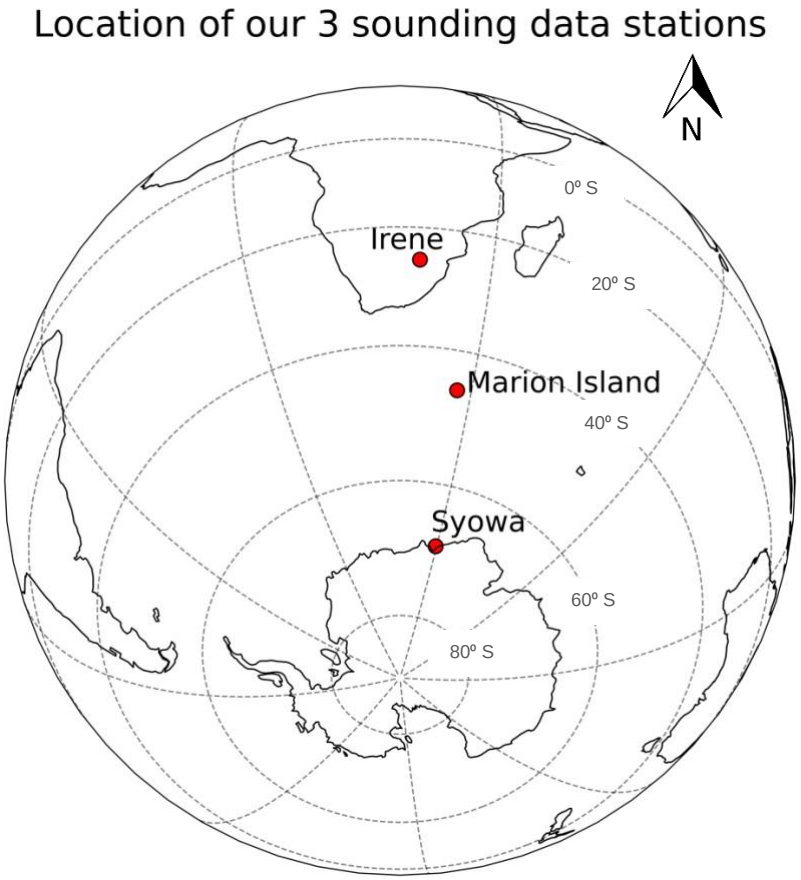

Figure 3.1: Spatial map showing stations where radiosonde data is obtained for our study.

3.2.3. Deriving Additional Parameters

The sounding data include primary variables of temperature, dewpoint depression, pressure, geopotential height, wind speed and direction. Before quality control of the data was undertaken, additional parameters were derived at each level of the sonde. These new parameters are simply added to the original data without manipulating or transforming it.

Using the original IGRA 2 data, the first step was to convert all the parameters to the International System of Units (SI units). We then derive the following new parameters: dewpoint temperature, relative humidity, potential temperature, and temperature lapse rates. Dewpoint temperature is simply derived from the given dewpoint depression by subtracting 273.15 K. We then use temperature (T) and dewpoint temperature (T_d) to calculate relative

humidity (RH) as the ratio of vapour pressure (e) to saturation vapour pressure (e_s) as shown by the Clausius-Clapeyron equation

$$RH = \frac{e(T_d)}{e_s(T)} \tag{3.1}$$

To calculate the potential temperature (θ), given pressure (P) and temperature (T), we use the Poisson equation

$$\theta = T\left(\frac{P_0}{P}\right)^{\kappa} \tag{3.2}$$

where $\kappa = 0.286$ and P_0 is the reference pressure of 1000 hPa.

The temperature lapse rate is calculated as

$$\Gamma = -\frac{dT}{dz} \tag{3.3}$$

where T is the temperature in ℃ and z is the height in km.

3.2.4. Quality Control Algorithm

Although IGRA 2 dataset is quality controlled, it is necessary that we conduct another quality control (QC) check to ensure that the data is adequate for our particular boundary layer study. Before we use the radiosonde data (which includes newly derived parameters as discussed in Section 3.3.2), we apply a set of QC algorithms to identify sondes or data points in sondes which may erroneously impact our ABLH determination. The QC checks used are adapted from those of Seidel et al. (2010) and Sivaraman et al. (2013). If any of the following 7 QC checks are true, then the sonde is flagged as bad and not used in the ABLH determination:

3.2.4.1. Upper air data points below 500 hPa < 10
3.2.4.2. Maximum pressure value ≤ 200 hPa
3.2.4.3. Pressure value in the first two levels missing or bad
3.2.4.4. Maximum sonde altitude < 1000 m
3.2.4.5. Wind speeds at altitudes less than 50 m AGL > 33.5 m/s
3.2.4.6. Maximum temperature > 50 °C or minimum temperature < -90 °C
3.2.4.7. Temperature changes by more than 30 °C in the first 5 hPa of the sounding (For high-resolution data)

During the QC process, data points within a sonde that are missing, or do not meet valid minimum or maximum criteria, are set to a default value of -9999 which indicates a QC flag for that particular data point. Figure 3.2 is a flow chart summarising our ABLH computation

algorithm, and includes the QC checks done prior to that. However, not shown in the flowchart is the fact that before we determine the ABL stability and height, we do a vertical interpolation after the QC check process, the method being explained in Section 3.3.4.

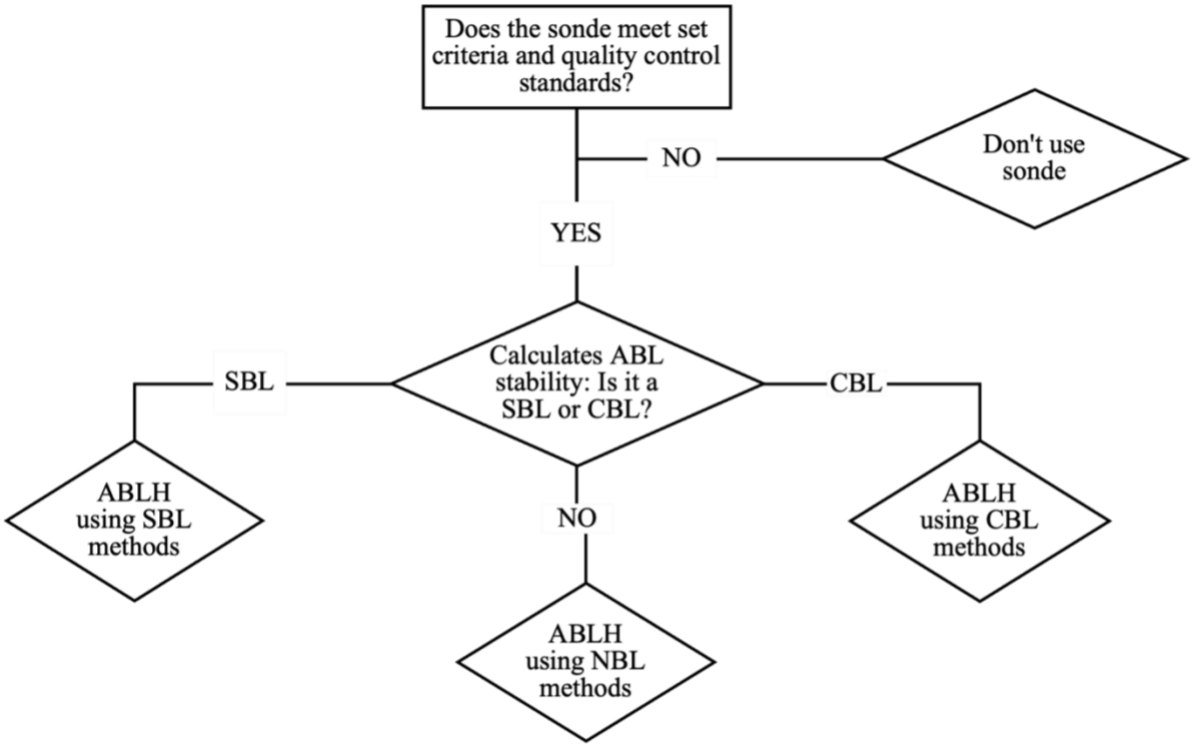

Figure 3.2: Flowchart summarising our ABLH computation algorithm, including QC checks done.

As an example of why it is necessary to do our QC checks with the IGRA 2 data to ensure it meets good standards for ABLH determination, consider the QC check on Section 3.3.3.1 which states that upper air data points below 500 hPa must not be less than 10 for the sonde to be considered. This check is there to ascertain that all sondes undergoing vertical interpolation and subsequent ABLH computations, have enough data points. This helps with reducing biases in the climatological analysis. Continuing with the example above, now consider Figure 3.3 below, showing radiosonde data (which includes newly derived parameters as discussed in Section 3.3.2). The shown data is from a sonde which was flagged by our QC check for data points below 500 hPa, dated 3 January 1979 at 00h00 UTC, from the Irene station.

datetime	pressure	height	temperature	dewpoint	theta	RH	speed	direction	u_wind	v_wind	lapse_rate
1979-01-03	846.0	1525.0	291.35	284.35	305.609146	63.644526	15.4	120.0	-13.3	7.7	6.198378
1979-01-03	700.0	3121.0	286.35	269.35	317.069808	30.460178	14.4	155.0	-6.1	13.1	5.770568
1979-01-03	500.0	5840.0	266.45	245.45	324.806188	17.064661	11.8	200.0	4.0	11.1	7.112215
1979-01-03	400.0	7550.0	254.85	233.85	331.117232	14.017610	15.9	270.0	15.9	0.0	7.619048
1979-01-03	300.0	9620.0	237.65	221.65	335.221408	17.838411	12.3	245.0	11.1	5.2	7.903469
1979-01-03	250.0	10865.0	228.65	192.65	339.772594	0.843586	11.3	250.0	10.6	3.9	7.851852
1979-01-03	200.0	12320.0	216.45	NaN	342.817754	NaN	16.4	250.0	15.4	5.6	6.945736
1979-01-03	150.0	14090.0	206.25	NaN	354.647134	NaN	20.1	240.0	17.4	10.1	4.316547
1979-01-03	100.0	16490.0	198.45	NaN	383.146964	NaN	20.1	235.0	16.5	11.5	7.361719

Figure 3.3: Radiosonde data which was flagged by QC check used to determine if the sonde's upper air data points below 500 hPa are less than 10. This is an example of a sonde which was flagged as bad and therefore excluded in our interpolation and ABLH calculations. This sonde is from Irene station and dated 00h00 UTC 3 January 1979.

The sonde captured in Figure 3.3 clearly indicates that the number of data points below 500 hPa pressure level is only 2, of which their pressure is respectively 700 and 846 hPa. The altitudes for the 500, 700 and 846 hPa pressure levels, above ground level, are respectively 2719 m, 1596 m and approximately the surface level. The data gaps between those levels are at least 1000 m, making it impossible to reliably interpolate at the desired resolution of 50 m (the interpolation scheme is discussed in the next Section 3.3.4), and subsequently determine the ABLH. Figure 3.4 indicates plots of parameters shown in Figure 3.3, from the surface up to 14 000 m into the atmosphere. Figure 3.4 indicates that, although general patterns within the entire troposphere follow the theoretical understand of how these parameters change with height, it is difficult to analyse what is happening below 500 hPa (4315 m height in this example) as there are only 2 points, one at the surface and the other at 700 hPa (1596 m height in this example). Including sondes like these, will affect our climatological analyses, hence the QC check flags them as bad and excludes them from our computations.

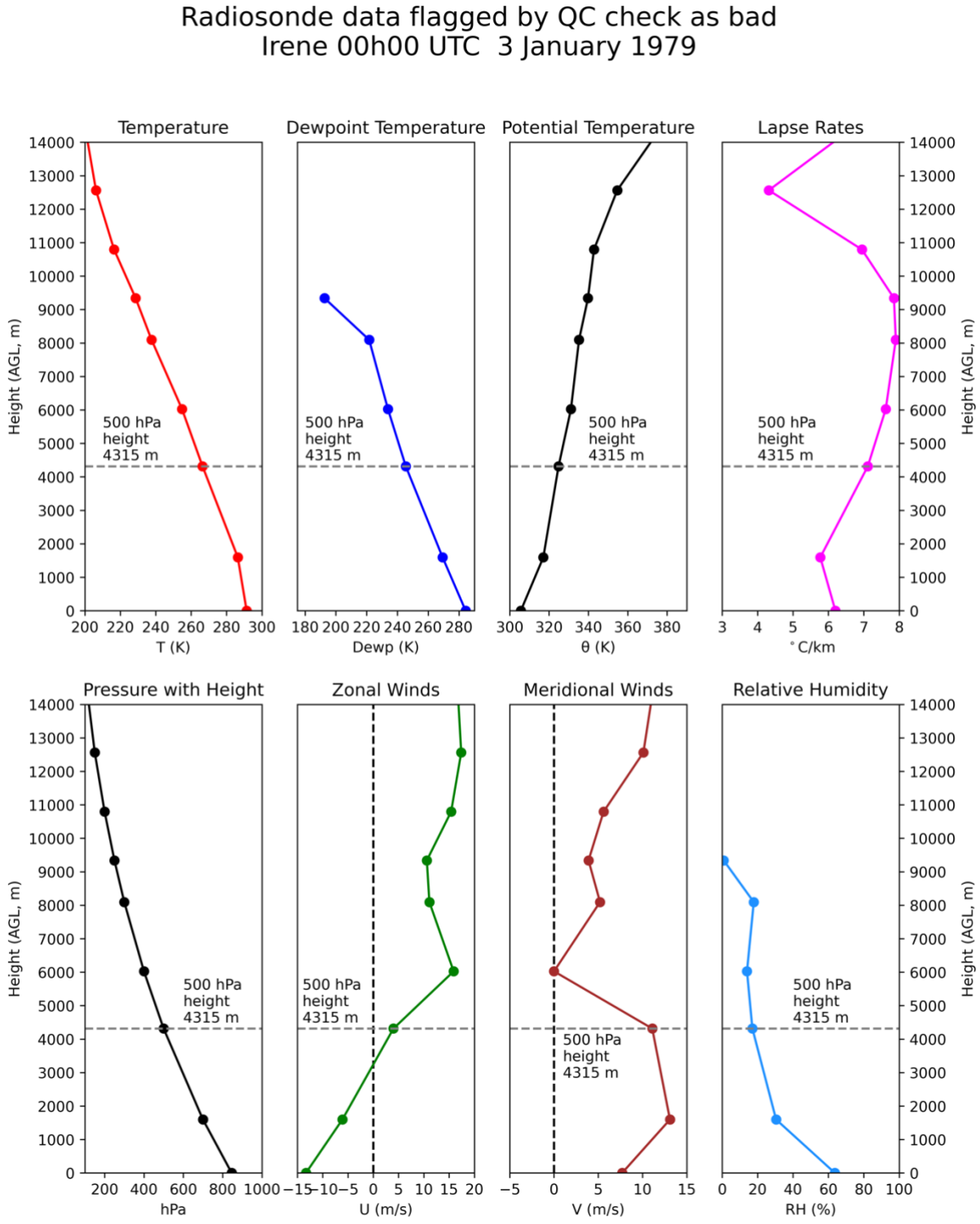

Figure 3.4: This is an example of radiosonde data which was flagged as bad by our QC check algorithm and therefore excluded in our interpolation and ABLH calculations. This illustrates that analysing data below 500 hPa and ABL will be difficult as there are only 2 data points below this level. This sonde is from Irene station and dated 00h00 UTC 3 January 1979.

3.2.5. Vertical Interpolation of the Quality Controlled Data

Radiosonde data that passes our QC checks is vertically interpolated to standard height levels before being used in climatological computations and seasonal variability analysis. The vertical linear interpolation algorithm being used in this study determines the values of parameters corresponding to height values, which have been fixed from the surface up to 5000 m into the atmosphere. This is done at an interval of 50 m. To illustrate how this works, consider the following x and y data points in Table 3.2.

Table 3.2: Data points showing x and y variables. x is the independent variable, and y is the dependent variable.

x:	x_0	x_1	x_2	x_3	$\cdots$	x_n
y:	y_0	y_1	y_2	y_3	$\cdots$	y_n

Consider data points x and y in Table 3.2. To interpolate values of dependent variable y at some point of independent variable x using linear Interpolation, say between x_0 and x_1, we take two points $[x_0, y_0]$ and $[x_1, y_1]$, and construct linear Interpolants by fitting a straight line between them. Mathematically, this can be represented as

$$\frac{y-y_0}{x-x_0} = \frac{y_1-y_0}{x_1-x_0} \tag{3.4}$$

This means to determine the interpolated value of y (e.g. temperature) at an independent point x (e.g. fixed height) between x_0 and x_1, given original points y_0 and y_1, we can rearranged Equation (3.4) such that

$$y = y_0 + (x - x_0)\frac{y_1-y_0}{x_1-x_0} \tag{3.5}$$

This linear interpolation scheme works well for our vertical interpolation of radiosondes. To demonstrate this, we use an example where we compare it with three other popular interpolation techniques commonly used to interpolate 1-Dimensional functions. These are quadratic, cubic and nearest-neighbour interpolation schemes. For our example, consider the following radiosonde data from Marion Island, which passed our QC checks. It is dated 14 January 1979 at 12h00 UTC. We only consider levels between the surface and 500 hPa, as these are the ones near or within the boundary layer.

datetime	pressure	height	temperature	dewpoint	theta	RH	speed	direction	u_wind	v_wind	lapse_rate
1979-01-14 12:00:00	996.0	22.0	280.35	273.35	280.671226	61.080737	11.3	315.0	8.0	-8.0	3.281915
1979-01-14 12:00:00	950.0	407.0	275.15	266.15	279.212078	51.327001	15.4	290.0	14.5	-5.3	2.077922
1979-01-14 12:00:00	906.0	792.0	278.75	255.75	286.723944	17.254970	20.1	280.0	19.8	-3.5	-0.220751
1979-01-14 12:00:00	850.0	1313.0	275.35	262.35	288.437088	37.594520	13.9	255.0	13.4	3.6	5.939788
1979-01-14 12:00:00	778.0	2021.0	271.45	257.45	291.634254	33.501248	8.2	240.0	7.1	4.1	4.381245
1979-01-14 12:00:00	722.0	2614.0	269.65	265.55	295.950016	73.228345	22.1	260.0	21.8	3.8	4.062127
1979-01-14 12:00:00	700.0	2858.0	268.05	263.45	296.806573	70.110796	29.8	260.0	29.3	5.2	3.890160
1979-01-14 12:00:00	646.0	3488.0	266.25	260.25	301.653867	62.302719	34.0	255.0	32.8	8.8	5.246253
1979-01-14 12:00:00	550.0	4726.0	258.25	255.25	306.353198	77.857588	28.8	255.0	27.8	7.5	6.591143
1979-01-14 12:00:00	500.0	5430.0	253.45	246.45	308.959011	53.754308	29.3	255.0	28.3	7.6	7.056799

Figure 3.5: Radiosonde data from Marion Island dated 14 January 1979 at 12h00 UTC. This is one of the radiosondes data which passed our QC checks and therefore used in our study.

The interpolation is done for all the meteorological variables in Figure 3.5, but for our example we only consider temperature. Height is the independent variable. In order to do the interpolation, we first create standard heights we want to interpolate to, at an interval of 50 m, from the surface to 5000 m. Using temperature values at original heights, we then calculate new temperatures at standard heights using the linear, quadratic, cubic and nearest-neighbour interpolation techniques. The results of these interpolations are shown on Figure 3.6.

Figure 3.6 shows plots of data before being interpolated (as in Figure 3.5) and the data after being interpolated using the linear interpolation method as represented by Equation 3.5 and the three other popular interpolation techniques commonly used to interpolate 1-Dimensional functions – quadratic, cubic and nearest-neighbour interpolation schemes. The original temperature plot clearly shows a decrease in temperature, with height, from the surface until below 500 m, from which there is a temperature inversion to up until about 800 m. Temperature then decreases with height to well beyond 5000 m.

Now consider the interpolated temperature plots alongside the original. By looking at the plots we can easily dismiss the use of the nearest-neighbour interpolation as it does not follow the pattern of the original temperature, and is discontinuous. This is because the newly calculated temperature only takes values of existing temperature nearest to it. Now, looking at the quadratic and cubic interpolation plots, it would be plausible to use them because they seem to follow the pattern of the original temperature, and are also smoother. However, the values between points seem to be less predictable, as indicated by the bulges at sharp temperature changes, below and above the temperature inversion. Looking at the linear interpolation plot, it can be seen that it is the closest pattern to the original temperature, and reproduces the temperature inversion with as much detail as the original data. This is because the newly

interpolated temperatures, at standard heights, stays in the limits of the original temperature. Hence, we use the linear interpolation method in our study.

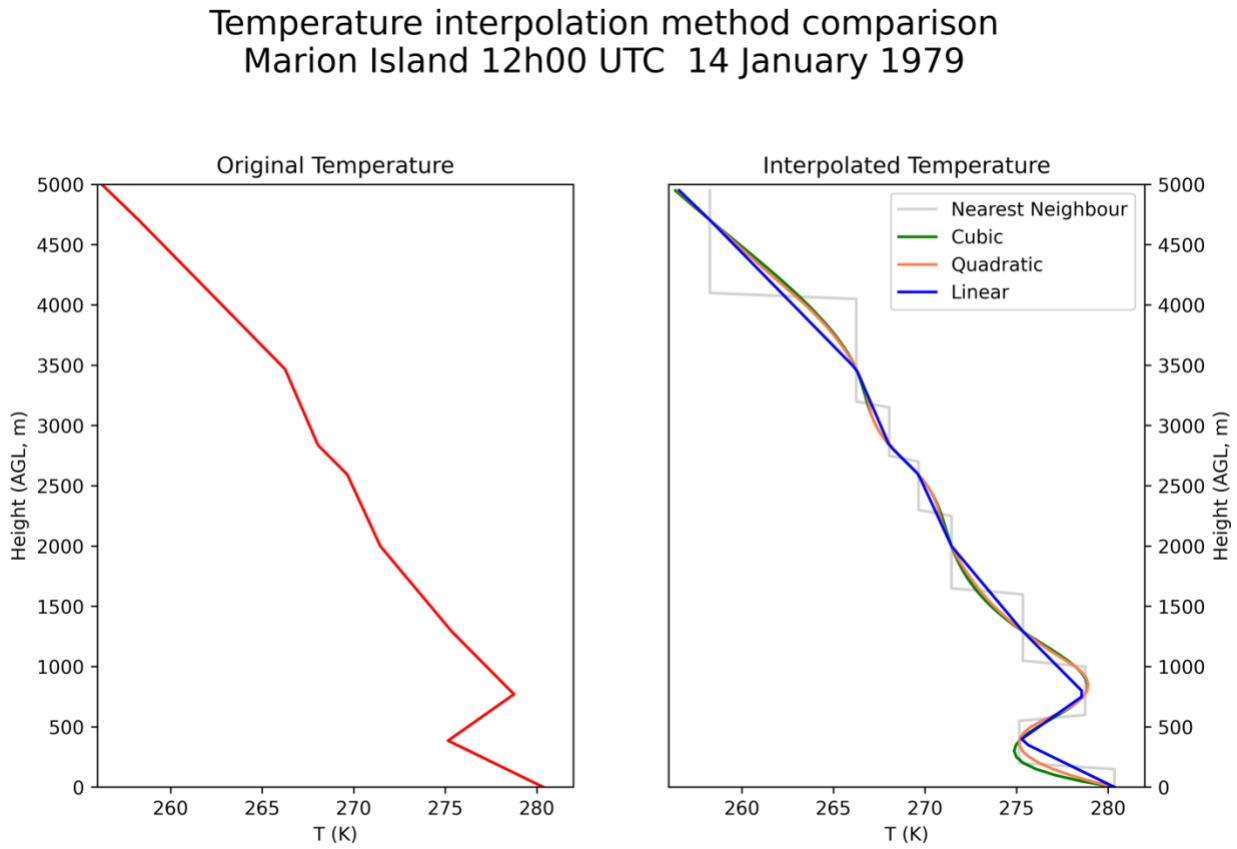

Figure 3.6: The Figure shows plots of data before being interpolated (as in Figure 3.5), and the data after being interpolated using the linear interpolation method as represented by Equation 3.5 and the three other popular interpolation techniques commonly used to interpolate 1-Dimensional functions – quadratic, cubic and nearest-neighbour interpolation schemes.

3.2.6. Computation of the ABLH and its Climatological and Seasonal Variability

To determine the ABLH from the interpolated radiosondes data we follow a well-established and widely used method, which defines the ABLH as the level of the maximum vertical gradient of potential temperature (Oke 1988, Stull 1988, Sorbjan 1989, Garratt 1992). This is calculated as

$$max\left(\frac{\partial\theta}{\partial z}\right) \tag{3.5}$$

where z is the height and θ is the potential temperature. The reason this location is used to define the boundary layer height is because it indicates a level of transition from a convectively

less stable region below to a more stable region above (Seidel et al. 2010). Sullivan and Patton (2011) indicated that PBL height determined in this manner represents the average height reached by the thermals. The potential temperature gradients are calculated for each radiosonde ascent during the calculation of additional variables as discussed in Section 3.3.2. We then find the maximum of these gradients to calculated the ABLH for each radiosonde, from which we calculate monthly and seasonal climatologies for 00h00 UTC and 12h00 UTC.

There are two exceptions to this definition of the ABLH in our study. The first exception is when there exists a temperature inversion which is a clear indicator of a stable boundary layer immediately above the surface, with the top of it representing the ABLH (Bradley et al. 1993). The second exception is when the bottom of the boundary layer is convective – that is when the potential temperature decreases with height immediately above the surface. In that case we use the parcel method to define the ABLH, which is also well established (Seibert et al. 2000).

3.3. RESULTS

The results of the analysis of the radiosonde data are divided into three main sections. Section 3.4.1 discusses the analysis of the Irene datasets, starting with the subsection focusing on the meteorological variables according to their monthly and seasonal climatologies for both 00h00 and 12h00. The second subsection focuses on the ABLH monthly and seasonal climatologies. Section 3.4.2 and Section 3.4.3 follows the same format of analysis, but are respectively for Marion Island and Syowa stations.

3.3.1. Irene Station

3.3.1.1. The September to November (SON) season and climatology for 00h00 and 12h00

The austral spring temperature profiles of Irene at 00h00 (see Figure 3.7) shows that there persistently exists a temperature inversion for all the three months (September, October and November). This corresponds well with negative lapse rates near the surface, with September and October respectively indicating highly negative lapse rates compared to November. The seasonal mean of lapse-rates follows the same pattern as that of October, meaning that the October month is representative of mean spring lapse-rate patterns, at least from near the surface up to a height of about 300 m. This is also true for temperature, except that the seasonal mean follows the same pattern as the October month throughout the lower troposphere.

The results showing October as representative of the mean spring patterns are also found for dewpoint temperature, potential temperature, zonal and meridional winds, and relative humidity. Interestingly, meridional winds seem to reach their maximum at a height where winds start to become westerly. Both these are indicative of low-level directional and speed shearing, located at about 500 m. The change in pressure with height is the same throughout the season.

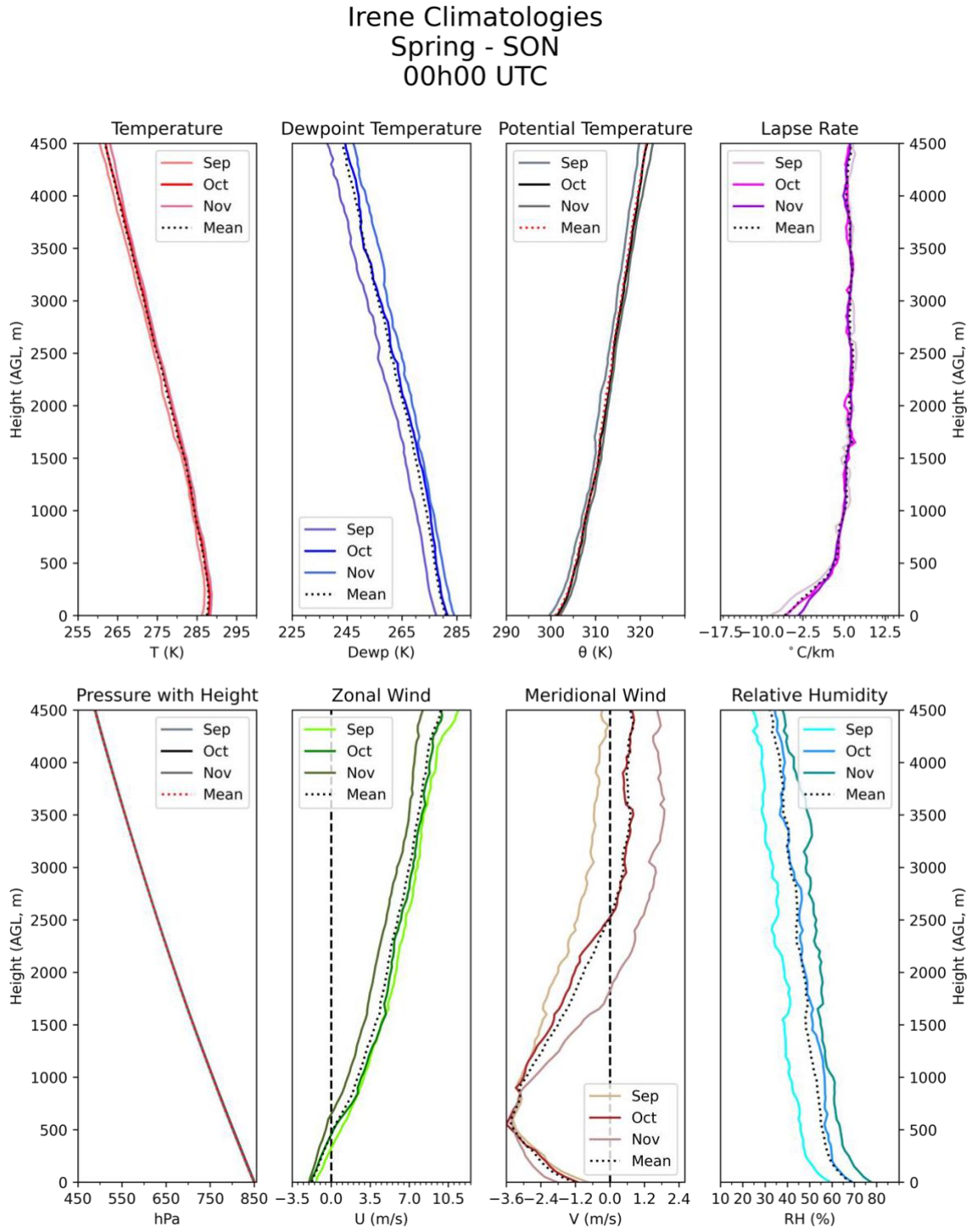

Figure 3.7: Irene radiosonde observation climatologies for the months of September, October and November (austral spring) at 00h00 UTC. The seasonal mean is also included for each parameter.

Potential temperature profiles for spring in Irene at 12h00 (see Figure 3.8) decrease with height from just above the surface to about 500 m, which is an indicator that the boundary layer near the surface is unstable. This is especially observed for the month of September (early spring). It is interesting to note that the temperature profile for the month of September also indicates the presence of an inversion at a height of 1600 m, which would represent the ABLH if defined according to the elevated temperature inversion. However, the parcel method used indicates an ABLH of 1525 m (see Figure 3.15), which corresponds to the level at which the potential temperature equals that of the surface. Temperature lapse-rates near the surface are high, about 15 °C/km, which is also true for all the months and seasons at 12h00. Above 500 m, temperature lapse-rates range between 5 and 7 °C/km.

Relative humidity observations in Figure 3.8 indicate pronounced variability throughout the spring season. Early-spring (September) is relatively drier than late-spring (November). It is also important to note the same pronounced variability between early- and late-autumn (March and May), while winter and summer do not have much variability (see Figure 3.7 to Figure 3.14) for both 00h00 and 12h00. It is also interesting to notice a relative humidity bulge which starts at the bottom of the lower troposphere to the middle lower troposphere. This is also true for all seasons at 12h00, but is especially noticeable for the summer and winter months (compare with Figure 3.10 and Figure 3.14). The zonal and meridional winds for the three spring months, are almost similar from the surface up to the level of elevated temperature inversion for zonal winds (1600 m), and about 1000 m for meridional winds.

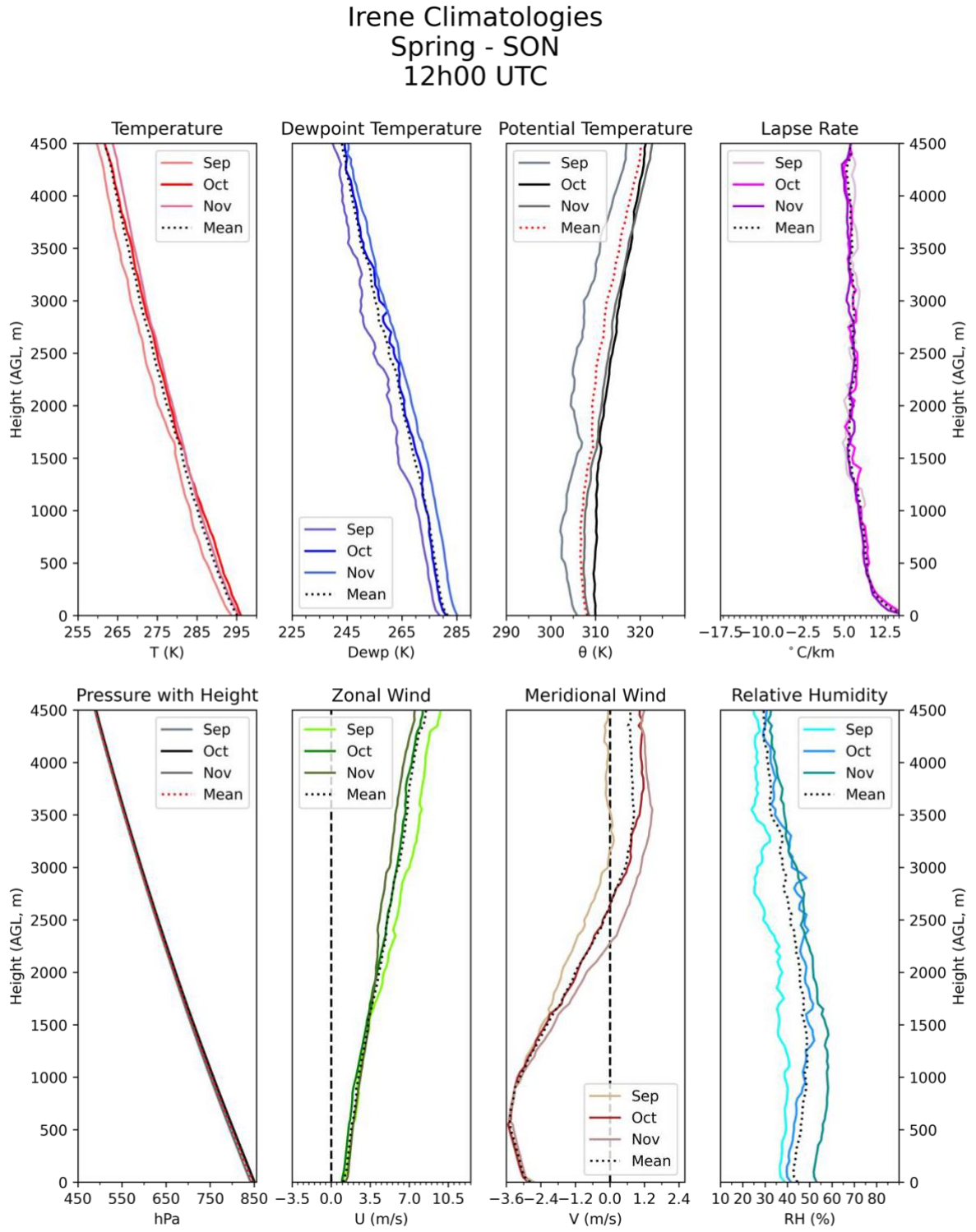

Figure 3.8: Irene radiosonde observation climatologies for the months of September, October and November (austral spring) at 12h00 UTC. The seasonal mean is also included for each parameter.

3.3.1.2. The DJF season and climatology for 00h00 and 12h00

Figure 3.9 indicates meteorological parameters for the austral summer season at 00h00 UTC. As with all the other seasons at 00h00 UTC, there is a temperature inversion above the surface, which corresponds with negative lapse-rates (indicating an increase in temperature with height). Potential temperature profiles show that the layer below the inversion is stable, while Figure 3.15 shows that the ABLH is at the level of inflection of temperature. Interestingly, relative humidity decreases rapidly with height from the surface to the inversion height, then it becomes steady. It should be noted that potential temperature profiles for January indicates a near-neutral atmosphere above the inversion height up until about 1000 m. This is also true for the month of April (see Figure 3.11). Zonal and meridional winds also show the change in direction at about 1500 m, with meridional winds also marked by a reversed S-shape pattern. The temperature, dewpoint temperature, temperature lapse-rate, pressure and relative humidity indicates similar patterns for the three summer months at 00h00, which means that there is not much variability of these parameters over the summer months.

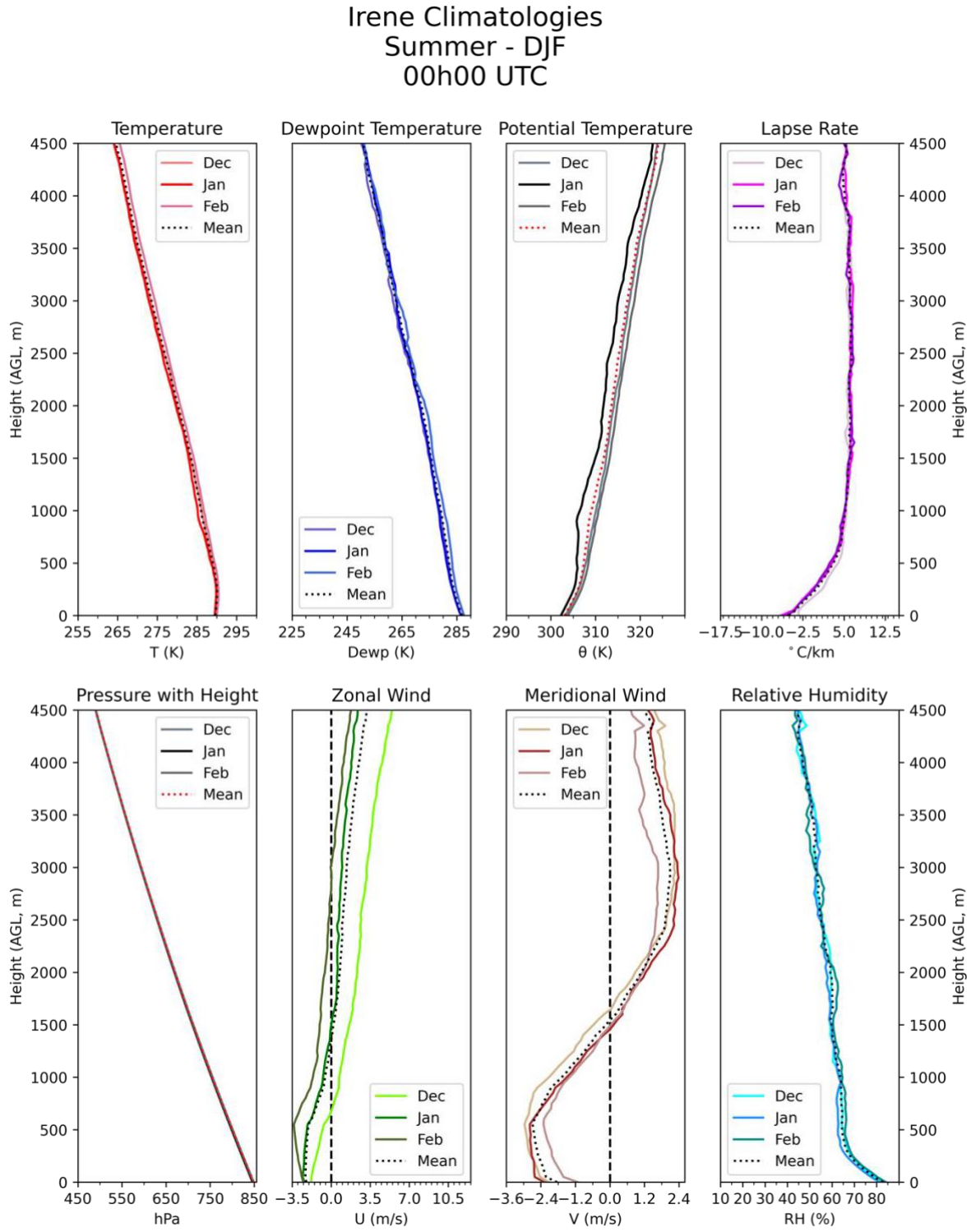

Figure 3.9: Irene radiosonde observation climatologies for the months of December, January and February (austral summer) at 00h00 UTC. The seasonal mean is also included for each parameter.

Figure 3.10 indicates that the summer months are noticeably marked by a relative humidity bulge above the surface, with their values being almost similar below the bulge. The potential

temperature decreases with height near the surface, and starts to increase from 500 m. It is also almost similar across the different months, and follows the same pattern throughout the season. This indicates that the near-surface atmosphere is unstable during the summer season at 12h00 UTC. Temperature lapse-rate follows the same pattern, except in January near the surface. Throughout the depth of our analysis, and above 500 m, lapse-rate values are between 6.5 °C/km and 9.8 °C/km, indicating an atmosphere that is conditionally unstable throughout the season.

As with the 00h00 UTC summer season observations, the 12h00 UTC also indicates the reversed S-shaped meridional winds, but with much variability especially for the December month. Zonal winds are almost 0 m/s for the months of January and February, implying that during these two months, wind speeds and directions are highly driven by meridional flows. The temperature profiles indicate that during the summer months, the change in temperature with height is almost similar across the different months, and that the patterns for all the months follows the mean pattern.

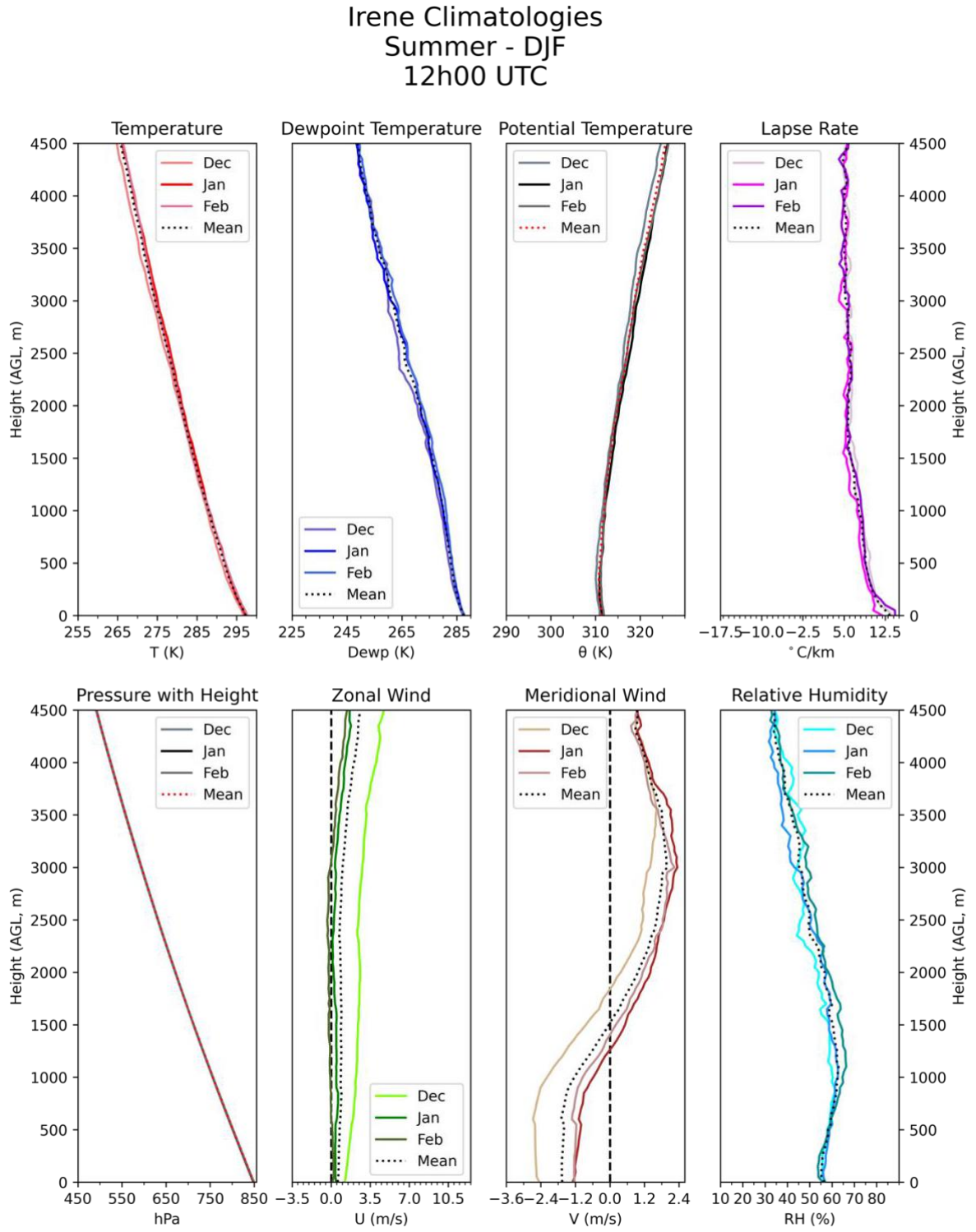

Figure 3.10: Irene radiosonde observation climatologies for the months of December, January and February (austral summer) at 12h00 UTC. The seasonal mean is also included for each parameter.

3.3.1.3. The MAM season and climatology for 00h00 and 12h00

It can be seen from Figure 3.11 and Figure 3.12 that the autumn season is marked by much variability between the March, April and May months. The temperature profiles shows the seasonal transitions from relatively higher temperatures in March and relatively lower temperatures in May. The mid-season month, that is April, follows the same pattern as the seasonal mean. This is also true for dewpoint and potential temperatures. There is relative humidity retreat from higher values in March to lower values in May. However, the relative humidity patterns are similar for all the months of the seasons. It is interesting to also note that the temperature lapse-rates near the surface retreat from being height in March and lower in May, which can also explain the intensifying temperature inversion between the months of March and May.

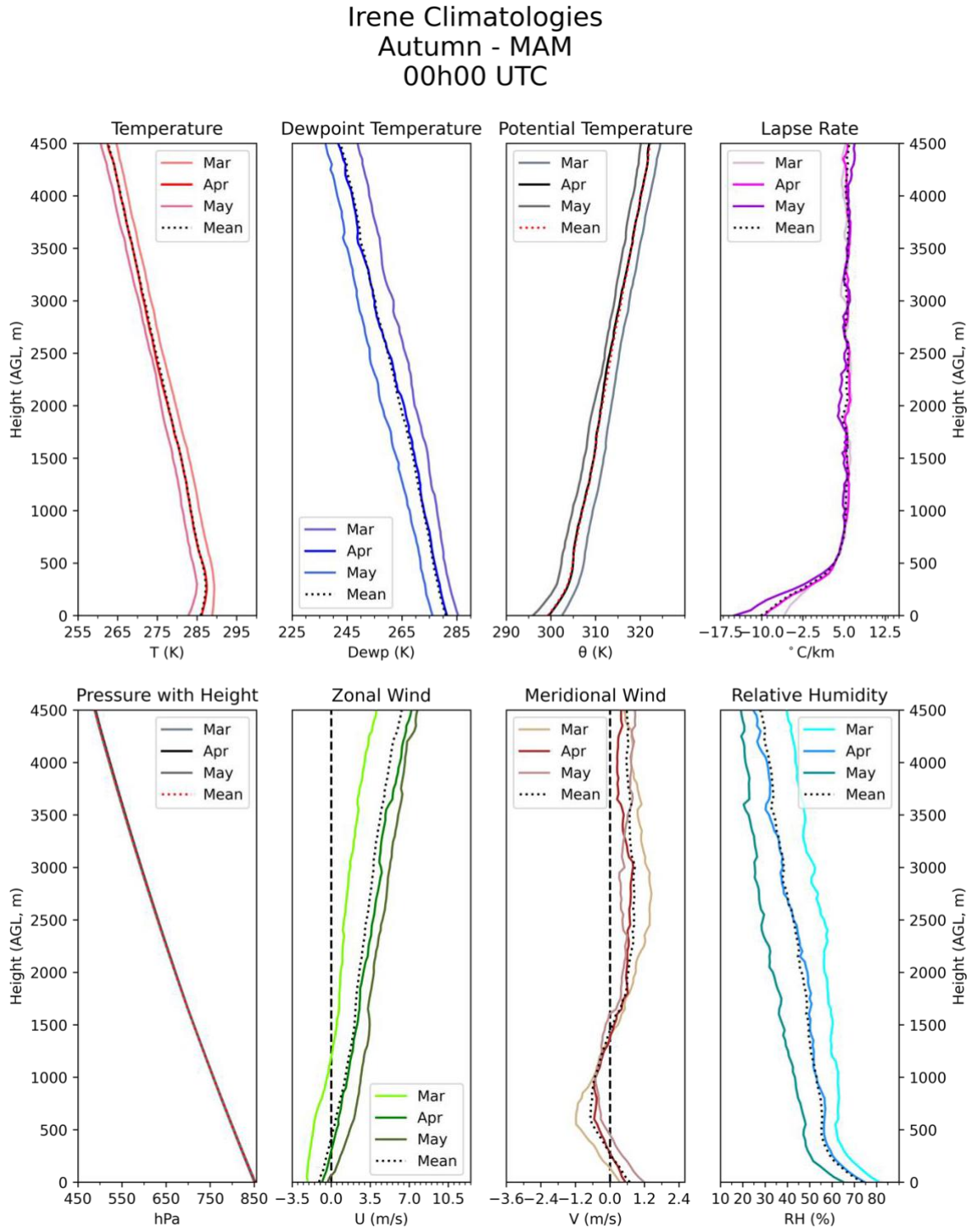

Figure 3.11: Irene radiosonde observation climatologies for the months of March, April, and May (austral autumn) at 00h00 UTC. The seasonal mean is also included for each parameter.

Although variable, the potential temperature indicates an unstable atmosphere near the surface. The pattern is also similar throughout the season, with the April pattern following the seasonal mean values. The April months also follows the seasonal mean patterns for

temperature, dewpoint temperature and relative humidity. It is interesting to note the meridional wind pattern for the month of May, which indicates variability between the surface and about 2250 m above ground-level, while the reversed S-shape patterns persist for the autumn months of April and May.

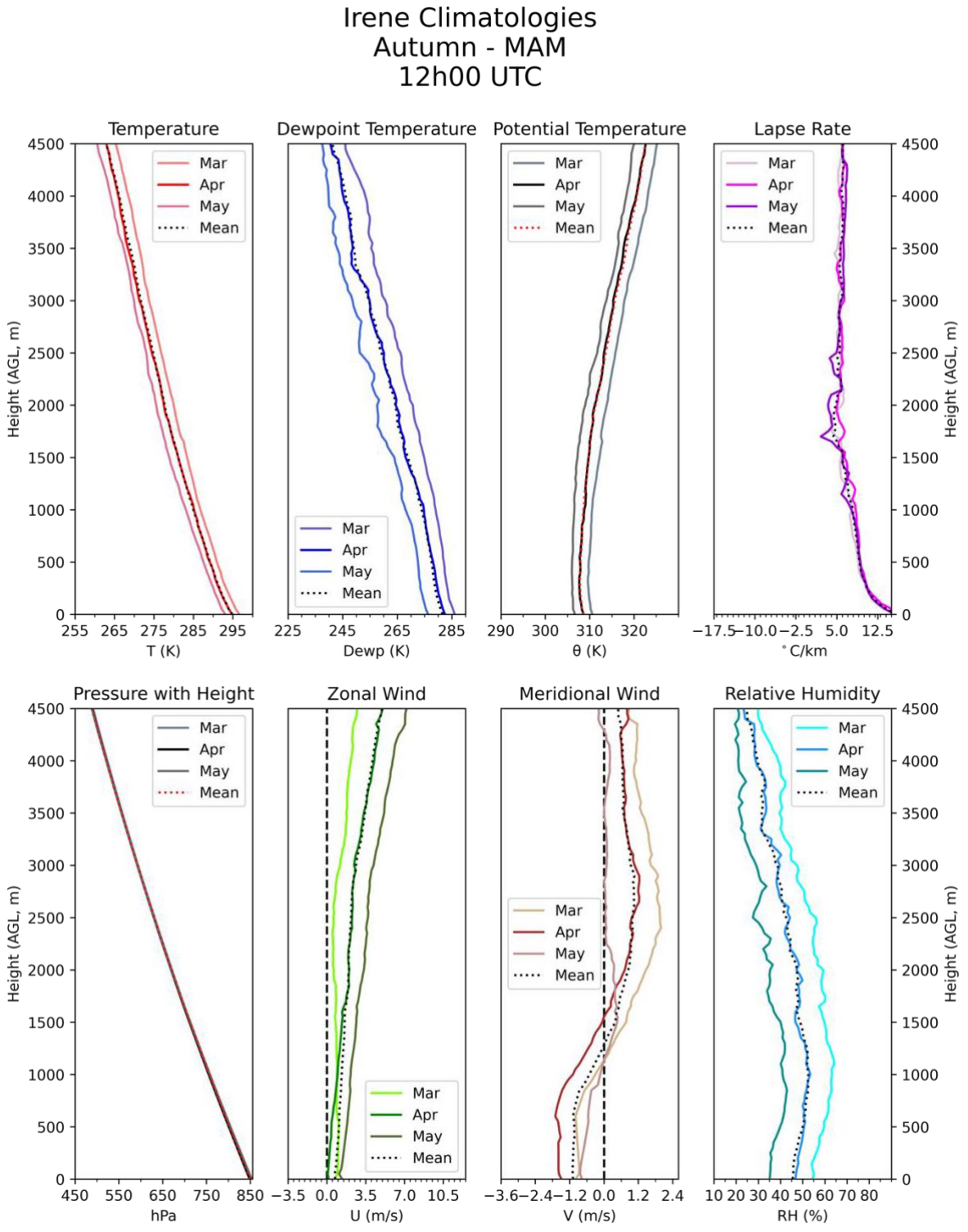

Figure 3.12: Irene radiosonde observation climatologies for the months of March, April, and May (austral autumn) at 12h00 UTC. The seasonal mean is also included for each parameter.

3.3.1.4. The JJA season and climatology for 00h00 and 12h00

The outstanding feature of the winter months of June, July and August, are the much deeper temperature inversions. The June and July inversion patterns have the same values as the seasonal mean, while August – end of winter – indicates slightly higher temperature values near the surface, albeit still with an inversion. Above 2500 m, temperature values for all three months are the same. This is interestingly also true for the potential temperature values. There is much variability in the meridional winds, and especially for the month of August. The meridional wind patterns for the winter months have also lost the reversed S-shape observed during the other seasons, while the zonal winds are more stronger and prominent than the other seasons. The relative humidity profiles also indicates less variability between the winter months compared to the variability observed during other seasons.

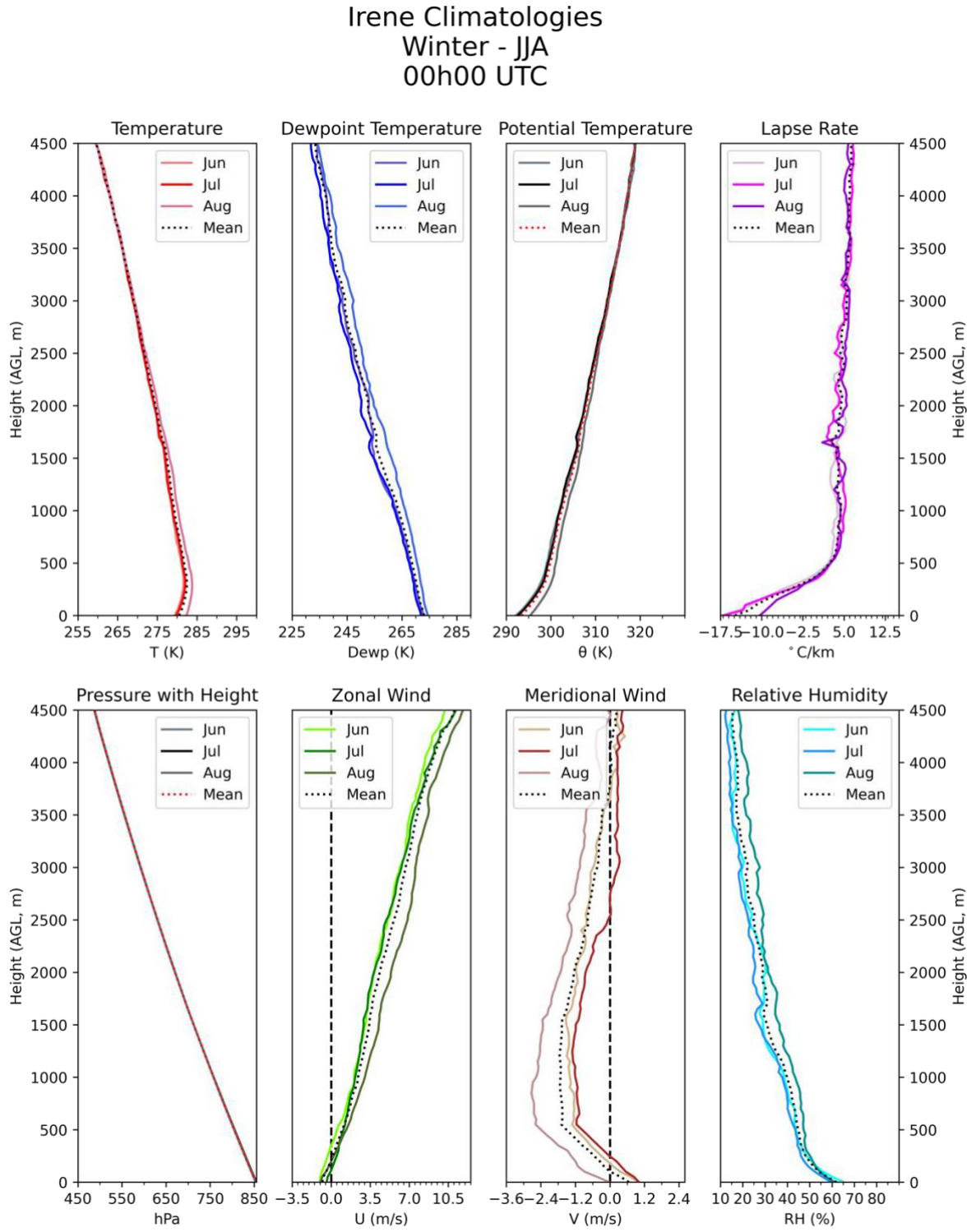

Figure 3.13: Irene radiosonde observation climatologies for the months of June, July, and August (austral winter) at 00h00 UTC. The seasonal mean is also included for each parameter.

Figure 3.14 indicates zonal wind patterns that are similar, below 1500 m, for the winter months of June, July and August. Above this level, the meridional winds are observed around the

seasonal mean which can be represented by 0 m/s, while zonal winds are dominant. This means that above 1500 m (and below 4500 m which is the upper limit of our analysis), winds tend to be westerlies during austral winter months. Temperature patterns and values for the months of June and July are similar, and also follow the mean pattern, while August indicates values that are slightly higher than the mean. It is interesting to observe that the relative humidity bulge above the surface at 12h00 is more pronounced compared to the other seasons. The relative humidity values are also slightly lower than other seasons. Interestingly, the potential temperature profiles indicates that the lower atmosphere is still unstable during winter months at 12h00 UTC.

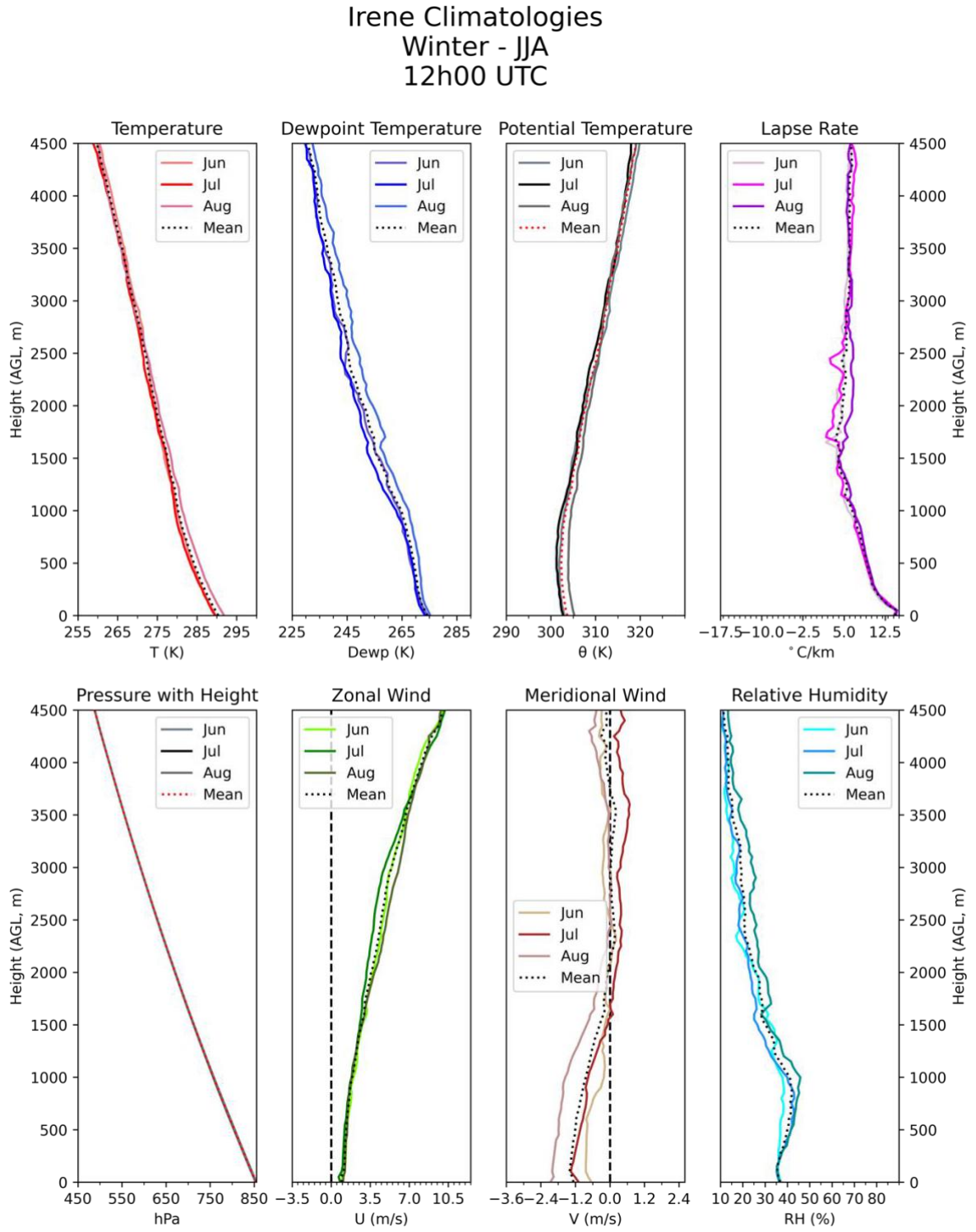

Figure 3.14: Irene radiosonde observation climatologies for the months of June, July, and August (austral winter) at 12h00 UTC. The seasonal mean is also included for each parameter.

3.3.1.5. Climatology and seasonal variability of the ABLH for 00h00 and 12h00

The monthly and seasonal ABLH for the 00h00 and 12h00 UTC sounding data were calculated according to the methods discussed in Section 3.3.5. It was found that there is monthly, and consequently, seasonal variability in the ABLH. As can be seen on Figure 3.15, surprisingly, the 00h00 UTC ABLH in Irene reach its highest during the winter months of June and July (325 m), and its lowest during the spring month of October (150 m). Figure 3.7 and Figure 3.14, respectively indicates that during the month of October (lowest ABLH value) and June/July (highest ABLH) at 00h00, there is a temperature inversion, the top of which represents the expected height of the boundary layer. Interestingly, this temperature inversion is relatively deeper during the winter months, and shallow during spring, which may explain why ABLH is highest during June/July and lowest during October.

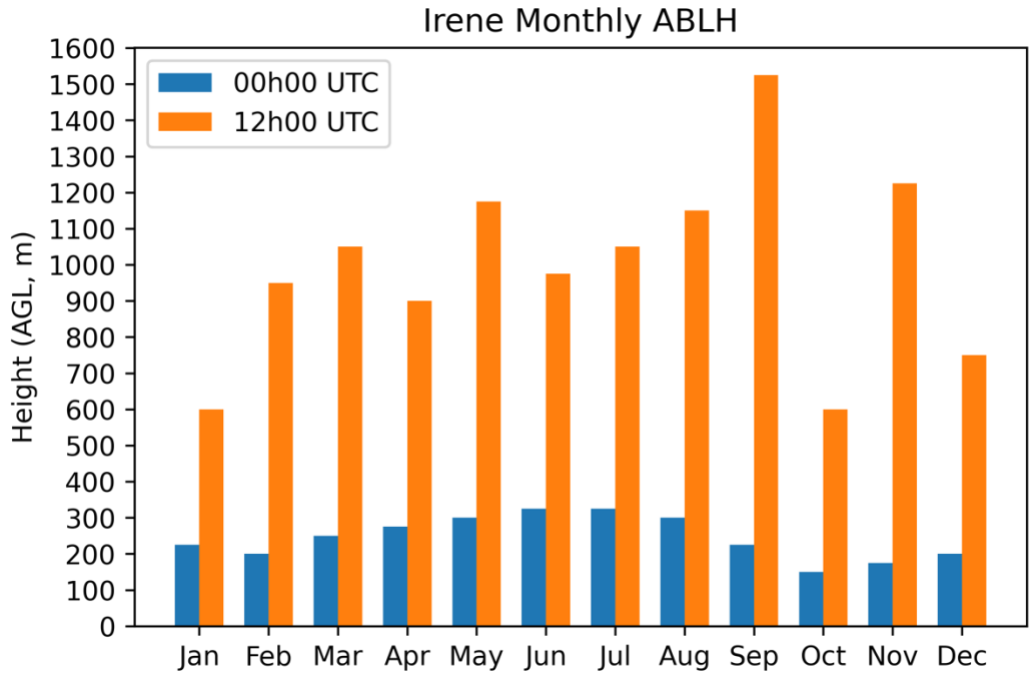

Figure 3.15: Monthly climatologies of the ABLH for 00h00 UTC (blue) and 12h00 UTC (orange) over Irene.

Contrary to the 00h00 UTC data, the 12h00 UTC analysis indicates that the spring month of September has the highest ABLH of 1525 m, while the spring month of October and the summer month of January have the lowest ABLH of 600 m. This means that October has overall lowest ABLH for both the 00h00 UTC and 12h00 UTC hours. Potential temperature for the month of September (see Figure 3.8) indicates that most of the lower troposphere is

unstable and is capped by an elevated temperature inversion. This can explain why September has the highest ABLH values at 12h00 UTC.

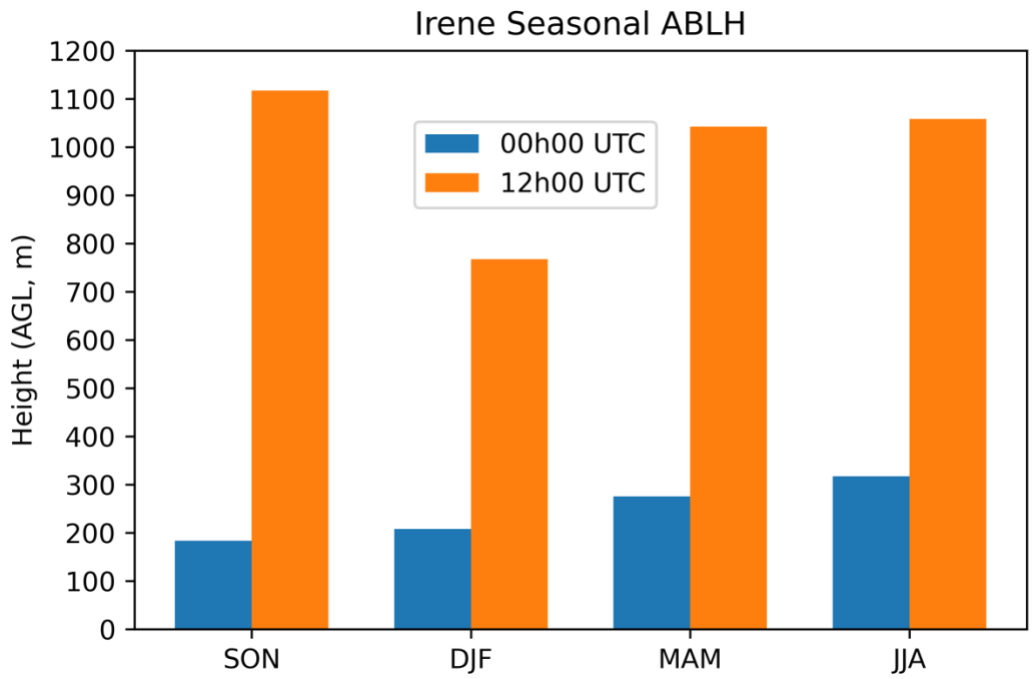

Figure 3.16: Seasonal climatologies of the ABLH for 00h00 UTC (blue) and 12h00 UTC (orange) over Irene.

Figure 3.16 indicates the seasonal ABLH means over Irene at 00h00 UTC and 12h00 UTC. Throughout the different seasons, it was found that 00h00 UTC ABLH are shallow compared to the 12h00 UTC. This was expected as 00h00 UTC represents 02h00 local Irene time. Temperature profile analysis indicates the presence of inversion at this time throughout the four seasons. This is because as the surface begins to cool at night the air near the surface cools faster than the air above, which then results in the temperature inversion. The ABLH at 00h00 UTC also persistently increases in depth from spring, and reaches its peak during winter.

The seasonal ABLH means indicates highest values in spring and lowest values in summer. The possible explanation of highest values of ABLH occurring during spring is the presence of elevated temperature inversion especially for the month of September. Also, apart from summer, the other seasons have ABLH mean values above 1000 m at 12h00 UTC. Summer has the mean value of 767 m, while spring, autumn and winter respectively have values of 1117 m, 1042 m, and 1058 m.

3.3.2. Marion Island Station

3.3.2.1. The SON season and climatology for 00h00 and 12h00

Climatological analysis shown in Figure 3.17 for the spring months of September, October and November over Marion Island at 00h00, indicates that below 2000 m there is not much variability in the potential temperature. Temperature profiles indicates that the mid-spring month of October follows the seasonal mean pattern, while September and November deviates from the mean, especially above the 2000 m height. Temperature lapse-rates follow the same pattern throughout the spring season, however, there is variability above 200 m. Interestingly, the zonal winds indicates much variability between the seasons (starting from 900 m for October and November), with relatively higher values for the month of September, and lower values for October. Below 4000 m, meridional winds seem to follow the same pattern, although variable between the three spring months. Relative humidity also follows the same pattern during spring, while pressure values are the same throughout the seasons.

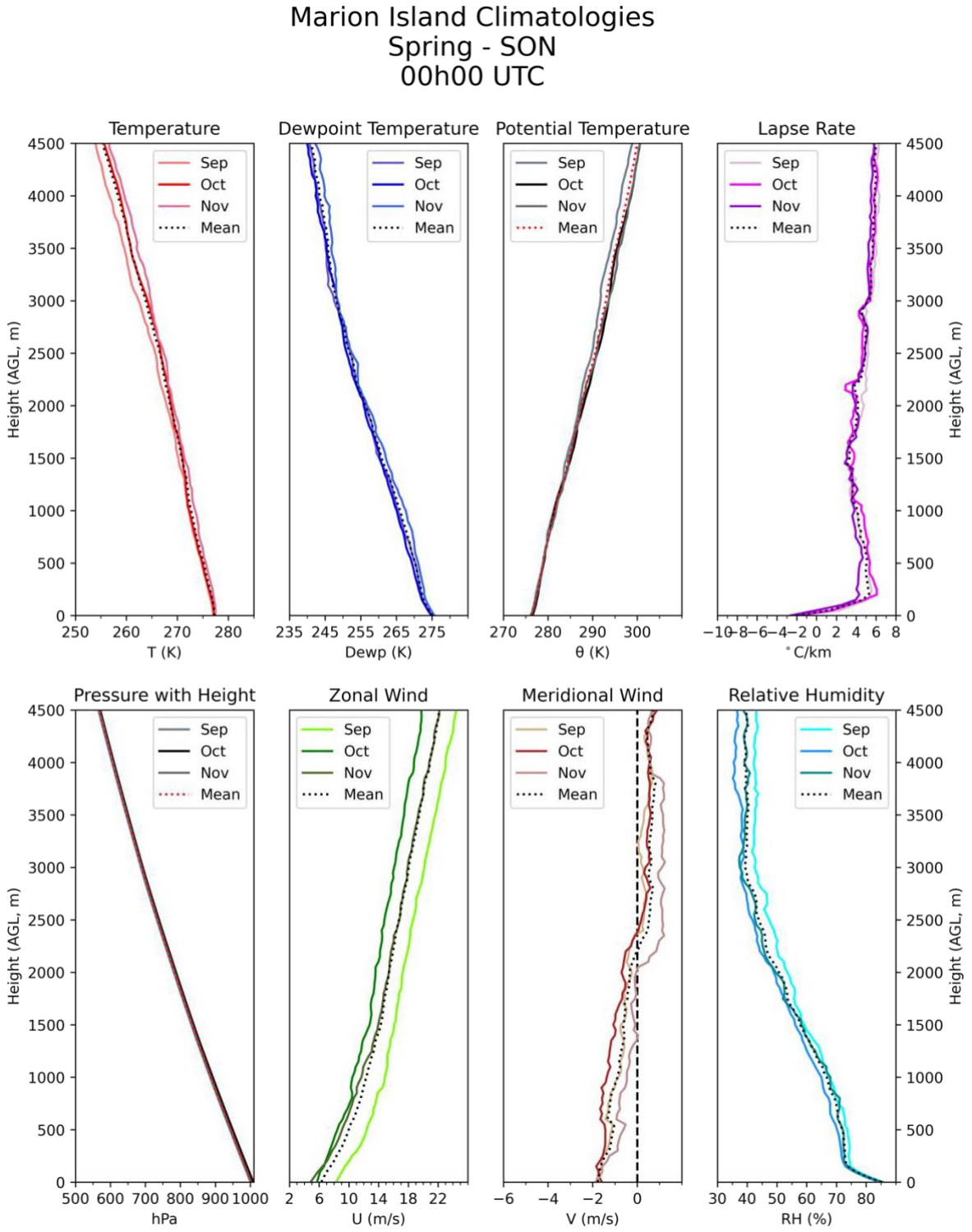

Figure 3.17: Marion Island radiosonde observation climatologies for the months of September, October, and November (austral spring) at 00h00 UTC. The seasonal mean is also included for each parameter.

Figure 3.18 shows substantial variability in temperature, potential temperature, zonal and meridional winds throughout the spring season at 12h00 UTC. Temperature, potential temperature and meridional wind values increase from their seasonal minimum in September to their spring maximum in November, while the month of October follows the seasonal mean pattern. Relative humidity profiles shows a bulge above the surface. Potential temperatures are almost constant between the surface and 250 m, which implies that the near-surface atmosphere over Marion Island at 12h00 UTC is near-neutrally stratified.

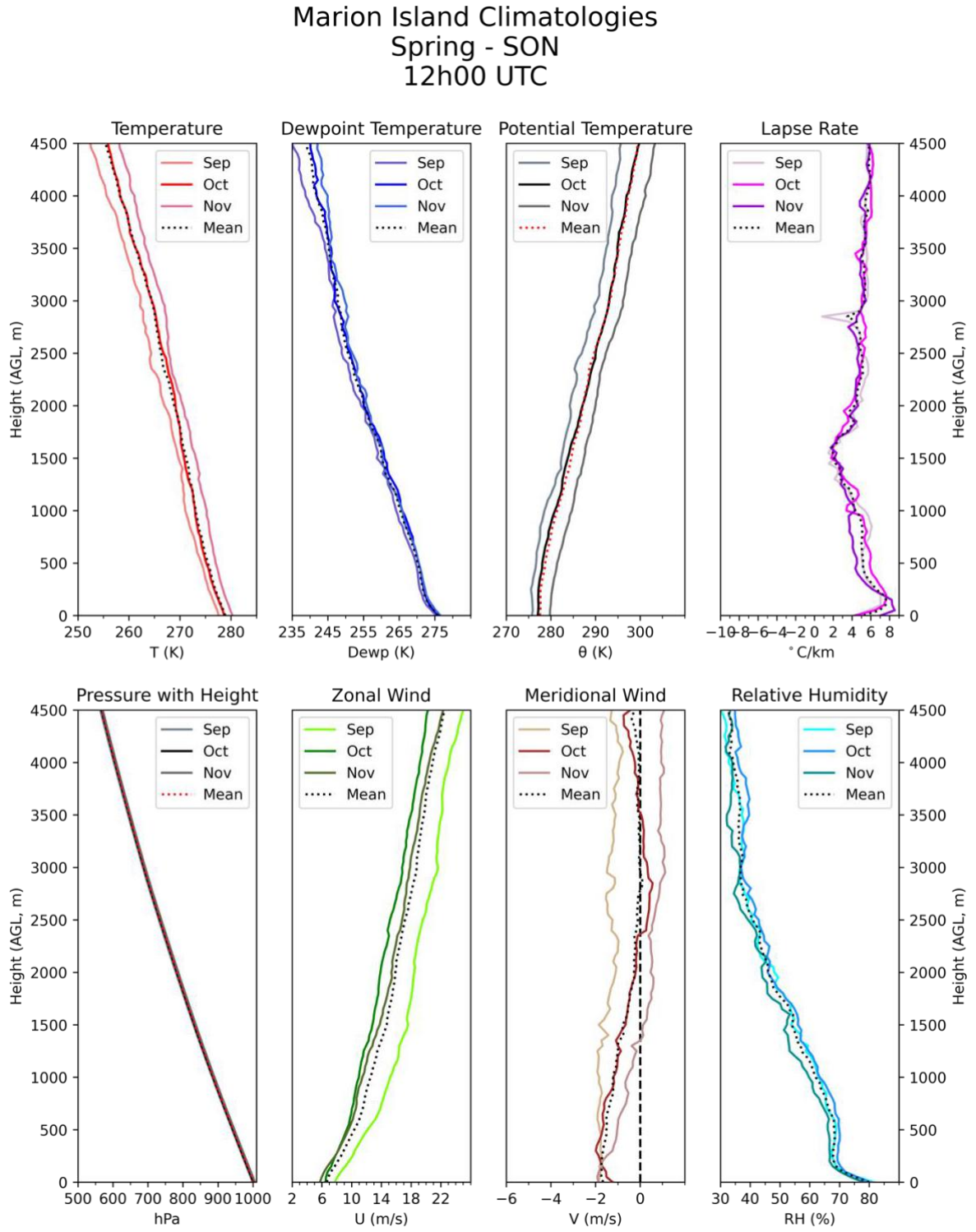

Figure 3.18: Marion Island radiosonde observation climatologies for the months of September, October, and November (austral spring) at 12h00 UTC. The seasonal mean is also included for each parameter.

3.3.2.2. The DJF season and climatology for 00h00 and 12h00

The temperature values for December and January at 00h00 UTC are almost similar between the surface and the 1500 m height, from which they start to vary. February temperature and potential temperature values are relatively higher than for December and January. Zonal wind patterns follow the classic mid-latitudinal logarithmic wind descriptions, with values being lowest near the surface and highest at the top of the lower-atmosphere. Temperature lapse-rate profiles indicate that for the months of January and February, there is a drastic decrease in the environmental lapse rates between the heights of 1300 m and 1800 m. Relative humidity patterns are similar throughout the season, while meridional wind patterns vary between the three summer months.

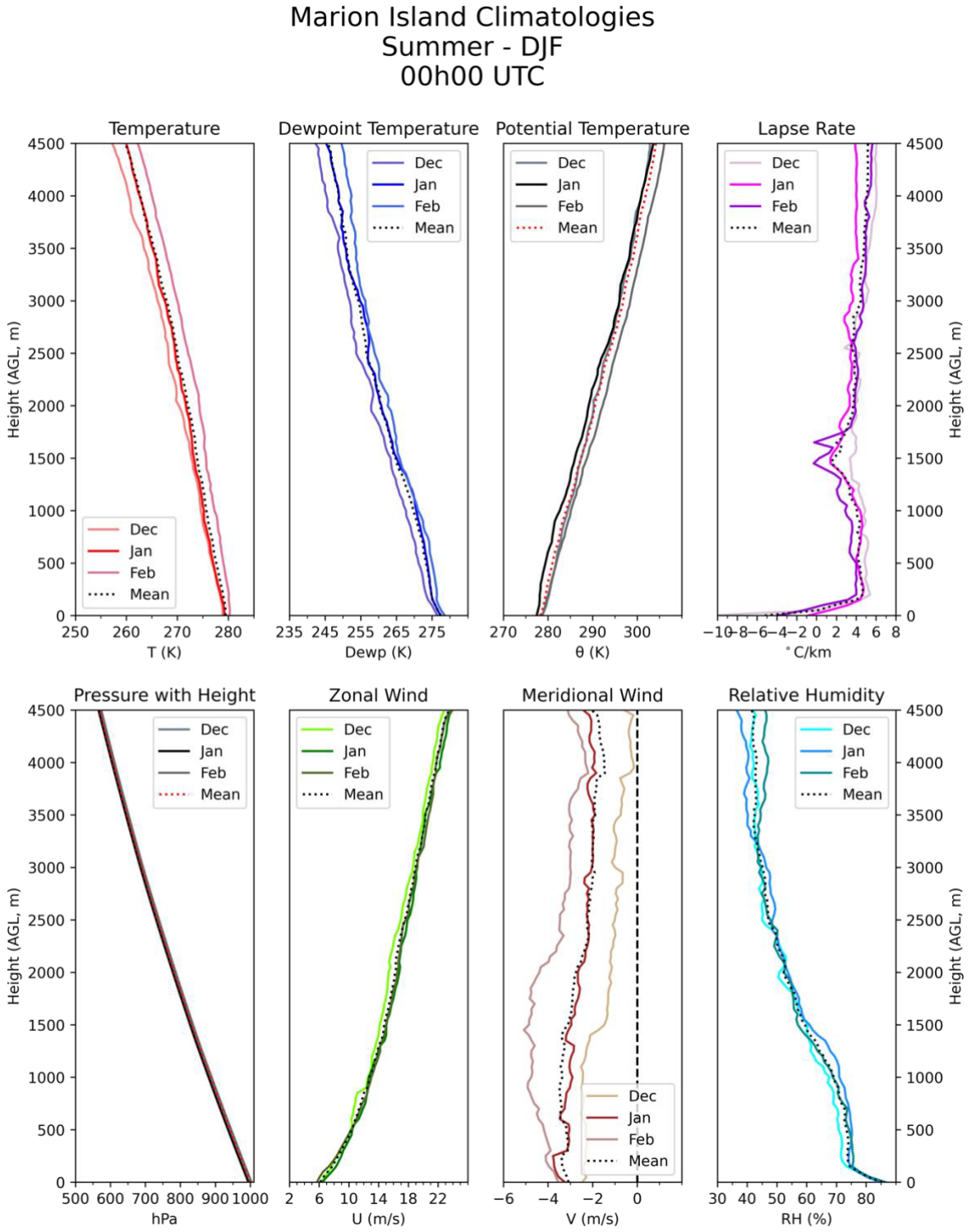

Figure 3.19: Marion Island radiosonde observation climatologies for the months of December, January, and February (austral summer) at 00h00 UTC. The seasonal mean is also included for each parameter.

Potential temperature profiles for Marion Island at 12h00 UTC during the summer months, as shown in Figure 3.20, depicts a near-surface atmosphere that is in near-neutral state. This is the same as observed with the spring months. This means that the near-surface atmosphere over Marion Island is neutrally stratified for both the spring and summer seasons. Relative humidity values below 1500 m are almost similar for all the three summer months. Meridional winds are almost similar in their vertical pattern, although their values vary throughout the season, with February having relative higher values and December having relatively lower values. The January relative humidity values are almost similar to the seasonal mean values.

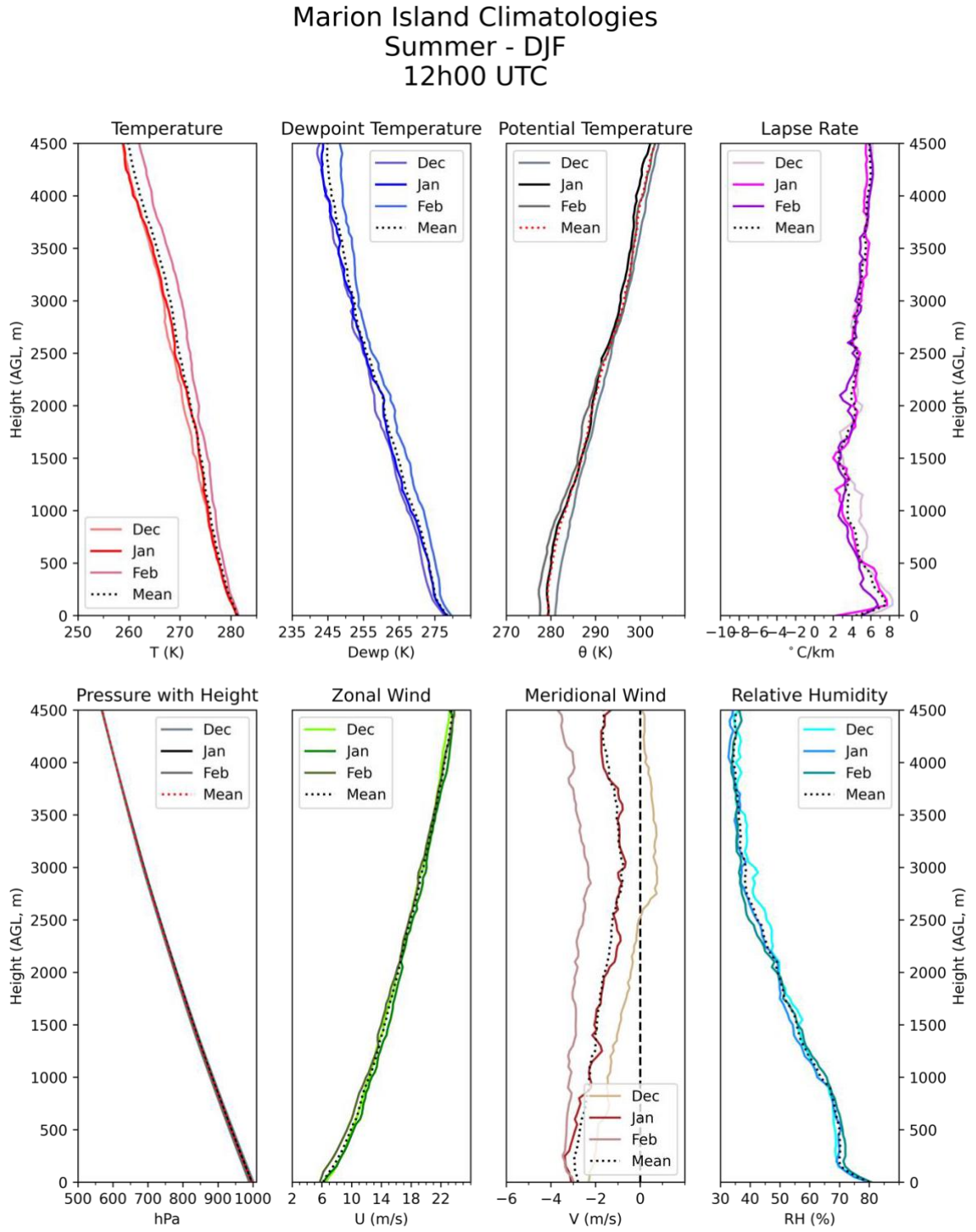

Figure 3.20: Marion Island radiosonde observation climatologies for the months of December, January, and February (austral summer) at 12h00 UTC. The seasonal mean is also included for each parameter.

3.3.2.3. The MAM season and climatology for 00h00 and 12h00

Figure 3.21 and Figure 3.22 shows that the autumn months of March, April, and May are characterised by a systematic decrease in temperature, dewpoint temperature and potential temperature values. The beginning of autumn in March is marked by relatively higher values, while the end of it in May is marked by relatively lower values. The mid-autumn month of April has a pattern and values that are similar to the seasonal means. The 00h00 UTC profiles in Figure 3.22 indicates that the temperature lapse-rates follow the same pattern below 750 m, while above this level there is slight deviation especially for March. Relative humidity profiles indicates a similar vertical pattern throughout the season, with a bulge observed above the surface. March has zonal wind patterns that follow the seasonal mean, while the month of May has relative higher values compared respectively to April and March. The meridional wind patterns are similar for the months of March and May, although their values are variable.

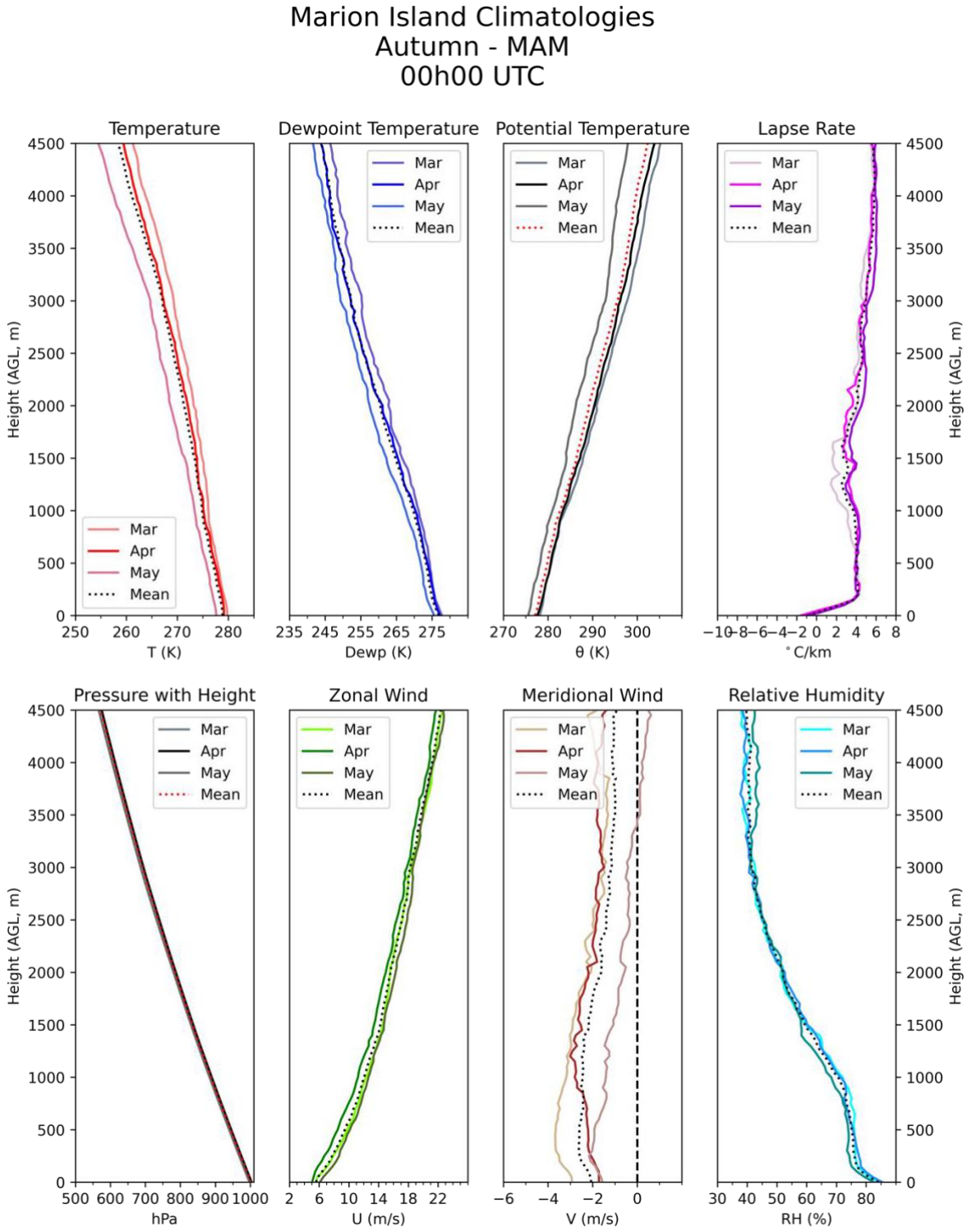

Figure 3.21: Marion Island radiosonde observation climatologies for the months of March, April, and May (austral autumn) at 00h00 UTC. The seasonal mean is also included for each parameter.

The 12h00 UTC meteorological profiles shown in Figure 3.22 indicates that the relative humidity values are almost similar below 3000m, while they vary above this level. Temperature lapse-rate values are also slightly variable throughout the season and range between 4 °C/km and 6.5 °C/km. The month of March has relatively higher values compare to May and April, while April also has values similar to the seasonal mean. Figure 3.22 also shows that dewpoint temperature patterns are different for all the three months, while temperature has similar patterns although values are varied with May having slightly lower temperature values compared to April and May. The zonal wind also has varied values for all the three months with relatively lower values observed for April. The meridional winds vary throughout the season.

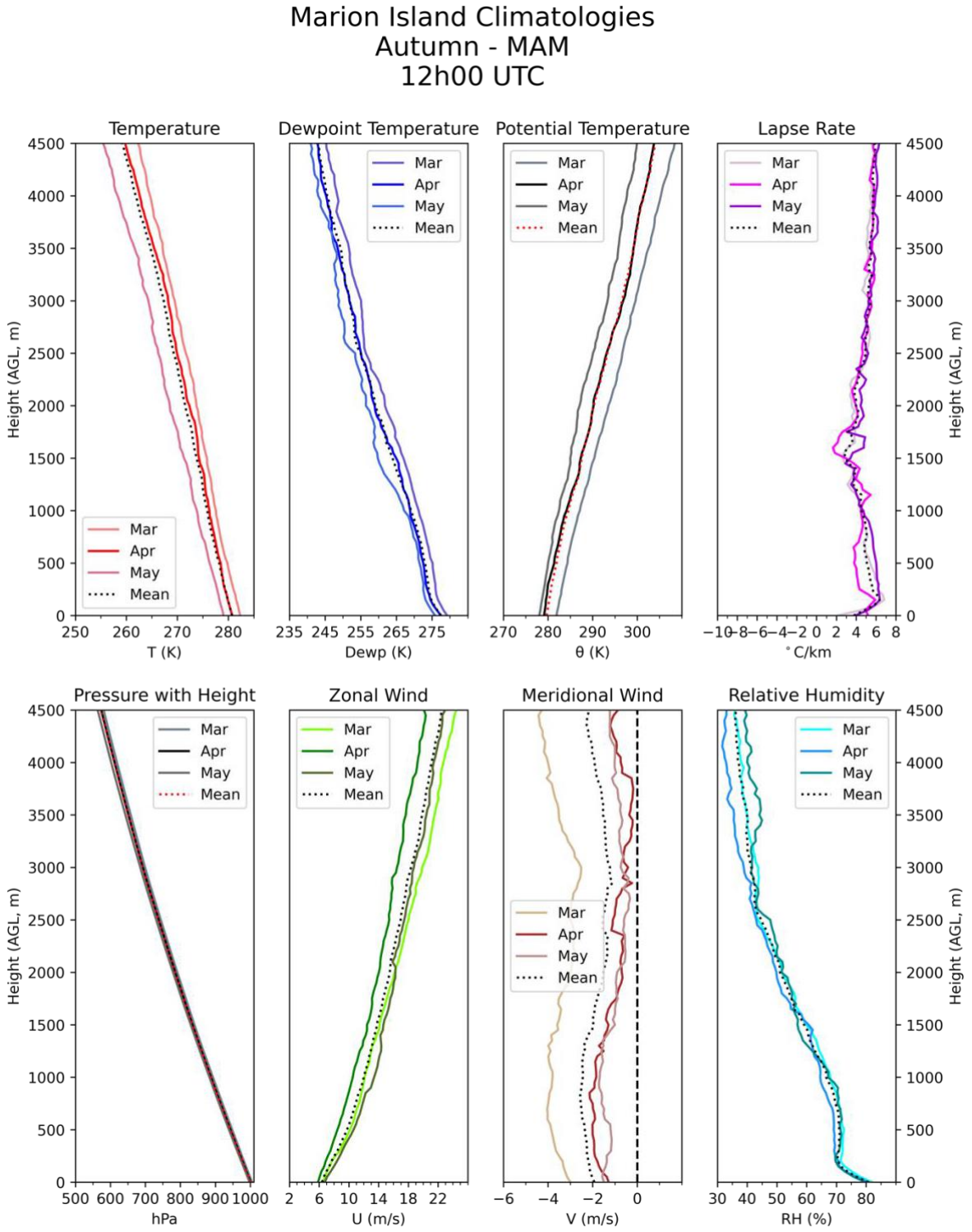

Figure 3.22: Marion Island radiosonde observation climatologies for the months of March, April, and May (austral autumn) at 12h00 UTC. The seasonal mean is also included for each parameter.

3.3.2.4. The JJA season and climatology for 00h00 and 12h00

Figure 3.23 indicates that the winter months of June, July and August have a temperature inversion near the surface. This temperature inversion is not as deep compared to those observed at the Irene station, for the same time and season. This may be described as a surface-based inversion, which also explains why the ABLH (see Figure 3.25) is shallow throughout the winter season. The potential temperature profiles indicate that June has relatively lower values compared August and July. It is interesting to note that the mid-season month of July has relatively higher values compared to June and August, while the month of August has the same values as – and follows the same pattern as – the seasonal climatology. The zonal winds follow the logarithmic pattern as for all other months.

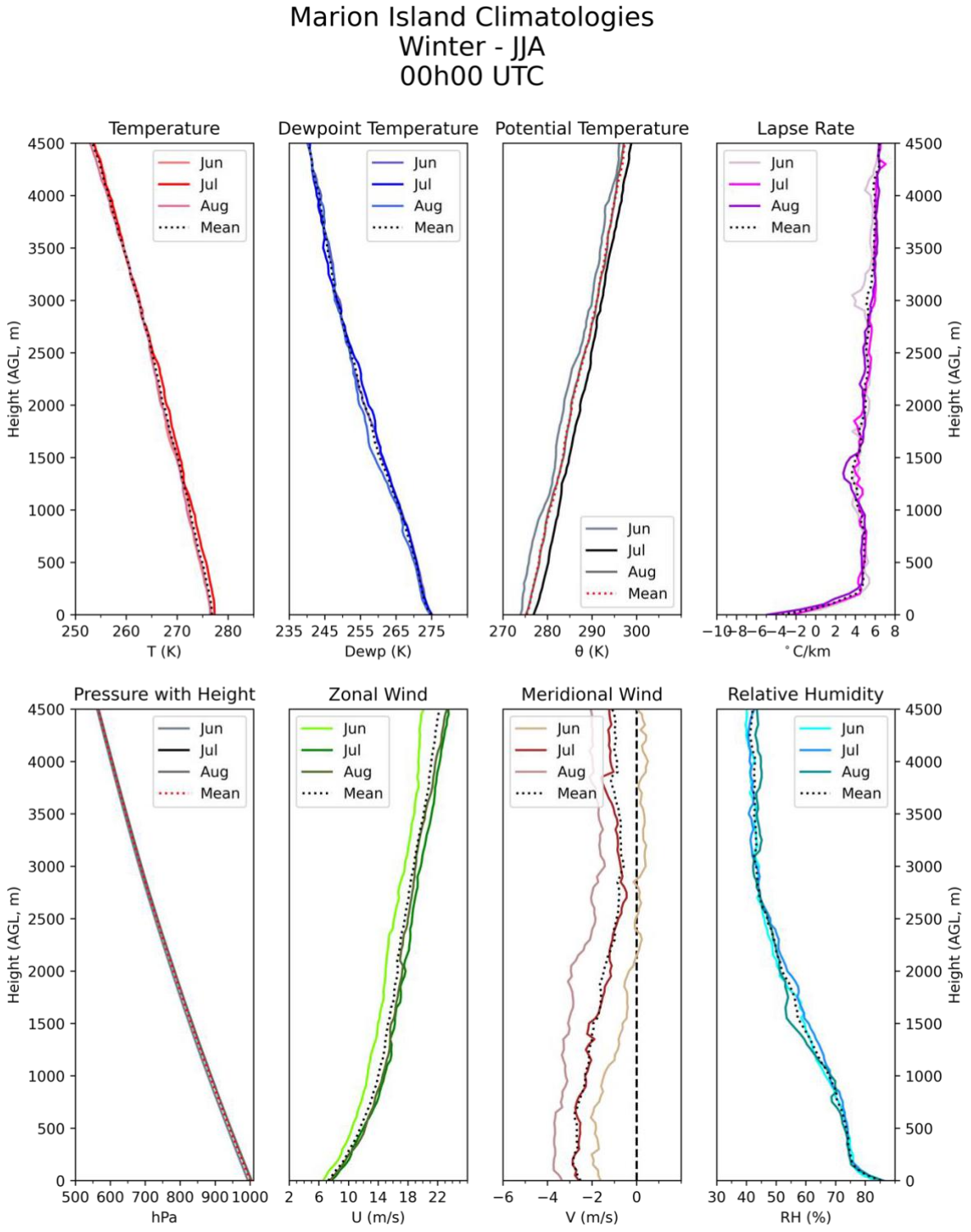

Figure 3.23: Marion Island radiosonde observation climatologies for the months of June, July, and August (austral winter) at 00h00 UTC. The seasonal mean is also included for each parameter.

Figure 3.24 depicts meteorological parameter profiles over Marion Island during the winter months of June, July and August at 12h00 UTC. The potential temperature plots indicate that the near-surface atmosphere is in a state of near-neutral stability, with this especially observed during the month of August. Temperature and dewpoint temperature profiles follow the same pattern throughout the winter season, while meridional wind profiles indicate much variability especially above the 3000 m level. Temperature lapse-rates follow the same pattern and values ranging between 2 °C/km and 6.5 °C/km above the surface. Relative humidity values and patterns are almost similar for all the three winter months except above the 3000 m level.

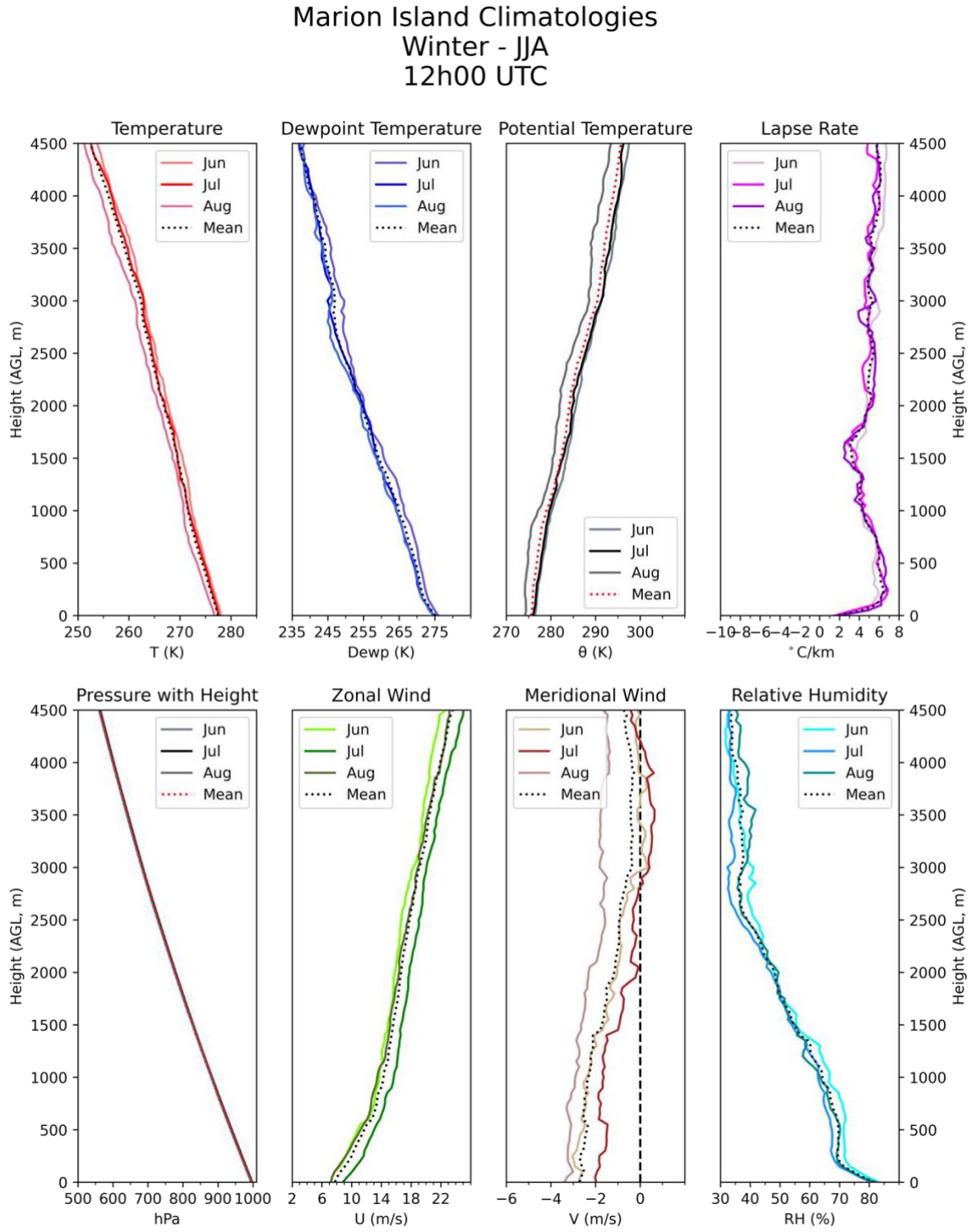

Figure 3.24: Marion Island radiosonde observation climatologies for the months of June, July, and August (austral winter) at 12h00 UTC. The seasonal mean is also included for each parameter.

3.3.2.5. Climatology and seasonal variability of the ABLH for 00h00 and 12h00

Stability analysis indicates that the lower atmosphere over Marion Island at 12h00 UTC is constantly in a near-neutral state. This result in higher ABLH values at 12h00 UTC compared to the Irene and Syowa stations. It is interesting to note that although, as depicted in Figure 3.25, the 00h00 UTC ABLH values are higher throughout the year, they are extremely low during the winter months of June, July and August, which has surface-based temperature inversion. The winter month of June has the lowest ABLH values for both 00h00 UTC (50 m) and 12h00 UTC (1150 m). The variability between the 00h00 UTC and 12h00 UTC ABLH is minimal during the summer months of December, January and February, including the spring months of September and October. This variability is pronounced during the winter months of July and August, including the months of May and November.

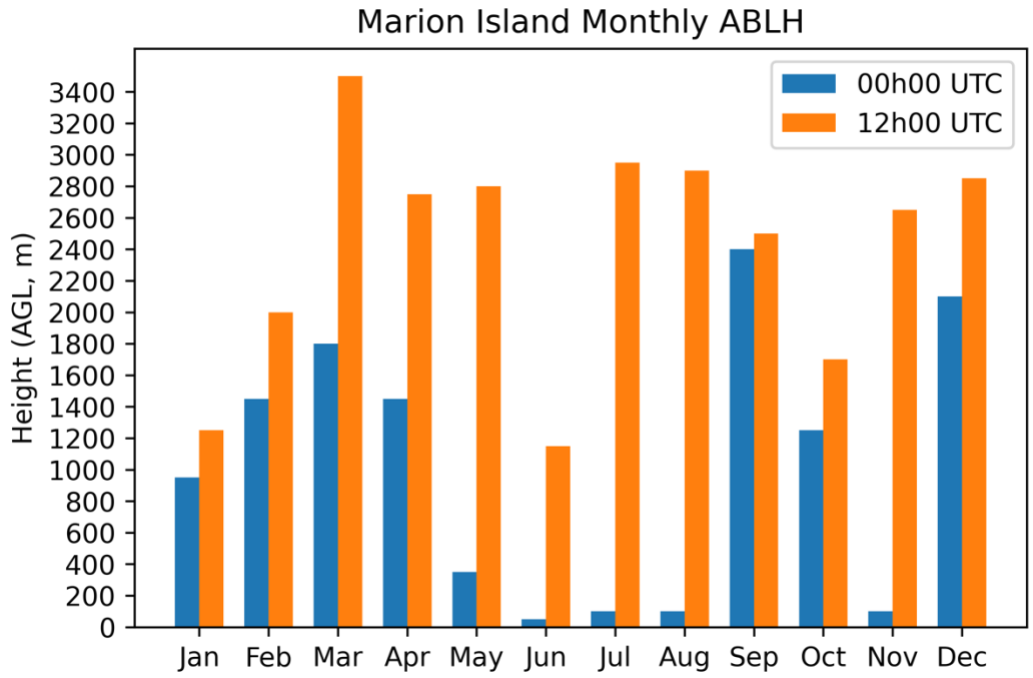

Figure 3.25: Monthly climatologies of the ABLH for 00h00 UTC (blue) and 12h00 UTC (orange) over Marion Island.

Figure 3.26 shows that the seasonal ABLH at 00h00 UTC ranges between 1200 m and 1500 m during spring, summer and autumn, with the months of spring and autumn respectively indicating values that are almost similar at 1200 m and 1250 m, while the summer season has the highest mean value of 1500 m. Out of the four seasons at 00h00 UTC, winter has the lowest mean ABLH value of 83 m. This is due to the presence of surface-based temperature inversion during the three winter months of June, July and August. The seasonal values at 12h00 also indicates that the autumn months of March, April and May, have the highest mean ABLH value of 3017 m, while the summer months of December, January, and February have the lowest mean ABLH value of 2033 m.

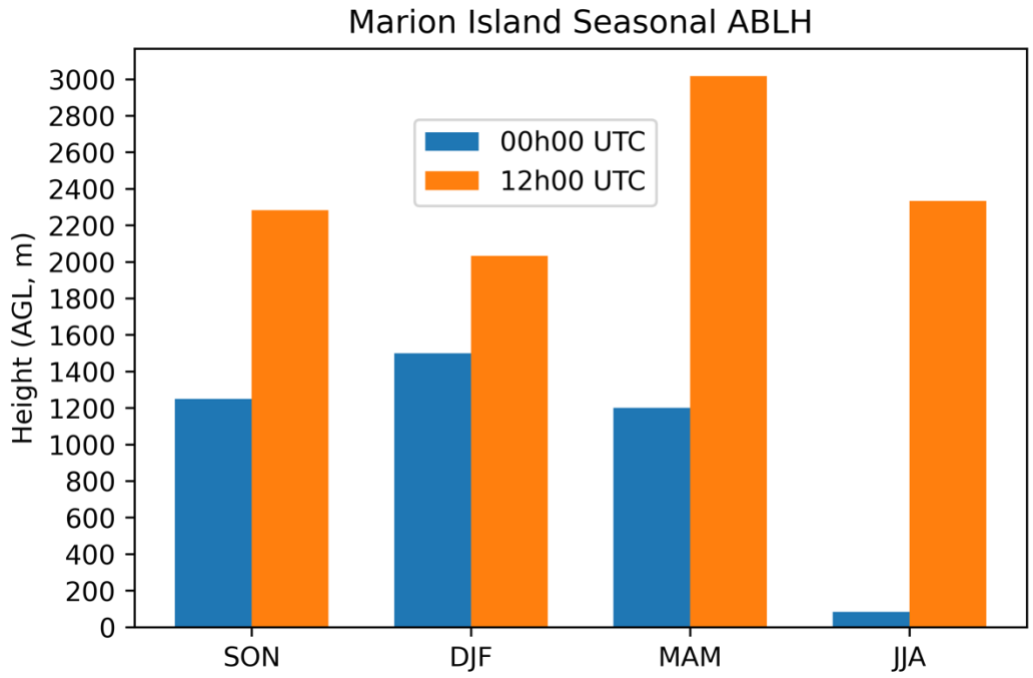

Figure 3.26: Seasonal climatologies of the ABLH for 00h00 UTC (blue) and 12h00 UTC (orange) over Marion Island.

3.3.3. Syowa Station

3.3.3.1. The SON season and climatology for 00h00 and 12h00

Figure 3.27 indicates that there is variability between the three spring months of September, October and November at both 00h00 UTC and 12h00 UTC (see Figure 3.27 and Figure 3.28). This is especially observed for temperature, dewpoint temperature, and potential temperature. Temperature inversion is observed for all the three months at 00h00 UTC, while it is only observed for September at 12h00 UTC. It is interesting to note that relative humidity indicates a bulge above the surface for both 00h00 UTC and 12h00 UTC.

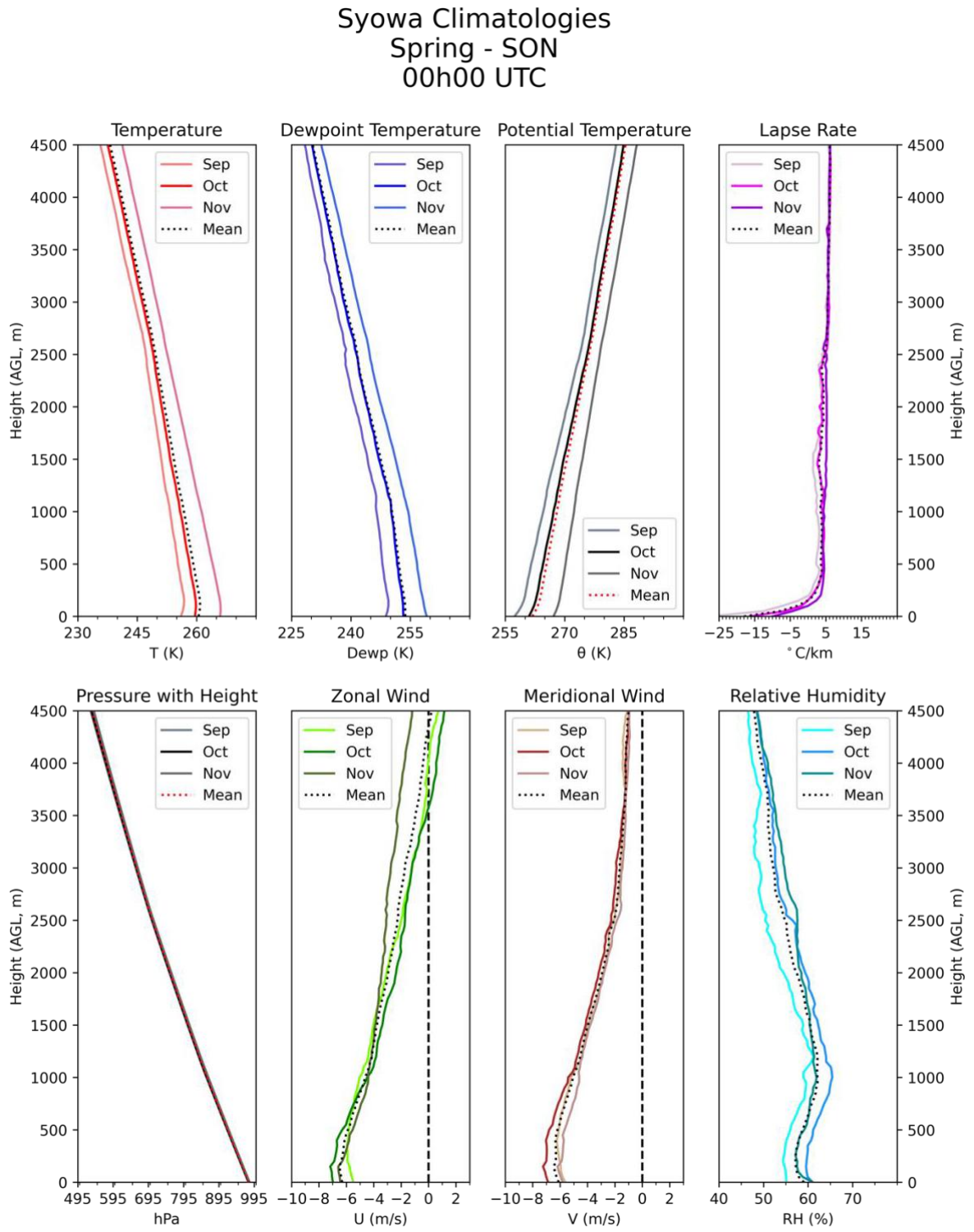

Figure 3.27: Syowa radiosonde observation climatologies for the months of September, October, and November (austral spring) at 00h00 UTC. The seasonal mean is also included for each parameter.

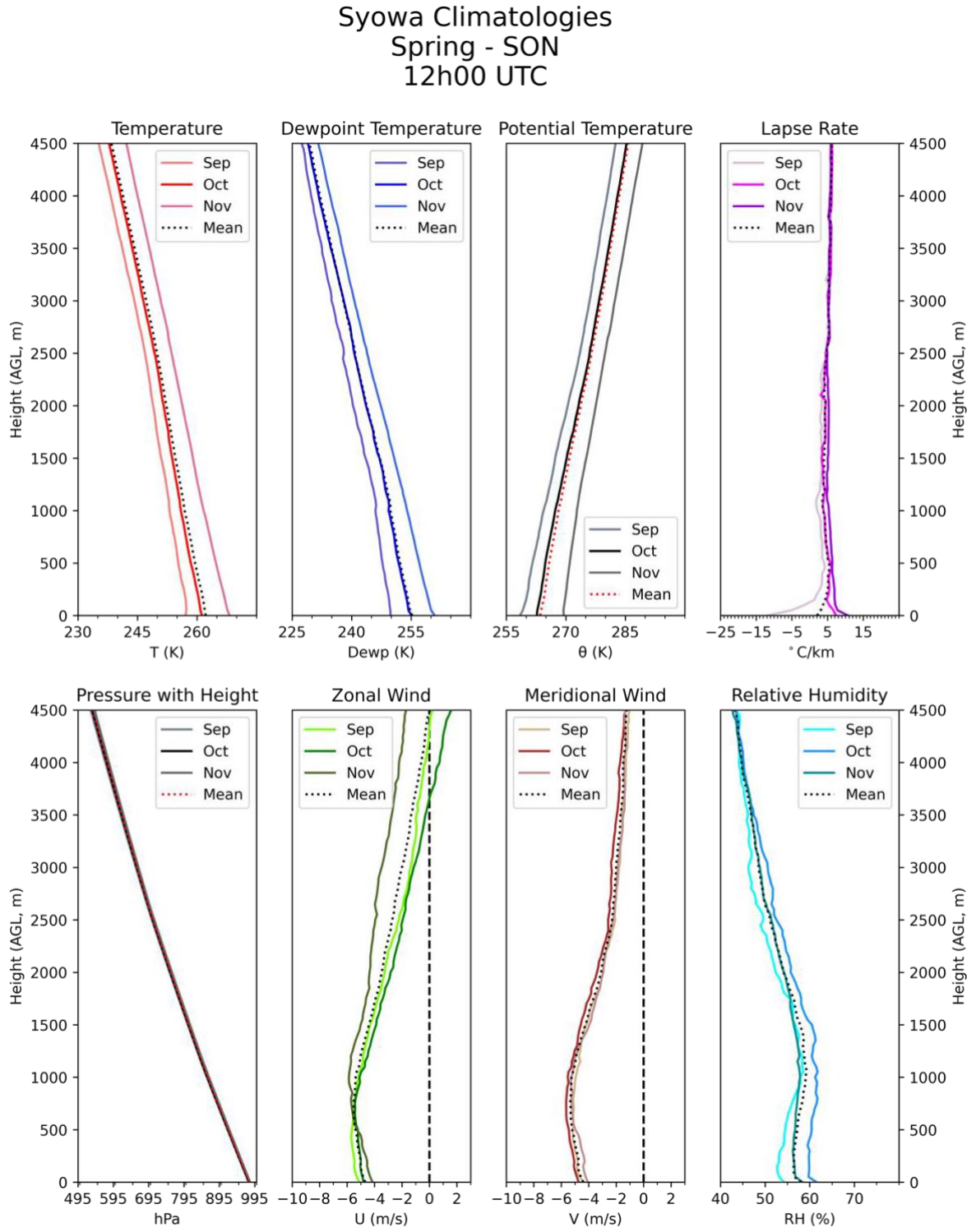

Figure 3.28: Syowa radiosonde observation climatologies for the months of September, October, and November (austral spring) at 12h00 UTC. The seasonal mean is also included for each parameter.

3.3.3.2. The DJF season and climatology for 00h00 and 12h00

It is interesting to note that, unlike during spring, the summer months of December, January, and February, indicates little to no variability at 00h00 UTC and 12h00 UTC for temperature, dewpoint temperature, potential temperature, temperature lapse-rate and pressure. For meridional wind, variability is only observed near the surface below 1500 m.

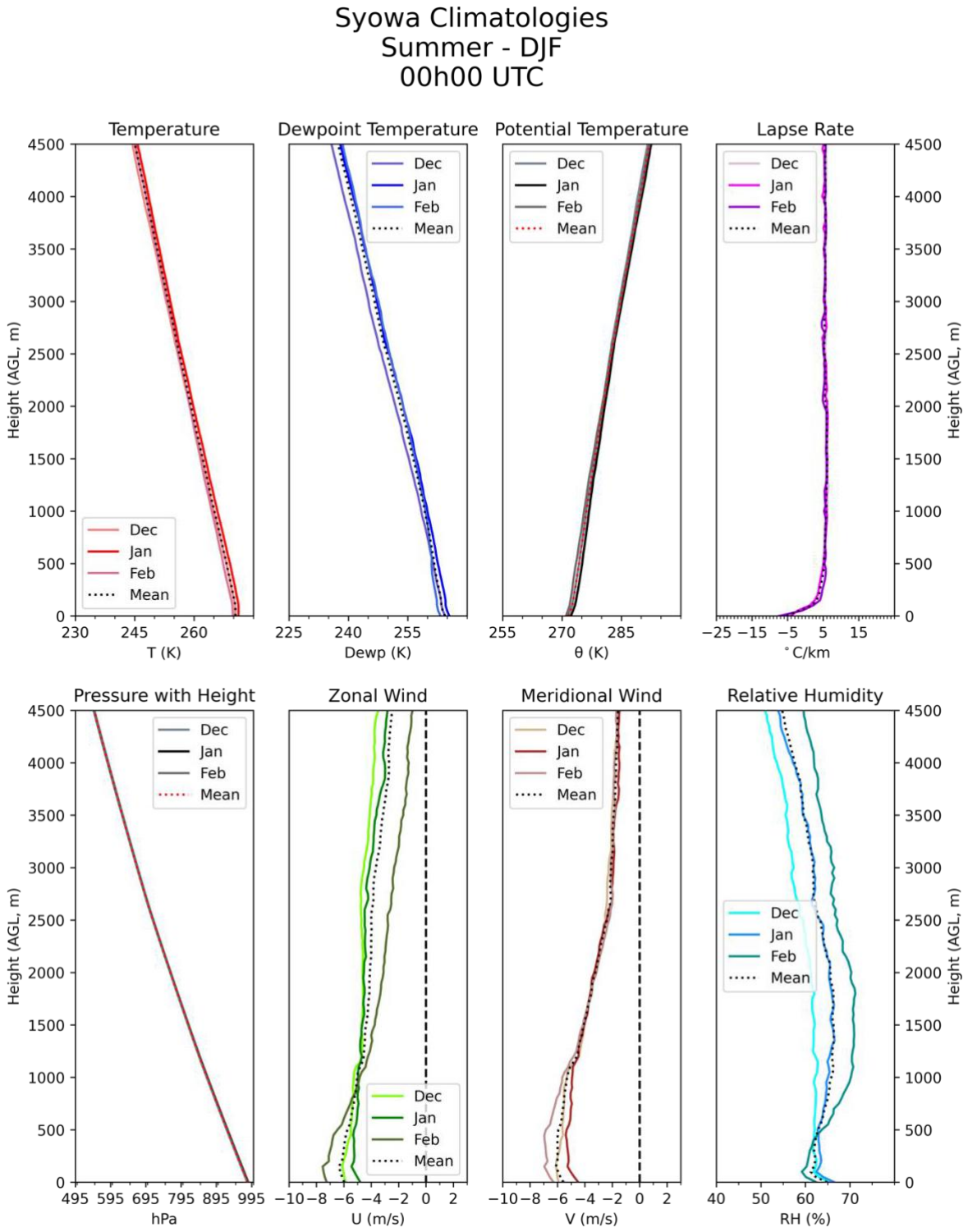

Figure 3.28: Syowa radiosonde observation climatologies for the months of December, January, and February (austral summer) at 00h00 UTC. The seasonal mean is also included for each parameter.

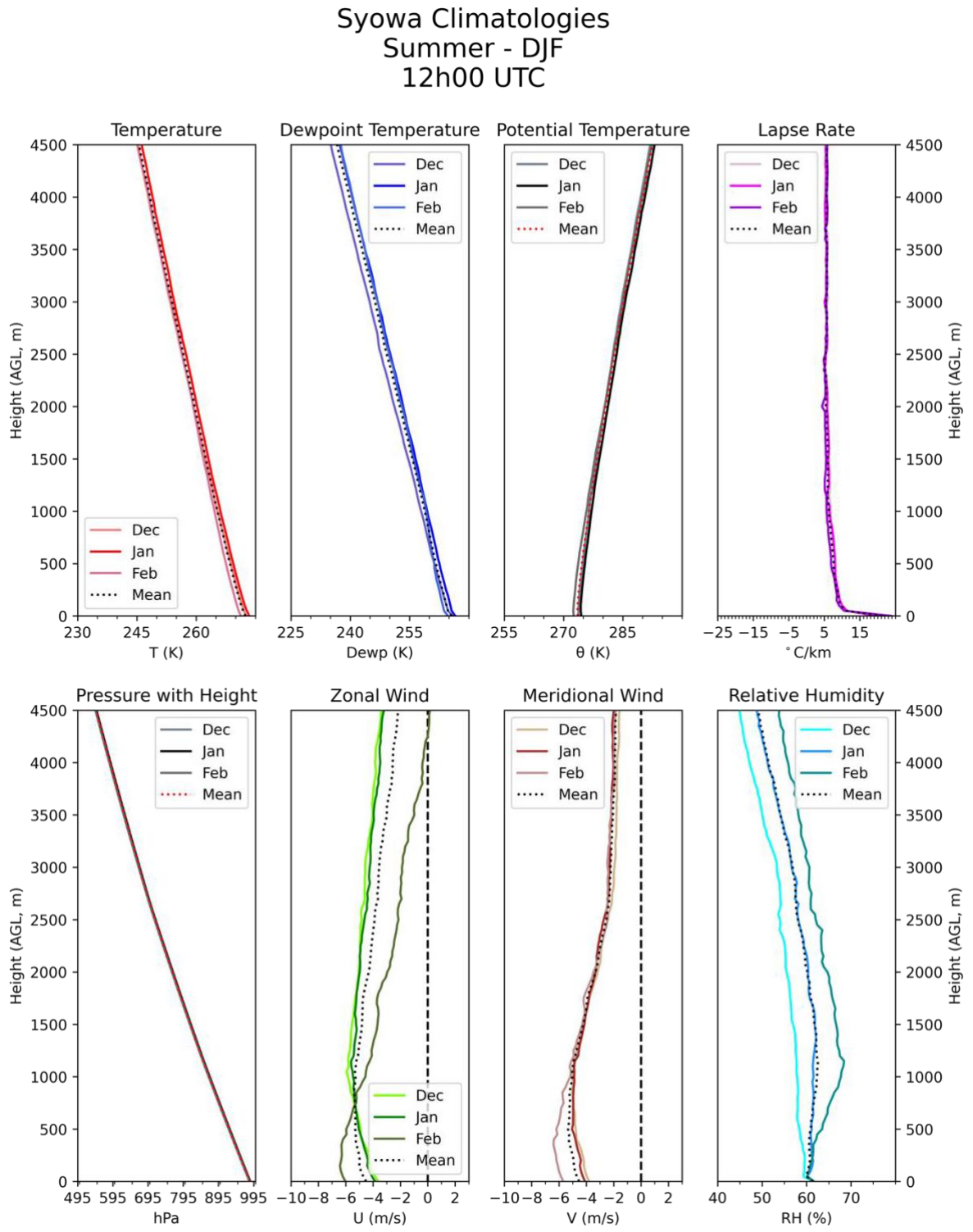

Figure 3.29: Syowa radiosonde observation climatologies for the months of December, January, and February (austral summer) at 12h00 UTC. The seasonal mean is also included for each parameter.

3.3.3.3. The MAM season and climatology for 00h00 and 12h00

As with the spring season, the autumn months of March, April, and May show variability for temperature, dewpoint temperature, potential temperature, and relative humidity for both 00h00 UTC and 12h00 UTC (see Figure 3.30 and Figure 3.31). Temperature lapse-rate and temperature indicates values and patterns that are almost similar for the three months. A relative humidity bulge is observed above the surface for both 00h00 UTC and 12h00 UTC.

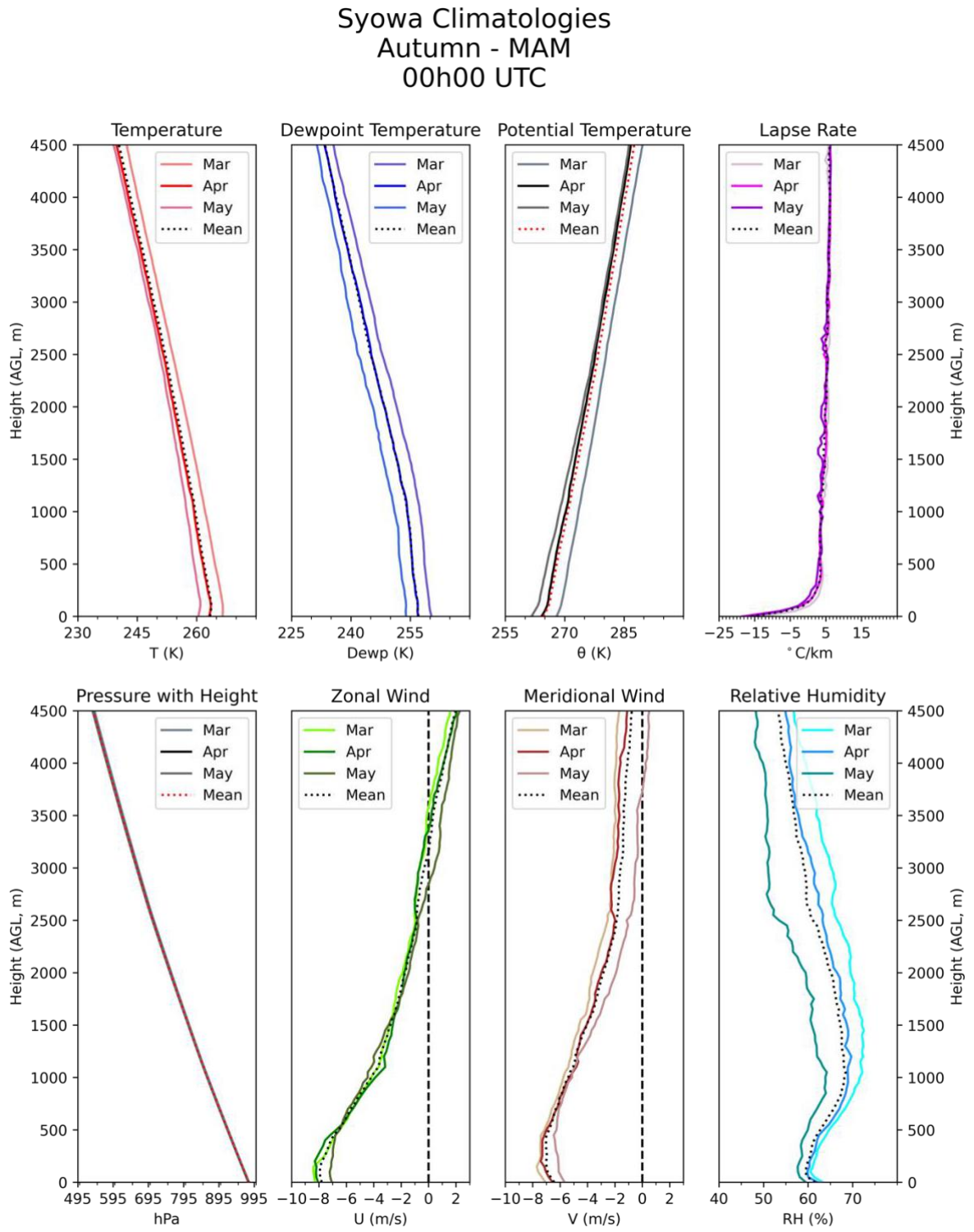

Figure 3.30: Syowa radiosonde observation climatologies for the months of March, April, and May (austral autumn) at 00h00 UTC. The seasonal mean is also included for each parameter.

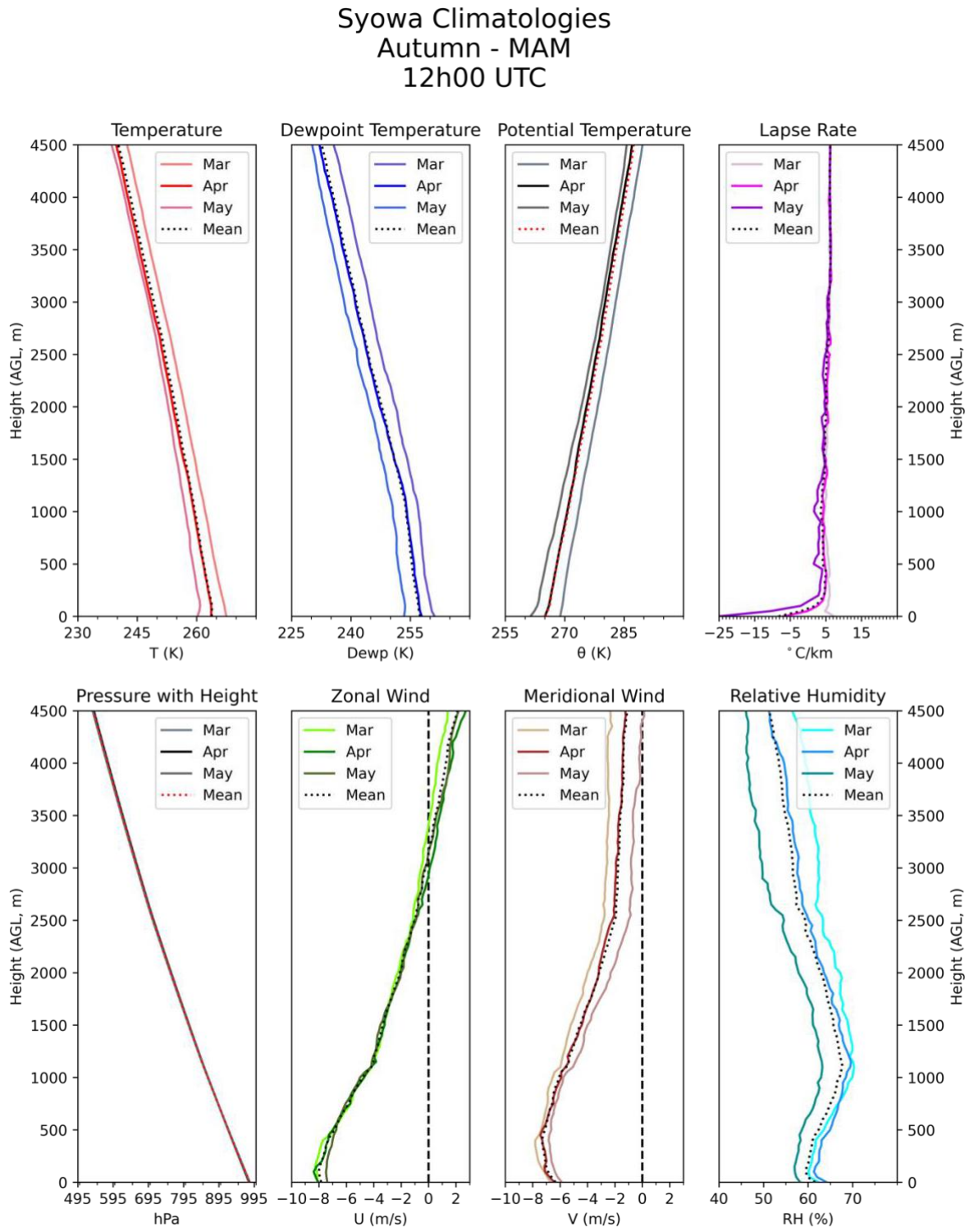

Figure 3.31: Syowa radiosonde observation climatologies for the months of March, April, and May (austral autumn) at 12h00 UTC. The seasonal mean is also included for each parameter.

3.3.3.4. The JJA season and climatology for 00h00 and 12h00

The winter months of June, July, and August, for both 00h00 UTC and 12h00 UTC (see Figure 3.32 and Figure 3.33), indicates little to no variability for temperature, dewpoint temperature, potential temperature, temperature lapse-rate, and pressure. Similar patterns and little variability are observed for zonal wind, meridional wind and relative humidity.

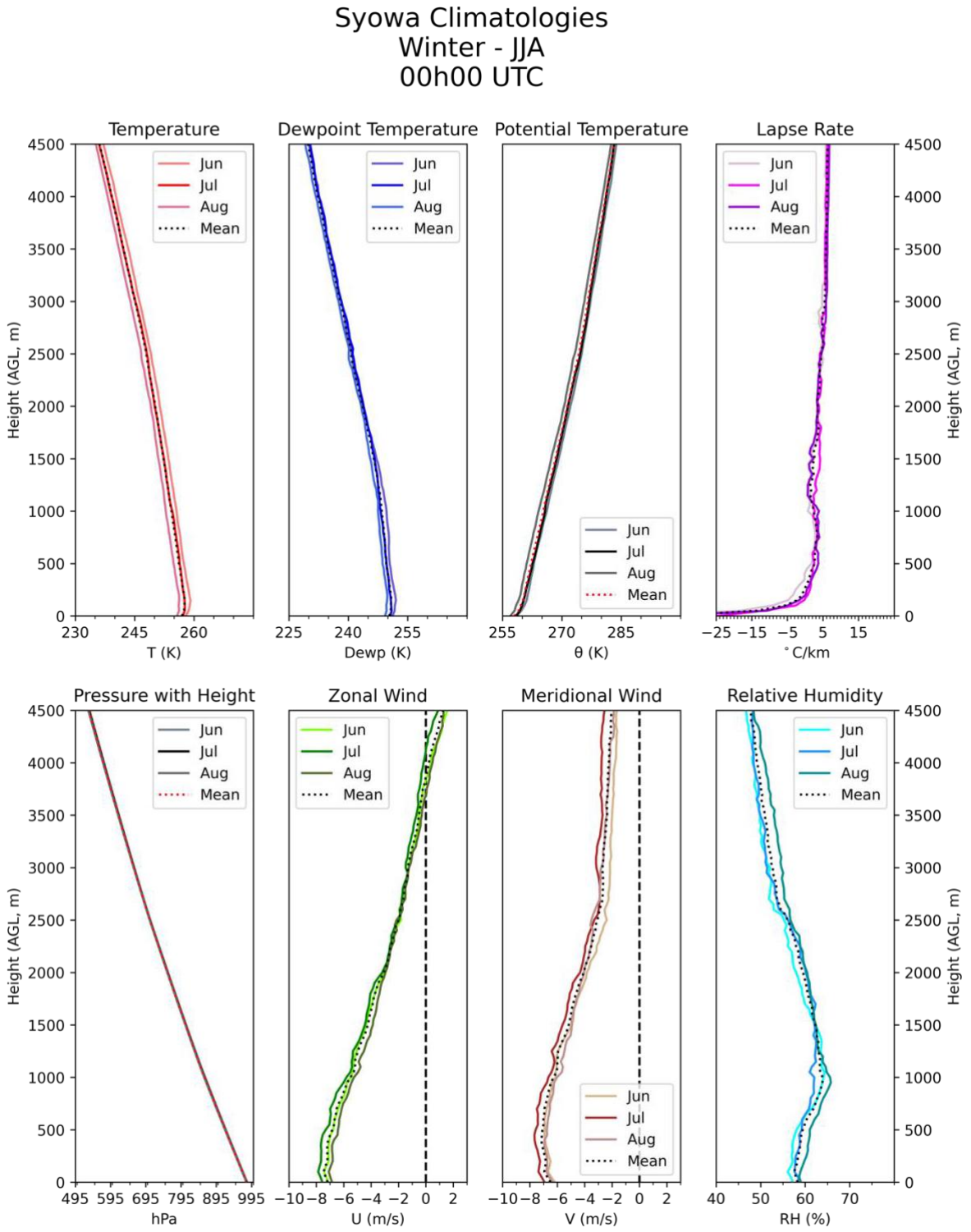

Figure 3.32: Syowa radiosonde observation climatologies for the months of June, July, and August (austral winter) at 00h00 UTC. The seasonal mean is also included for each parameter.

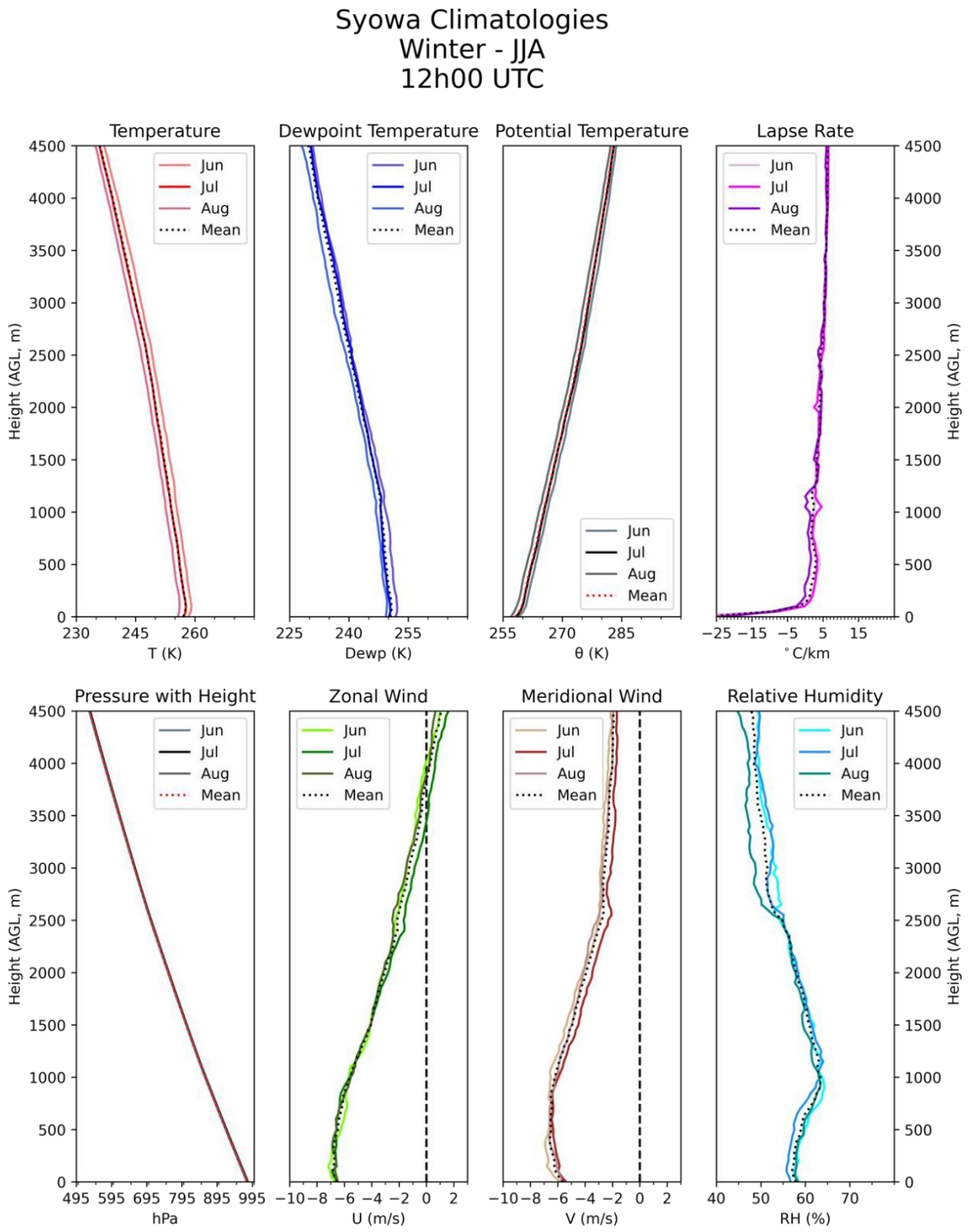

Figure 3.33: Syowa radiosonde observation climatologies for the months of June, July, and August (austral winter) at 12h00 UTC. The seasonal mean is also included for each parameter.

3.3.3.5. Climatology and seasonal variability of the ABLH for 00h00 and 12h00

Figure 3.34 and 3.35 indicates that the boundary layer height in Syowa for both 00h00 UTC and 12h00 UTC are shallow, except for the months of March and October. The shallow ABLH can be attributed to the presence of surface-based inversions throughout the different months of the year. The ABLH minima at 00h00 UTC is observed during the months of March and December, while for maxima it is observed for October. As a result, lowest ABLH are observed during the autumn season for 00h00 UTC, and observed during the spring season for 12h00 UTC.

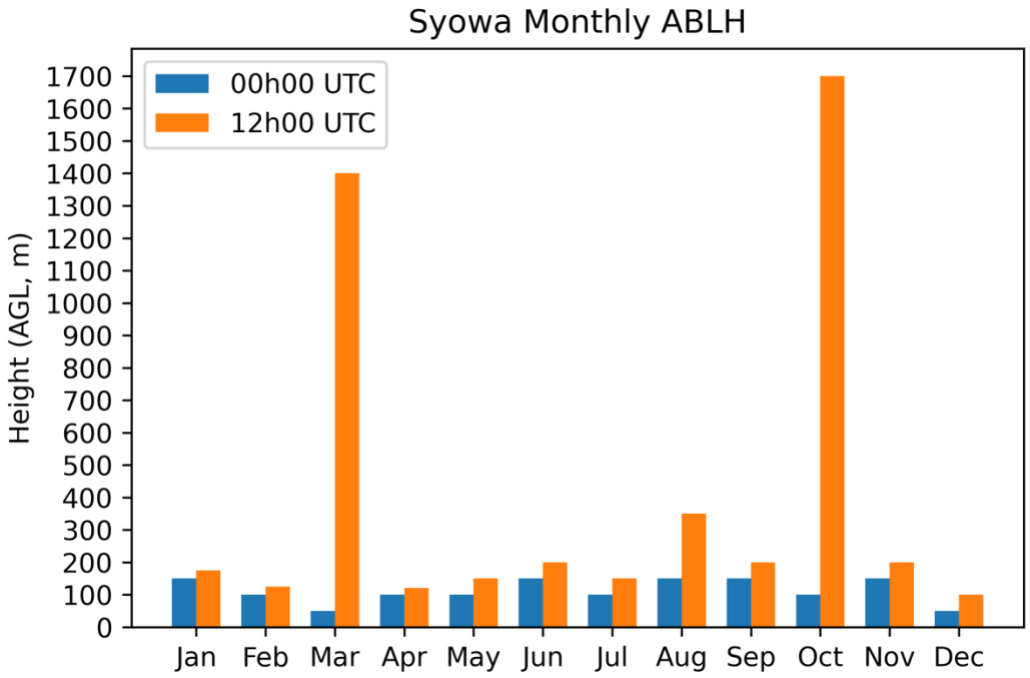

Figure 3.34: Monthly climatologies of the ABLH for 00h00 UTC (blue) and 12h00 UTC (orange) over Syowa.

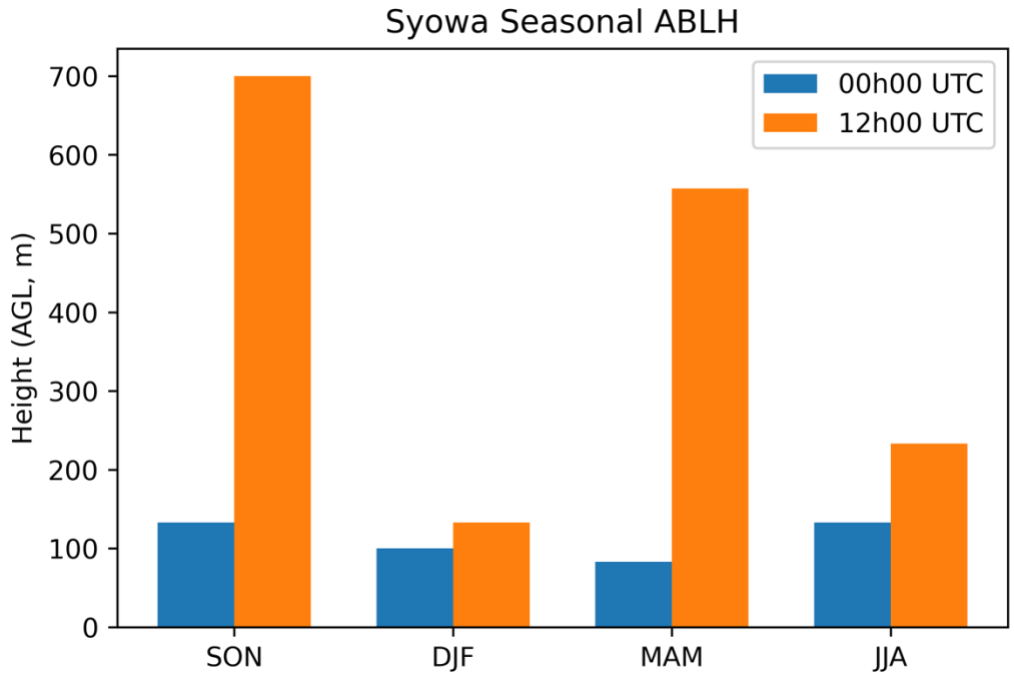

Figure 3.35: Seasonal climatologies of the ABLH for 00h00 UTC (blue) and 12h00 UTC (orange) over Syowa.

3.4. SUMMARY OF THE RESULTS

Our climatological analysis of the radiosonde data indicates that there persistently exists a temperature inversion over Irene at 00h00 UTC throughout all the months of the year. This inversion is more intense during the autumn and winter seasons, while it is not as pronounced during the spring and summer seasons. This agrees well with findings by Tyson et al. (1976), who also used radiosonde data to characterise temperature inversions in South Africa. Our results also affirm that of Tyson et al. (1976) in that they show that the environmental lapse rates correlate well with temperature inversions, with the autumn and winter months recording highly negative lapse-rates near the surface compared to the spring and summer seasons.

The radiosonde data analysis over Syowa also indicates the presence of surface-based inversion at 00h00 UTC for all the months of the year. The surface-based inversion was also observed for 12h00 during all the months except the summer months, May, October and November. This is expected as the Antarctic ABL is known to be frequented by surface-based inversions and has been found that this feature is stronger, deeper and frequent during the autumn and winter months (Zhang et al. 2011).

It was also found that monthly variability within the different seasons is prominently observed during the transitional seasons of autumn and spring, especially for thermodynamic variables. An interesting feature which was also observed over Irene and Syowa throughout all the seasons is a bulge in relative humidity above the surface. For Irene this is true for all the months of the year at 12h00 UTC, while for Syowa this bulge is observed for both 00h00 UTC and 12h00 UTC for all the month of the year. It is currently not known why this bulge exists, but we hypothesise that it is due to the presence of low-level jet (LLJ) (see Gimeno et al. 2016).

CHAPTER 4: EVALUATING THE CCAM IN SIMULATING PRESENT-DAY ABL HEIGHT AND ATTRIBUTES

4.1. INTRODUCTION

At a foundational level, boundary layer modelling seeks to represent the evolution and dissipation of turbulence. However, the turbulent mixing within the ABL occurs at short time and length scales (order of minutes and metres) compared to the free atmospheric flow. Therefore the effects of boundary layer turbulence to the resolved model dynamics is parameterised. This is done through modelling various processes occurring within the boundary layer, and those involved in the transport and entrainment at the bottom and top of the layer.

4.2. DATA AND METHODS

4.2.1. CCAM Variable-Resolution Global Atmospheric Model

The climate model used in our study is the variable-resolution global atmospheric model CCAM, developed by the Commonwealth Scientific and Industrial Research Organisation (CSIRO) in Australia. It employs a semi-implicit, semi-Lagrangian solution of the set of primitive equations on the conformal-cubic grid (McGregor 2005). CCAM was integrated at a horizontal grid length of 50 km, with 27 vertical levels, across the globe. The digital filter of Thatcher and McGregor (2009) was used to nudge temperature and horizontal wind every 6 hours towards the ERA-interim reanalysis data (Dee et al., 2011), from the 900 hPa level upwards. The ERA-interim sea-surface temperature (SST) and sea-ice data were used as lower boundary forcing. For this study, CCAM simulations were re-gridded to $0.5° \times 0.5°$ horizontal resolution and 101 vertical levels at 50 m from the surface to a height of 4500 m. The nearest-neighbour method was used to select the closest model grid-point to the relevant station. This process does introduce a smoothing error in terms of horizontal interpolation and due to the model grid-point not necessarily having the same altitude as the weather station. However, the model grid-point still reflects the representative synoptic conditions and consequently the same type of boundary layer climatology of the station. The CCAM data output we use in this study employs the local closure scheme which uses the gradient Richardson number method in determining the boundary layer height.

4.2.2. Simulating the Boundary Layer with the CCAM

The CCAM approach to simulating the boundary layer is in terms of the turbulent vertical mixing based on both local and non-local formulations. Two options are supported by the CCAM for boundary layer turbulent mixing. The atmosphere and ocean turbulent mixing

parameterisations can also be combined into a single implicit solution, which helps with robustness and accuracy, particularly for momentum (Thatcher 2021). The local approach employs the stability-dependent scheme based on the Monin-Obukhov similarity theory (McGregor et al. 1993). This was developed utilising the methods of the theory of similitudes by Monin and Obukhov (1954), which concluded that the vertical changes of mean flow, turbulence, characteristics in the surface layer is only dependent on the surface momentum flux measured by friction velocity, buoyancy flux, and height. However, the CCAM stability functions which relate the surface fluxes to their mean gradients, differs from the original suggestion by Monin and Obukhov (1954) in that it uses the gradient Richardson number instead of the height.

Therefore, the local scheme follows that of Equation (2.3), but the K diffusion coefficients are expressed in the form

$$K = l^2 \left|\frac{\partial v}{\partial z}\right| F_m(Ri_b) \tag{2.5}$$

with Blackadar's (1962) expression for the mixing length l written as

$$l = \frac{kz}{1+\frac{kz}{\lambda}} \tag{2.6}$$

k is the asymptomatic mixing length and is an adjustable constant. Variable z represents the height and for the stable and unstable cases, the function F_m is respectively represented by

$$F_m = (1 + b'_m Ri_b)^{-2} \tag{2.7}$$

and

$$F_m = 1 - \frac{b_m Ri_b}{1+c_m|Ri_b|^{1/2}} \tag{2.8}$$

where

$$c_m = 5C_{DN} b_m \left(\frac{z}{z_0}\right)^{1/2} \tag{2.9}$$

and

$$C_{DN} = \frac{k^2}{\{ln(\frac{z}{z_0})\}^2} \tag{2.10}$$

z_0 represents the roughness length for momentum, and k is the von Kármán constant. The Ri_b is the bulk Richardson number

$$Ri_b = \frac{g\frac{\partial\theta}{\partial z}}{\theta\left|\frac{\partial V}{\partial z}\right|^2} \tag{2.11}$$

where g is gravitational acceleration and θ is a column-wise potential temperature.

On the other hand, the non-local simulation of the boundary layer is based on the gradient diffusion approach, which depends on the diffusion coefficient K and gradients of mean

variables (McGregor et al. 1993). The scheme employed to calculate K is formulated from the turbulence kinetic energy and the eddy dissipation rate, and uses the eddy-diffusivity/mass-flux approach described by Hurley (2007). This approach uses a mass-flux scheme following Soares et al. (2004) which parameterises the counter-gradient term in the vertical heat flux equation.

Expanding from Equation (2.4), the turbulence scheme used to calculate K is the standard $E-\varepsilon$ model. The model respectively solves the prognostic equations for the turbulence kinetic energy (E) and the eddy dissipation rate (ε) as follows

$$\frac{dE}{dt} = \frac{\partial}{\partial z}\left(K\frac{\partial E}{\partial z}\right) + P_S + P_b - \varepsilon \tag{2.12}$$

and

$$\frac{d\varepsilon}{dt} = \frac{\partial}{\partial z}\left(c_{\varepsilon 0}K\frac{\partial \varepsilon}{\partial \sigma}\right) + \frac{\varepsilon}{E}\left(c_{\varepsilon 1}\left(P_S + max\left(0, P_b\right)\right) + max(0, P_T)\right) - c_{\varepsilon 2}\varepsilon) \tag{2.13}$$

where

$$P_S = K\left(\left(\frac{\partial u}{\partial z}\right)^2 + \left(\frac{\partial v}{\partial z}\right)^2\right) \tag{2.14}$$

$$P_b = -\frac{g}{\theta_v}K\left(\frac{\partial \theta_v}{\partial z} - \gamma_{\theta_v}\right) \tag{2.15}$$

$$P_T = -\frac{\partial}{\partial z}\left(K\frac{\partial E}{\partial z}\right) \tag{2.16}$$

$$K = c_m\frac{E^2}{\varepsilon} \tag{2.17}$$

and $c_m = 0.09$, $c_{\varepsilon 0} = 0.69$, $c_{\varepsilon 1} = 1.46$, and $c_{\varepsilon 2} = 1.83$.

4.2.3. Data Post-Processing

The CCAM simulated variables analysed in this study are temperature, dewpoint temperature, potential temperature, pressure, zonal wind, meridional wind, relative humidity and ABLH, for 00h00 UTC and 12h00 UTC. We also used Equation 3.3 of Chapter 3 to calculate the temperature lapse-rate, which was also analysed and evaluated. Before any analysis was performed, the 00h00 UTC and 12h00 UTC monthly climatologies were computed for each field, averaged over the period 1 January 1979 to 31 December 2017. The resulting monthly climatologies were then used to determine mean seasonal values. The seasons are categorised as follows: September, October and November (SON) represent spring; December, January, and February (DJF) represent summer; March, April and May (MAM) represents autumn; June, July, and August (JJA) represents winter.

After analysing each model field, we then use observational data analysed in Chapter 3 to calculate the model bias for each level as follows:

$$Bias = model\ value - observed\ value \tag{4.1}$$

Model bias is calculated to determine any systematic errors or inaccuracies by the model for each given field.

4.3. RESULTS

The results of the analysis of the CCAM simulations, including model biases, are divided into three main sections. Section 4.4.1 discusses the analysis of the model data over the Irene station, starting with the subsection focusing on the seasonal climatologies of variables for 00h00 and 12h00. The second subsection focuses on the ABLH seasonal climatologies and their bias as compared to the radiosonde data. Section 4.4.2 and Section 4.4.3 follows the same pattern of analysis but are respectively for the Marion Island and Syowa stations.

4.3.1. Irene Station

4.3.1.1. The SON season and bias for 00h00 and 12h00

CCAM seasonal mean data for the spring months of September, October and November almost follow the same pattern as the observed data at 00h00 UTC over Irene (Figure 4.1).

Figure 4.1 indicates that the observed temperature inversion is also captured by the model. However, this feature is overestimated by 3 K, including the temperature values for the entire depth, which has positive biases of between 1 K and 3 K. Dewpoint temperature values are almost accurately predicted for heights below 1000 m, while at levels above 1000 m there are positive biases not exceeding 6 K. It is interesting to note that this positive bias corresponds with a positive relative humidity bias above the 1000 m level.

It is also of interest to note that the CCAM accurately simulated the potential temperature values above 1 500 m. This is also true for temperature lapse-rate, albeit with negative bias near the surface. Another interesting feature accurately simulated by the CCAM is the reversed S-shaped meridional wind pattern. Apart from the near-surface, this pattern and values match those observed by the radiosonde. On the other hand, pressure values depicted by the CCAM have a positive bias of between 10 hPa and 12 hPa, while zonal wind values are underestimated by as much 2 m/s

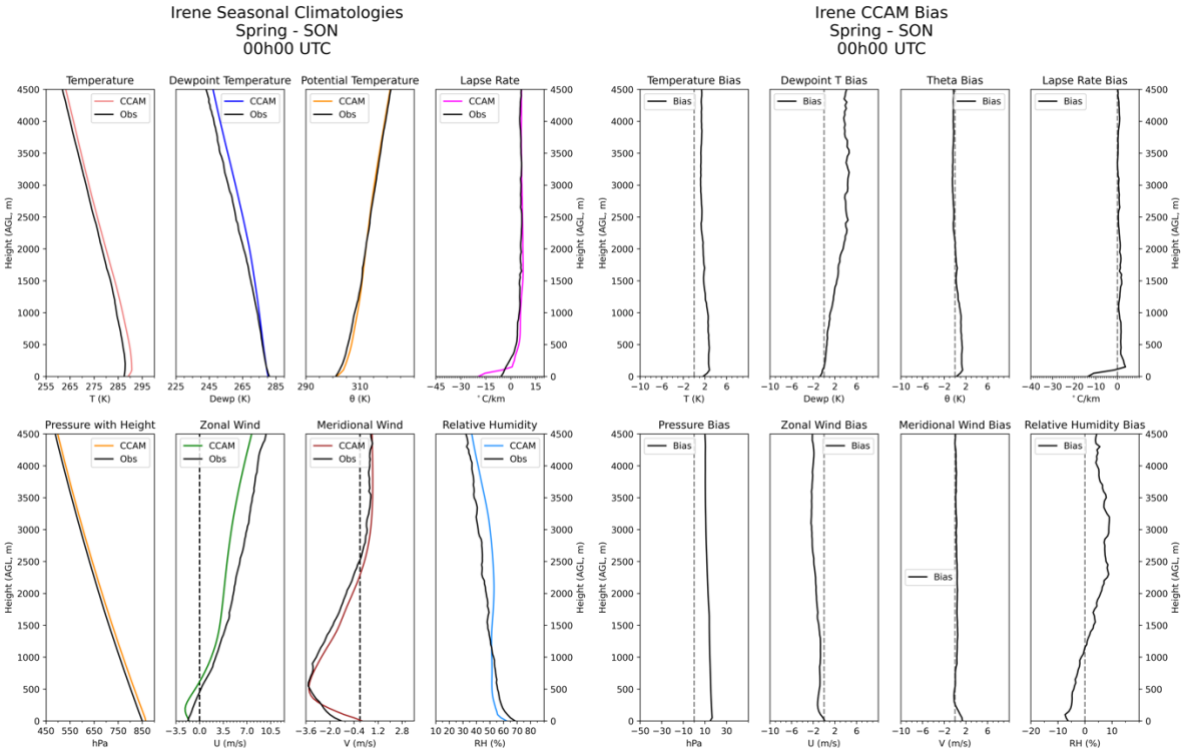

Figure 4.1: Irene 00h00 UTC austral spring seasonal mean CCAM and radiosonde vertical profiles, including the CCAM bias, of temperature, dewpoint temperature, potential temperature, lapse-rate, pressure, zonal wind, meridional wind, and relative humidity.

Figure 4.2 indicates an accurate depiction of the reversed S-shaped meridional wind pattern at 12h00 UTC. This is also true for temperature lapse-rate, although there is negative bias near the surface. It is interesting to note that dewpoint temperature and relative humidity are similarly biased as at 00h00 UTC. This may be an indicator that the CCAM produces too much moisture above the surface. The pressure bias at 12h00 UTC is similar to the one at 00h00 UTC.

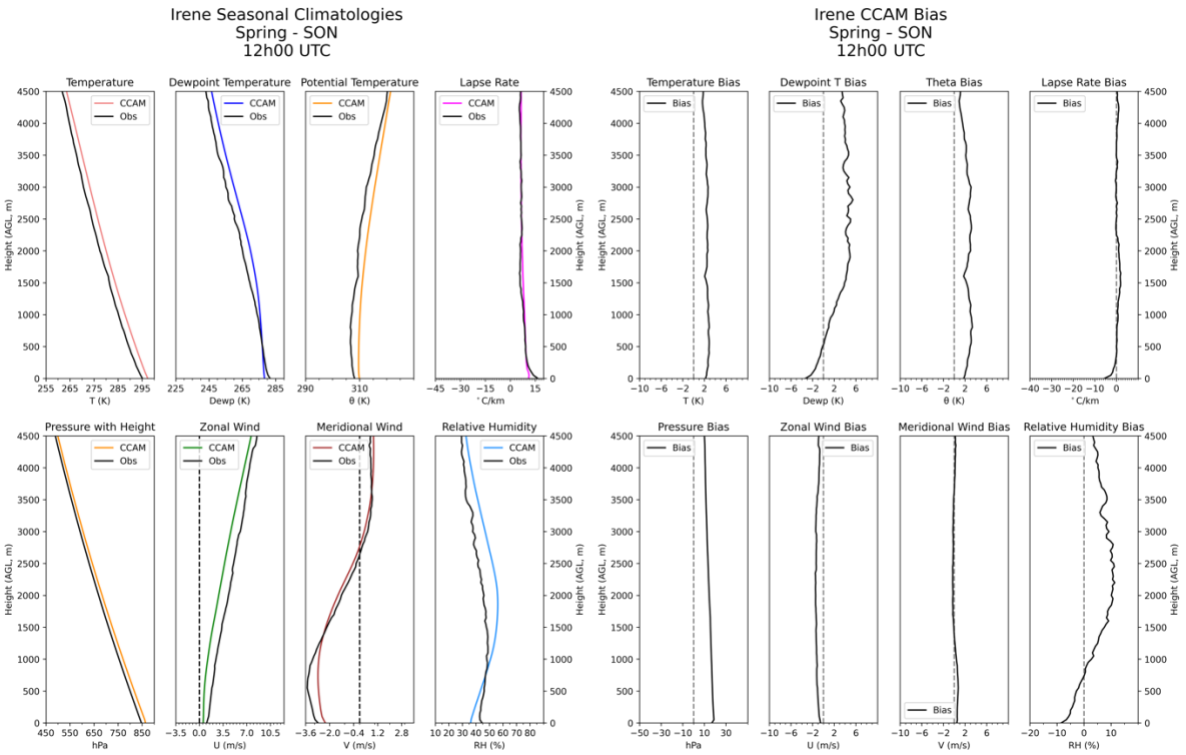

Figure 4.2: Irene 12h00 UTC austral spring seasonal mean CCAM and radiosonde vertical profiles, including the CCAM bias, of temperature, dewpoint temperature, potential temperature, lapse-rate, pressure, zonal wind, meridional wind, and relative humidity.

4.3.1.2. The DJF season and bias for 00h00 and 12h00

The temperature inversion for the summer months of December, January and February at 00h00 UTC is also well captured by the CCAM, although it is positively biased as with the spring months (see Figure 4.3). It is interesting to note that the CCAM also captured the reserved S-shaped meridional wind pattern, except near the surface where there is a positive bias of up to 2 m/s. The model still overestimates the above surface moisture, while potential temperature and zonal wind are almost accurately represented by the CCAM.

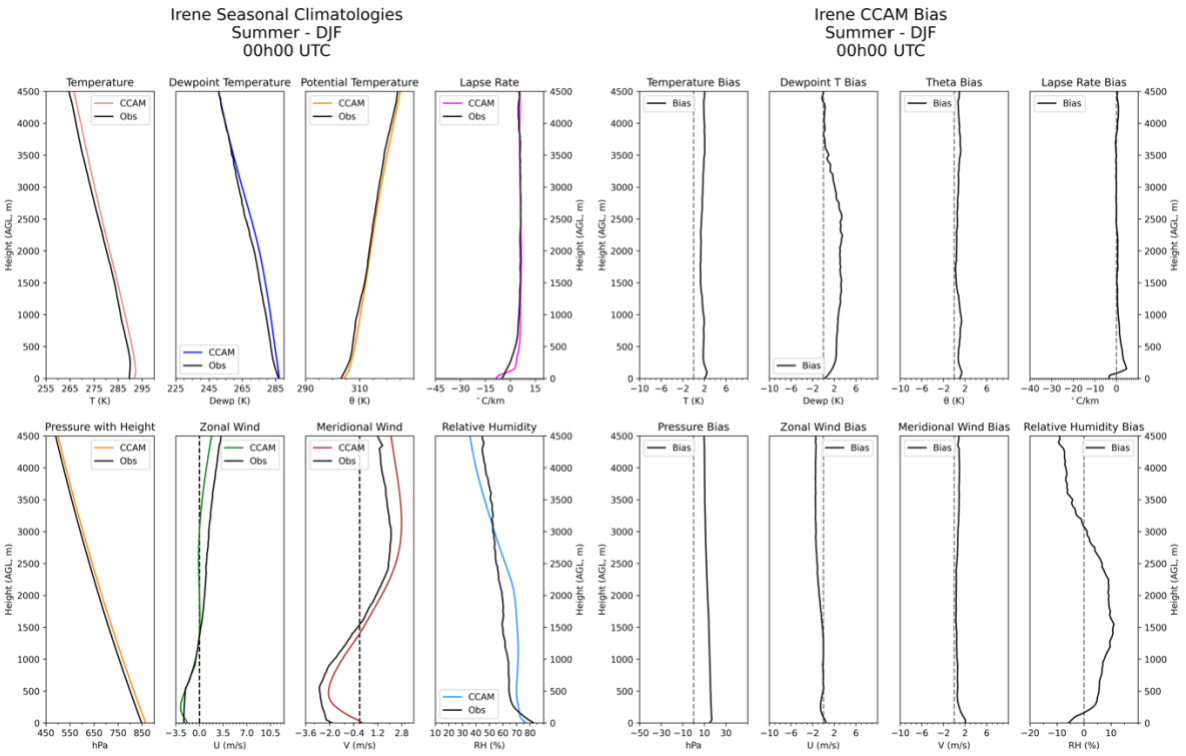

Figure 4.3: Irene 00h00 UTC austral summer seasonal mean CCAM and radiosonde vertical profiles, including the CCAM bias, of temperature, dewpoint temperature, potential temperature, lapse-rate, pressure, zonal wind, meridional wind, and relative humidity.

Figure 4.4 indicates that the zonal and meridional winds are almost accurately captured by the CCAM at 12h00 UTC during the summer months. This is also true for temperature lapse-rate. The positive pressure bias is persistently present throughout the seasons, including the positive moisture bias above the surface.

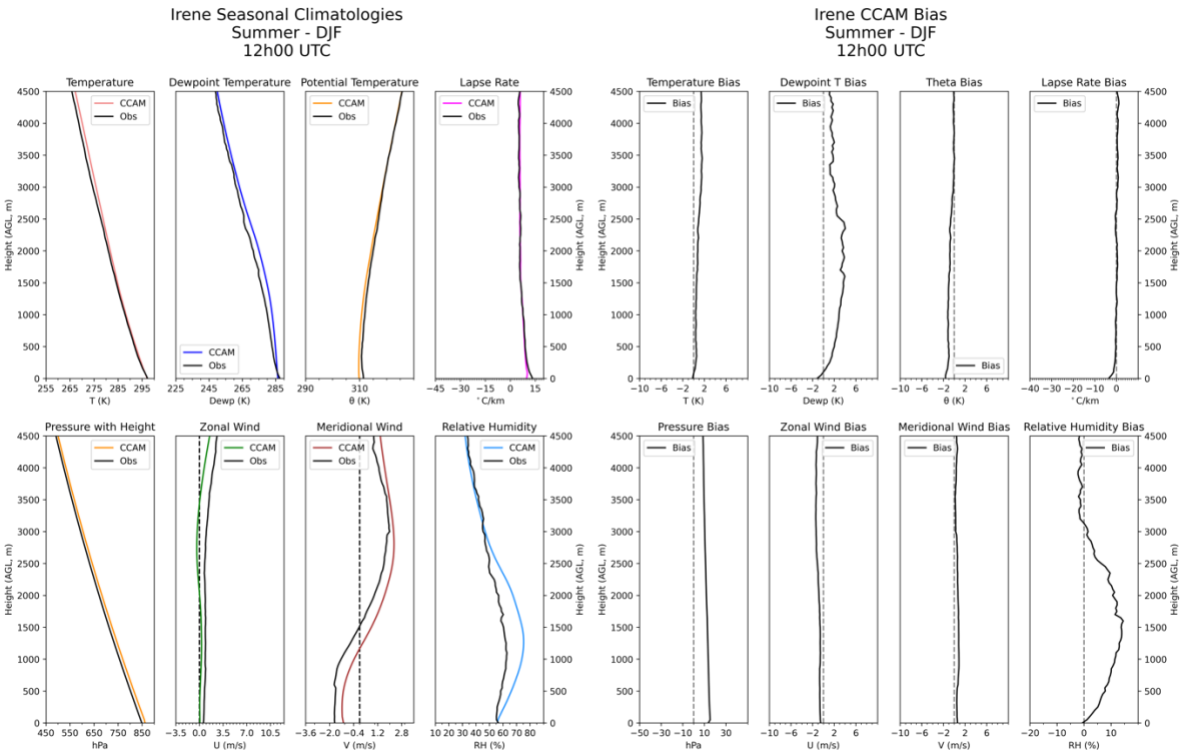

Figure 4.4: Irene 12h00 UTC austral summer seasonal mean CCAM and radiosonde vertical profiles, including the CCAM bias, of temperature, dewpoint temperature, potential temperature, lapse-rate, pressure, zonal wind, meridional wind, and relative humidity.

4.3.1.3. The MAM season and bias for 00h00 and 12h00

During the autumn months of March, April and May, at 00h00 UTC (see Figure 4.5), temperature lapse-rate values are greatly negatively biased near the surface. The temperature inversion is also overestimated by the CCAM, including the potential temperature near the surface, and zonal wind above the 1000 m height. The meridional wind patterns are almost accurately predicted by the CCAM, while the positive moisture bias above the surface still persists.

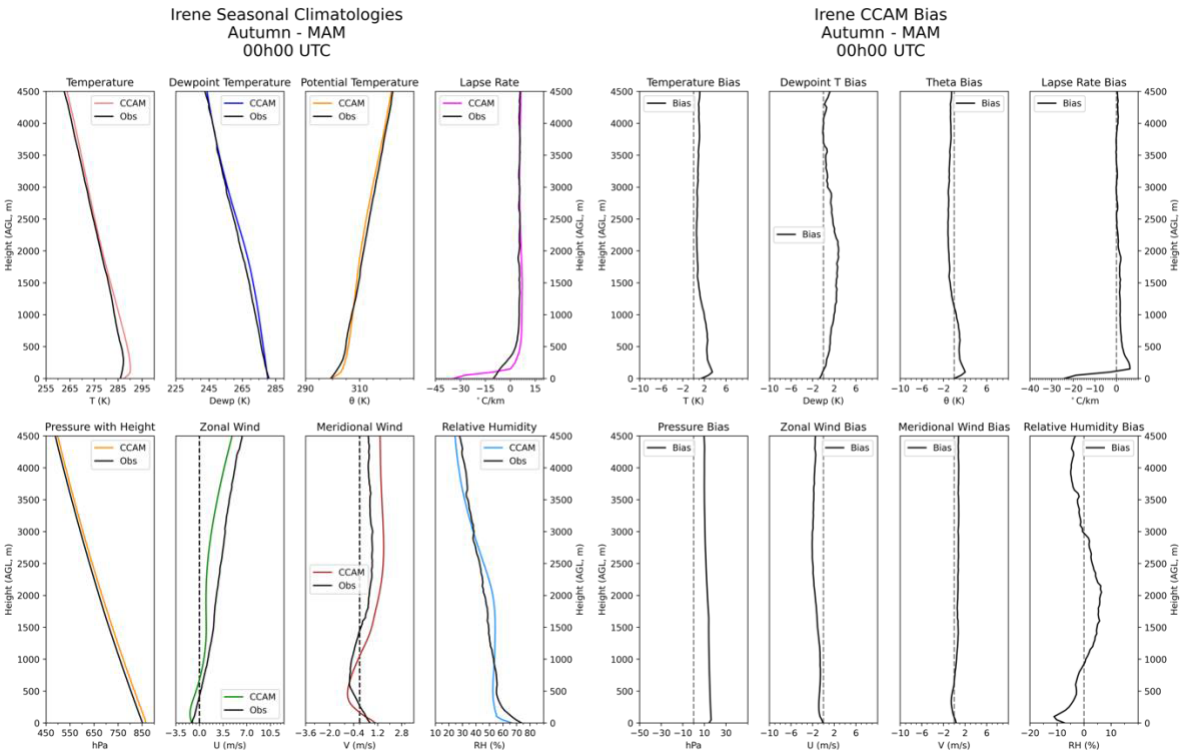

Figure 4.5: Irene 00h00 UTC austral autumn seasonal mean CCAM and radiosonde vertical profiles, including the CCAM bias, of temperature, dewpoint temperature, potential temperature, lapse-rate, pressure, zonal wind, meridional wind, and relative humidity.

Figure 4.6 indicates that the CCAM almost accurately captures the temperature, potential temperature, temperature lapse-rate, zonal and meridional wind, while pressure, dewpoint temperature, and relative humidity values are persistently overestimated throughout the vertical depth (for pressure) and above the surface (for dewpoint temperature and relative humidity).

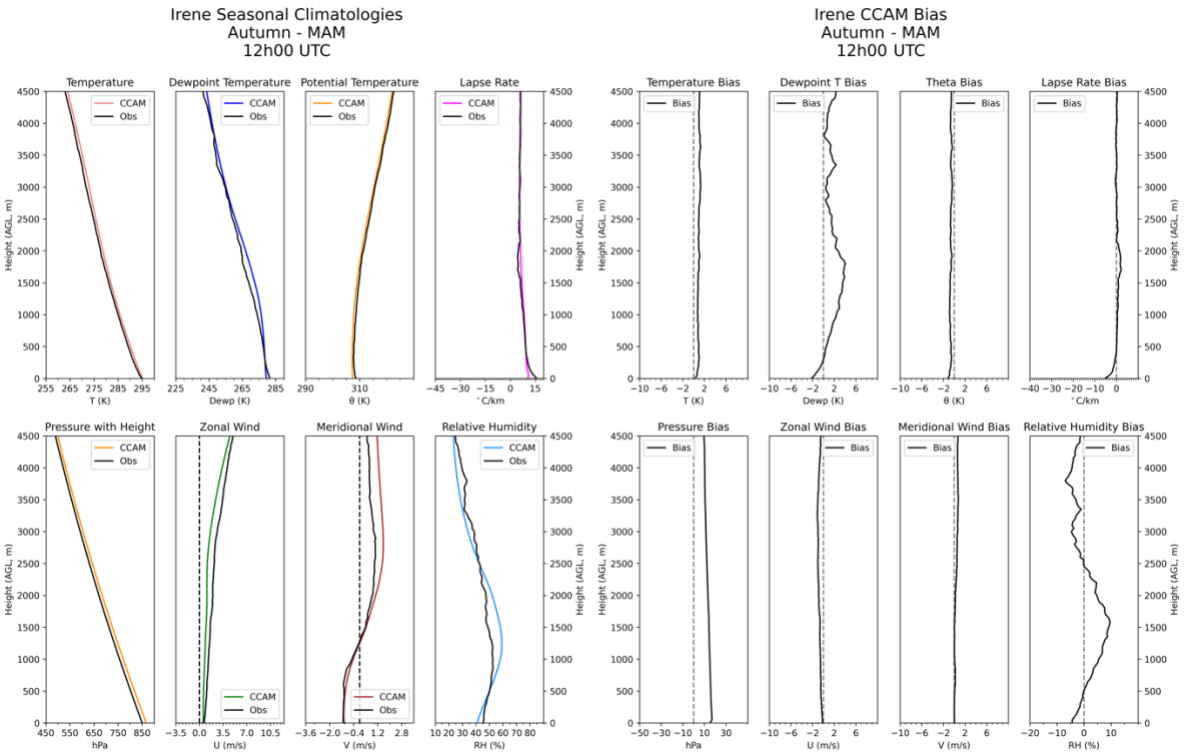

Figure 4.6: Irene 12h00 UTC austral autumn seasonal mean CCAM and radiosonde vertical profiles, including the CCAM bias, of temperature, dewpoint temperature, potential temperature, lapse-rate, pressure, zonal wind, meridional wind, and relative humidity.

4.3.1.4. The JJA season and bias for 00h00 and 12h00

During the winter months of June, July and August at 00h00 UTC (see Figure 4.7), the near-surface temperature values as well as the strength of thethe temperature inversion are overestimated by the CCAM. This corresponds well with high negatively biased temperature lapse-rates. The potential temperature is also overestimated by the CCAM. It is interesting to note that the above-surface positive dewpoint temperature and relative humidity biases continue to persist even during the winter season.

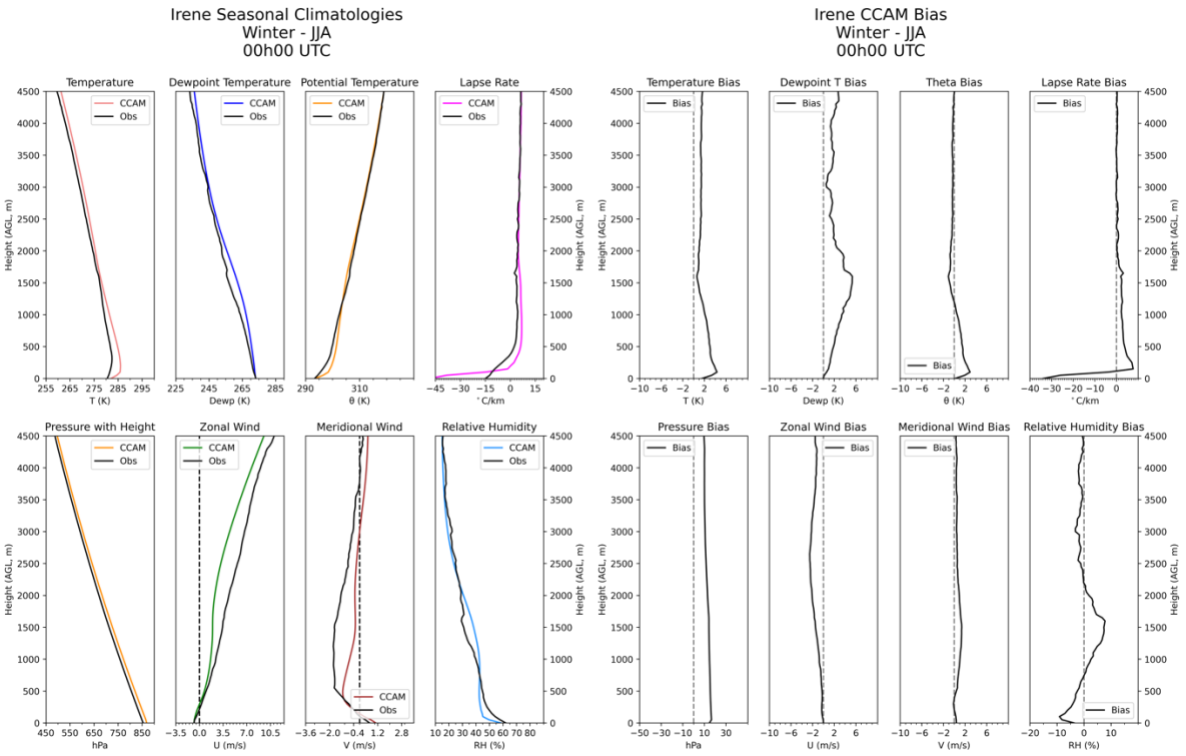

Figure 4.7: Irene 00h00 UTC austral winter seasonal mean CCAM and radiosonde vertical profiles, including the CCAM bias, of temperature, dewpoint temperature, potential temperature, lapse-rate, pressure, zonal wind, meridional wind, and relative humidity.

Figure 4.8 indicates that during the winter months over Irene at 12h00 UTC, values for potential temperature, temperature lapse-rate, and meridional wind, are accurately depicted by CCAM. The above surface positive moisture bias represented by the dewpoint temperature and relative humidity values continue to persist. This bias is present throughout the seasons at both 00h00 UTC and 12h00 UTC times. This persistent above-surface positive bias for dewpoint temperature and relative humidity, can be interpreted as a systematic error by the CCAM, because of too much moisture being produced above the surface.

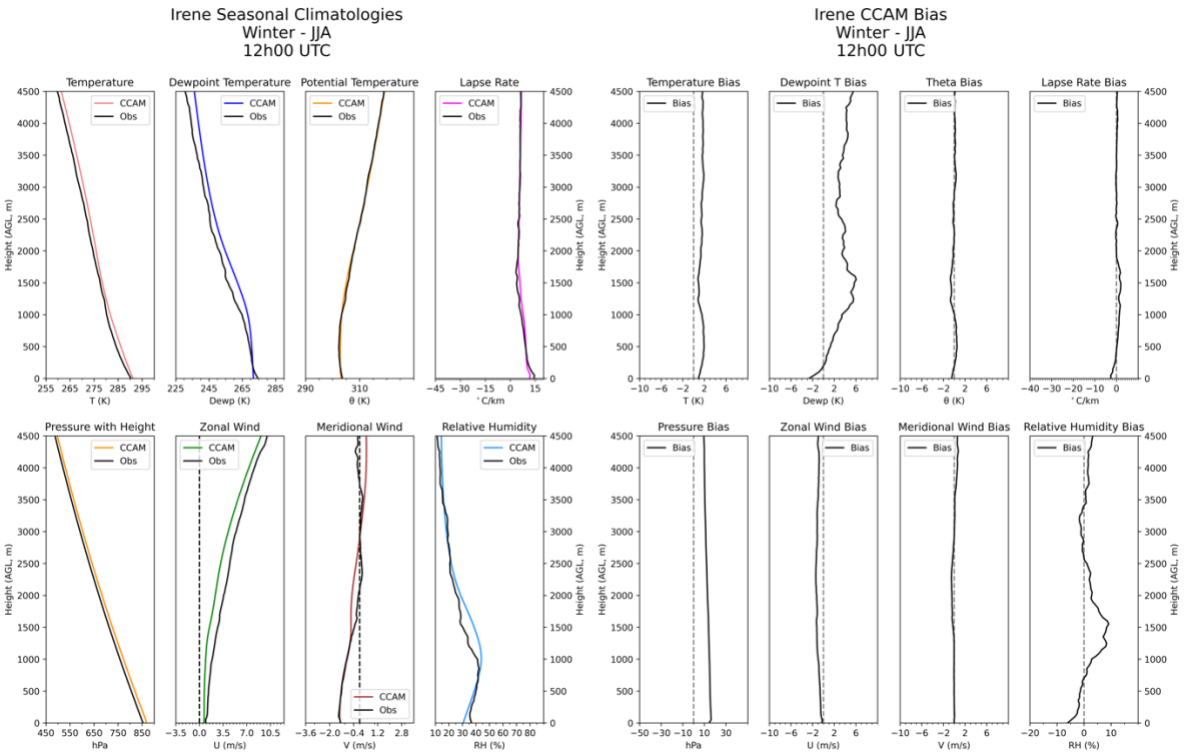

Figure 4.8: Irene 12h00 UTC austral winter seasonal mean CCAM and radiosonde vertical profiles, including the CCAM bias, of temperature, dewpoint temperature, potential temperature, lapse-rate, pressure, zonal wind, meridional wind, and relative humidity.

4.3.1.5. Climatology and seasonal variability of the ABLH for 00h00 and 12h00

Figure 4.9 and Figure 4.10 respectively represents ABLH simulations by the CCAM and its bias as compared to the ABLH calculated in Chapter 3. It is interesting to note that the CCAM indicates shallow ABLH throughout the seasons over Irene at 00h00 UTC. These are negatively biased by up to 200 m as compared to ABLH calculation from radiosondes. On the other hand, 12h00 UTC ABLH heights from the CCAM indicates that the spring season has highest mean values, while the summer season has the lowest mean values. It is interesting to note that this was also found to be the case from radiosonde observations, although CCAM overestimates these values for all seasons.

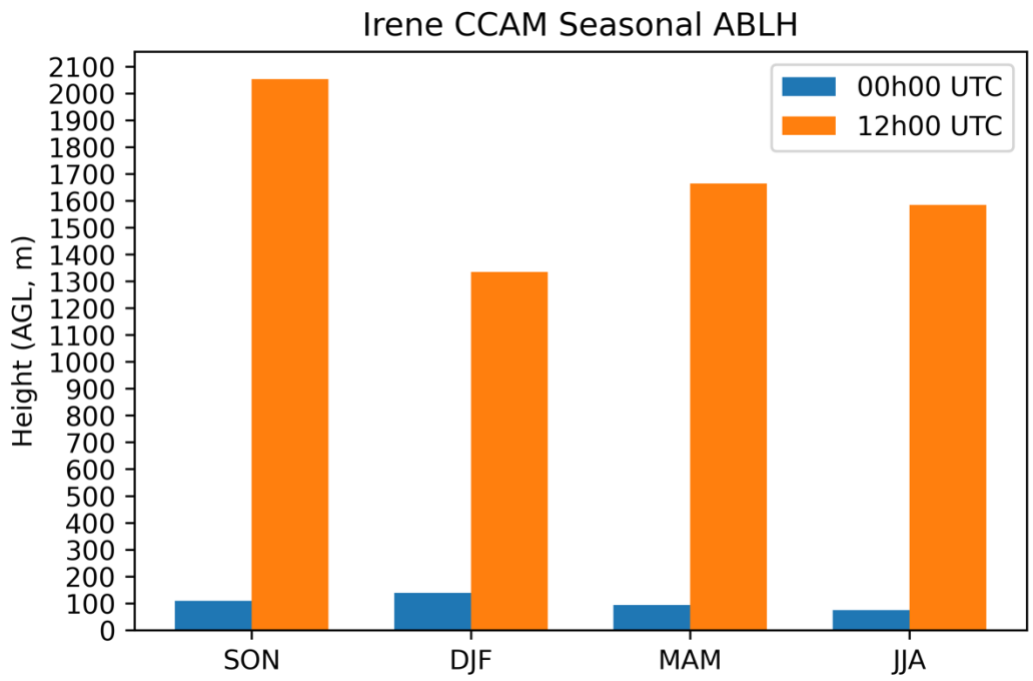

Figure 4.9: CCAM seasonal climatologies of the ABLH for 00h00 UTC (blue) and 12h00 UTC (orange) over Irene.

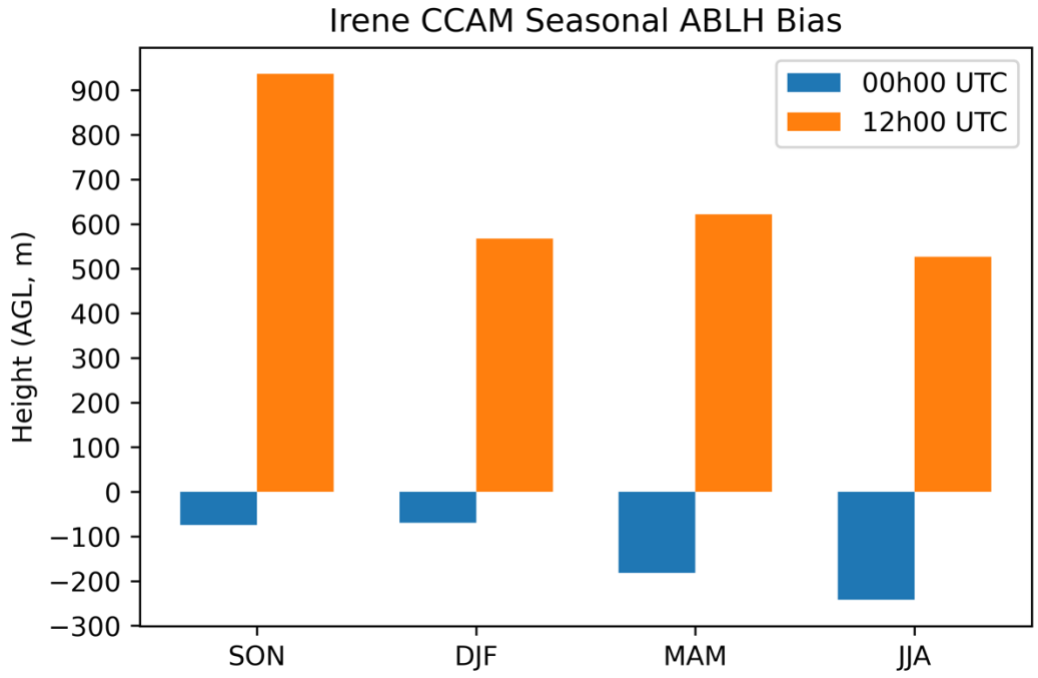

Figure 4.10: CCAM seasonal bias of the ABLH for 00h00 UTC (blue) and 12h00 UTC (orange) over Irene.

4.3.2. Marion Island Station

4.3.2.1. The SON season and bias for 00h00 and 12h00

During the spring months of September, October, and November, over Marion Island, Figure 4.11 shows that the 00h00 UTC CCAM representations of temperature, potential temperature, temperature lapse-rate, and meridional wind is almost similar to the observations by radiosonde. Unlike over the Irene station, pressure values depicted by the CCAM over Marion Island are also almost similar to the observed ones. It is interesting to note that the dewpoint temperature and relative humidity values indicate that the CCAM is positively biased above the near-surface. This bias is even more pronounced than over Irene, especially for relative humidity.

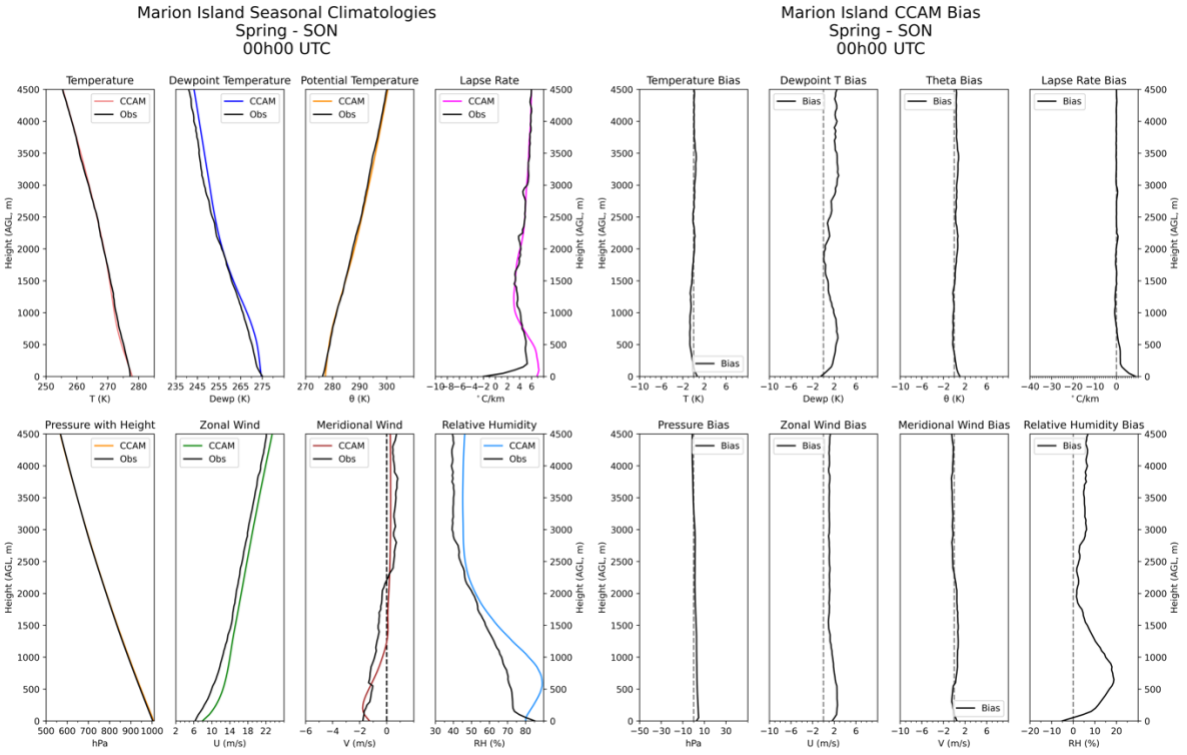

Figure 4.11: Marion Island 00h00 UTC austral spring seasonal mean CCAM and radiosonde vertical profiles, including the CCAM bias, of temperature, dewpoint temperature, potential temperature, lapse-rate, pressure, zonal wind, meridional wind, and relative humidity.

Figure 4.12 indicates that the CCAM performs well in capturing temperature, potential temperature, temperature lapse-rate and meridional wind patterns and values at 12h00 UTC over Marion Island. The depiction of pressure and zonal wind is also almost similar to observations, except that it is slightly positively biased, especially near the surface. The

dewpoint temperature and relative humidity is still positively biased especially above the near-surface.

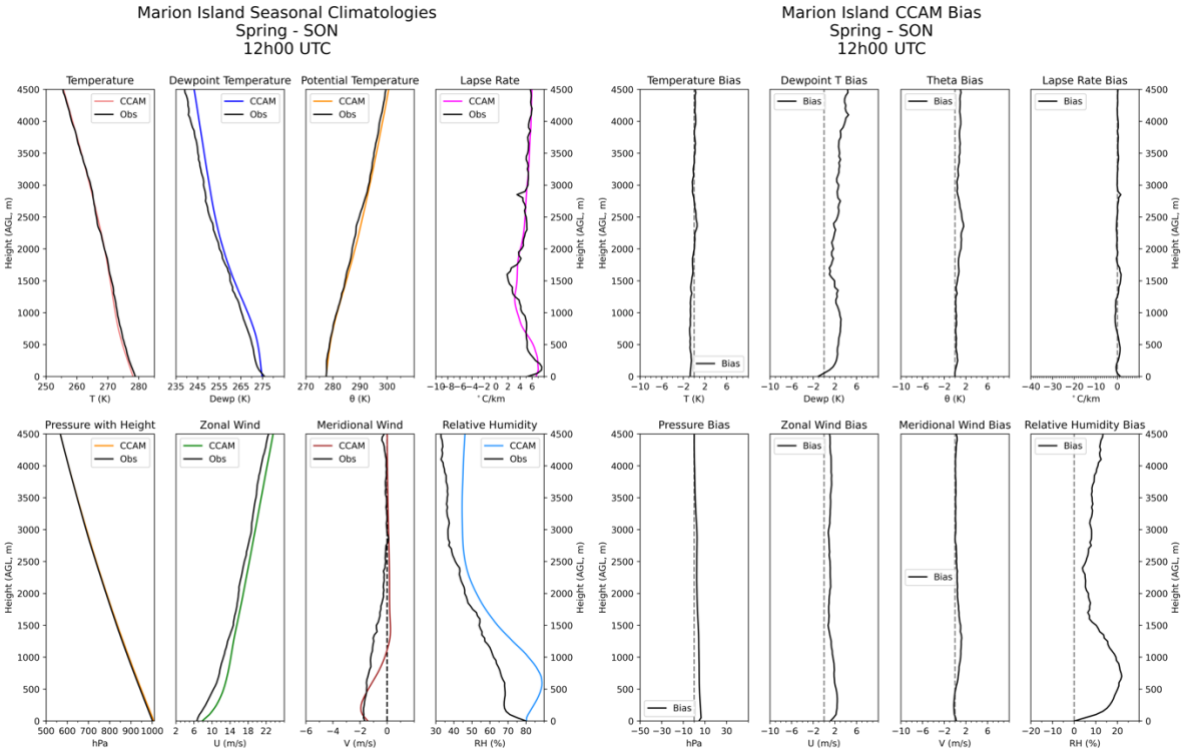

Figure 4.12: Marion Island 12h00 UTC austral spring seasonal mean CCAM and radiosonde vertical profiles, including the CCAM bias, of temperature, dewpoint temperature, potential temperature, lapse-rate, pressure, zonal wind, meridional wind, and relative humidity.

4.3.2.2. The DJF season and bias for 00h00 and 12h00

The summer months of December, January, and February over Marion Island at 00h00 are well represented by the CCAM. This is especially true for temperature, and temperature lapse-rate (see Figure 4.13). The zonal and meridional winds are also well represented by the CCAM, although there is slight positive bias from the surface to just below 1500 m for zonal wind, and between 500 m and 2500 m for meridional wind. This is also true for temperature lapse-rate near the surface. Relative humidity is overestimated by the CCAM above the surface.

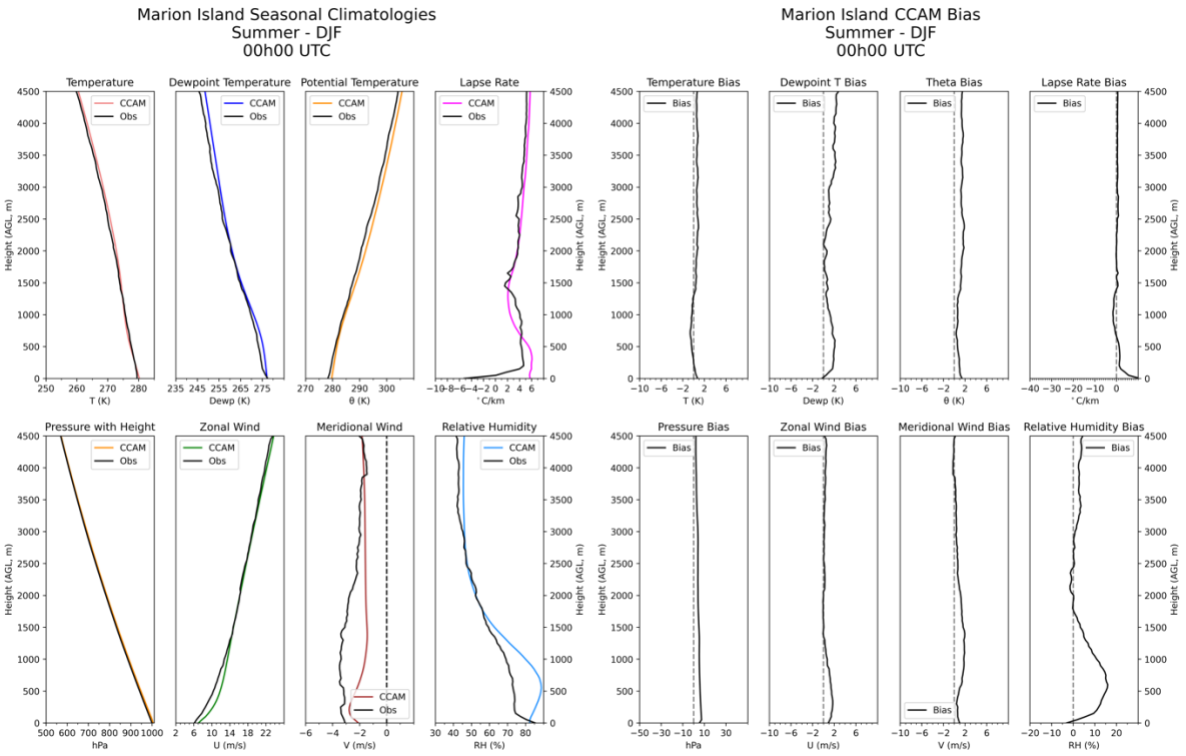

Figure 4.13: Marion Island 00h00 UTC austral summer seasonal mean CCAM and radiosonde vertical profiles, including the CCAM bias, of temperature, dewpoint temperature, potential temperature, lapse-rate, pressure, zonal wind, meridional wind, and relative humidity.

The positive relative humidity bias is also seen at 12h00 UTC as shown by Figure 4.14. The biases of pressure, zonal wind and meridional wind, follow the same patterns as the 00h00 UTC analysis, including for potential temperature. The temperature and temperature lapse-rate observations are well-represented by the CCAM.

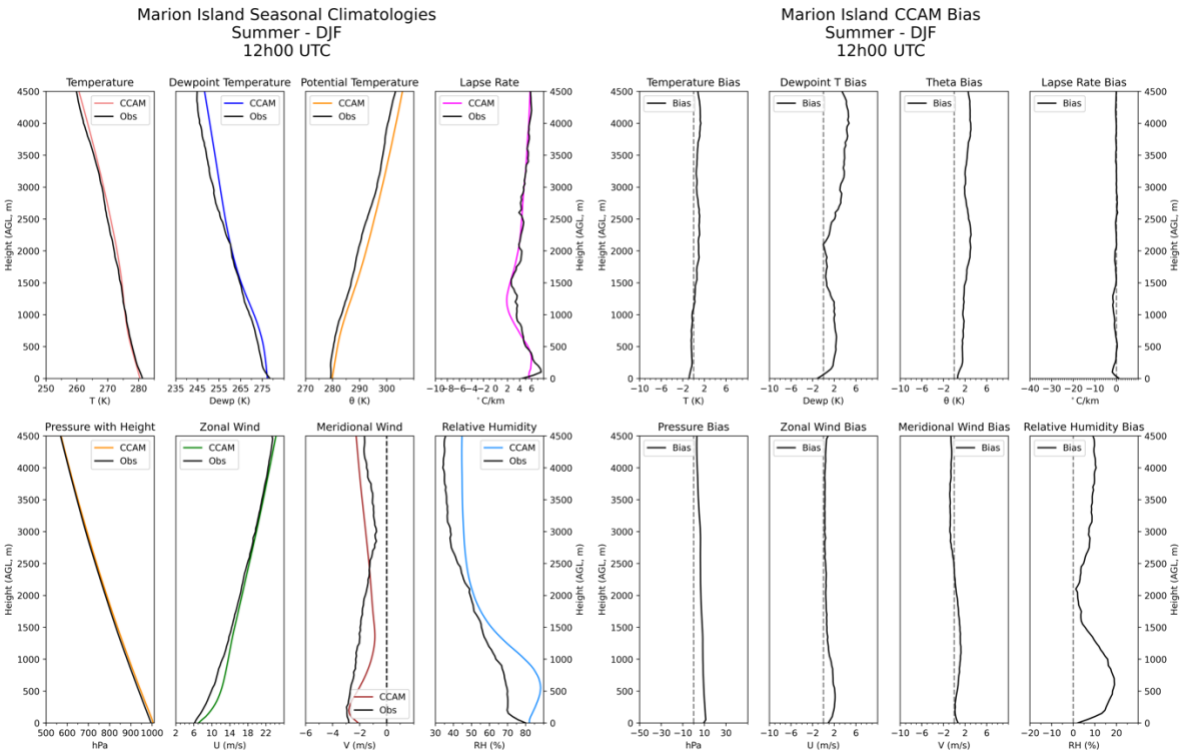

Figure 4.14: Marion Island 12h00 UTC austral summer seasonal mean CCAM and radiosonde vertical profiles, including the CCAM bias, of temperature, dewpoint temperature, potential temperature, lapse-rate, pressure, zonal wind, meridional wind, and relative humidity.

4.3.2.3. The MAM season and bias for 00h00 and 12h00

The 00h00 UTC and 12h00 UTC analysis over the autumn months of March, April and May (see Figure 4.15 and Figure 4.16), continue to indicate a positive bias by relative humidity, dewpoint temperature, potential temperature, and pressure. On the other hand, the depiction of temperature, and temperature lapse-rate values and patterns are also almost similar to observed ones.

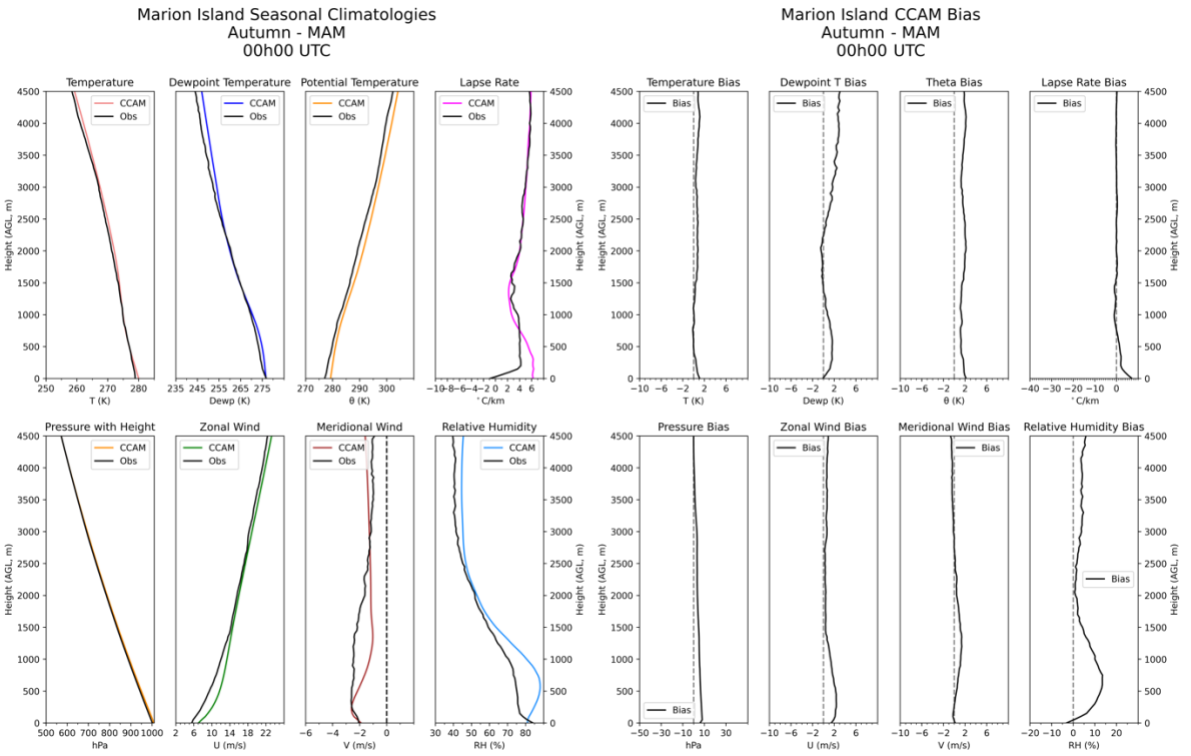

Figure 4.15: Marion Island 00h00 UTC austral autumn seasonal mean CCAM and radiosonde vertical profiles, including the CCAM bias, of temperature, dewpoint temperature, potential temperature, lapse-rate, pressure, zonal wind, meridional wind, and relative humidity.

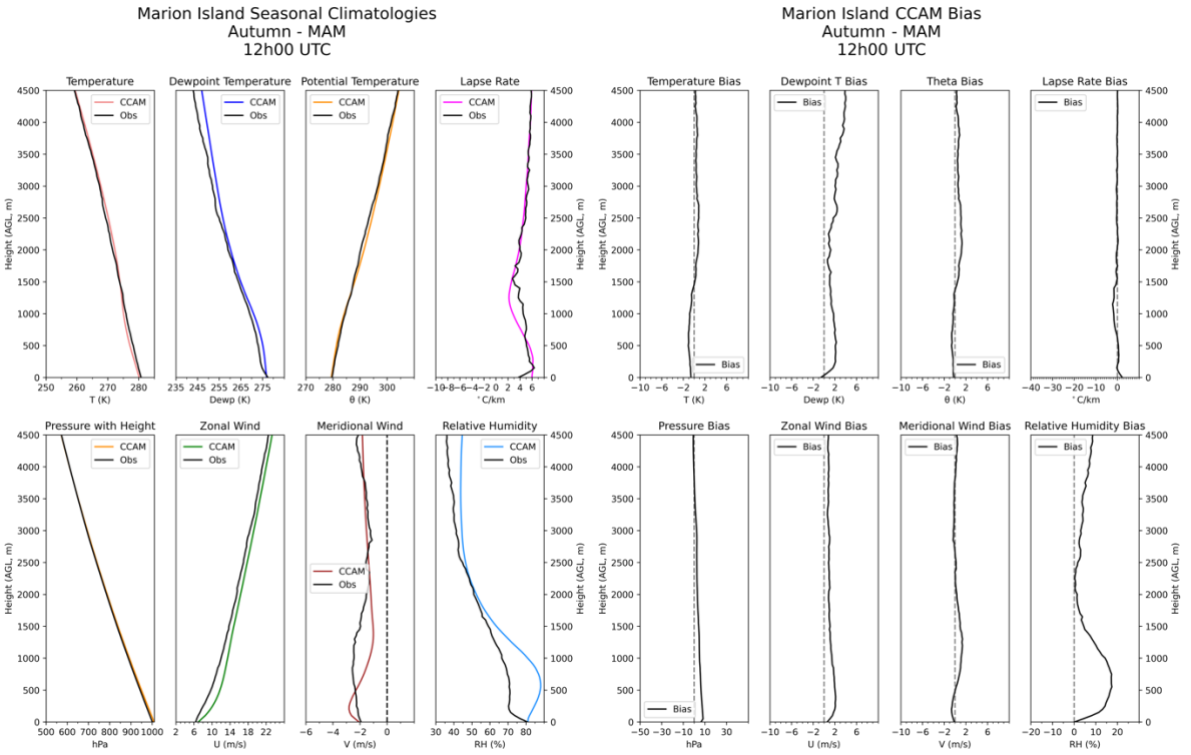

Figure 4.16: Marion Island 12h00 UTC austral autumn seasonal mean CCAM and radiosonde vertical profiles, including the CCAM bias, of temperature, dewpoint temperature, potential temperature, lapse-rate, pressure, zonal wind, meridional wind, and relative humidity.

4.3.2.4. The JJA season and bias for 00h00 and 12h00

It is interesting to note that the CCAM fails to represent the very shallow temperature inversion observed at 00h00 UTC during the winter months of June, July and August over Marion Island (See Figure 4.17). However, the depiction of temperature lapse-rate, and meridional wind, at 00h00 UTC and 12h00 UTC (see Figure 4.18) are very similar to observations. The positive biases of relative humidity and dewpoint temperature at both hours continue to be seen during this season, including for pressure values.

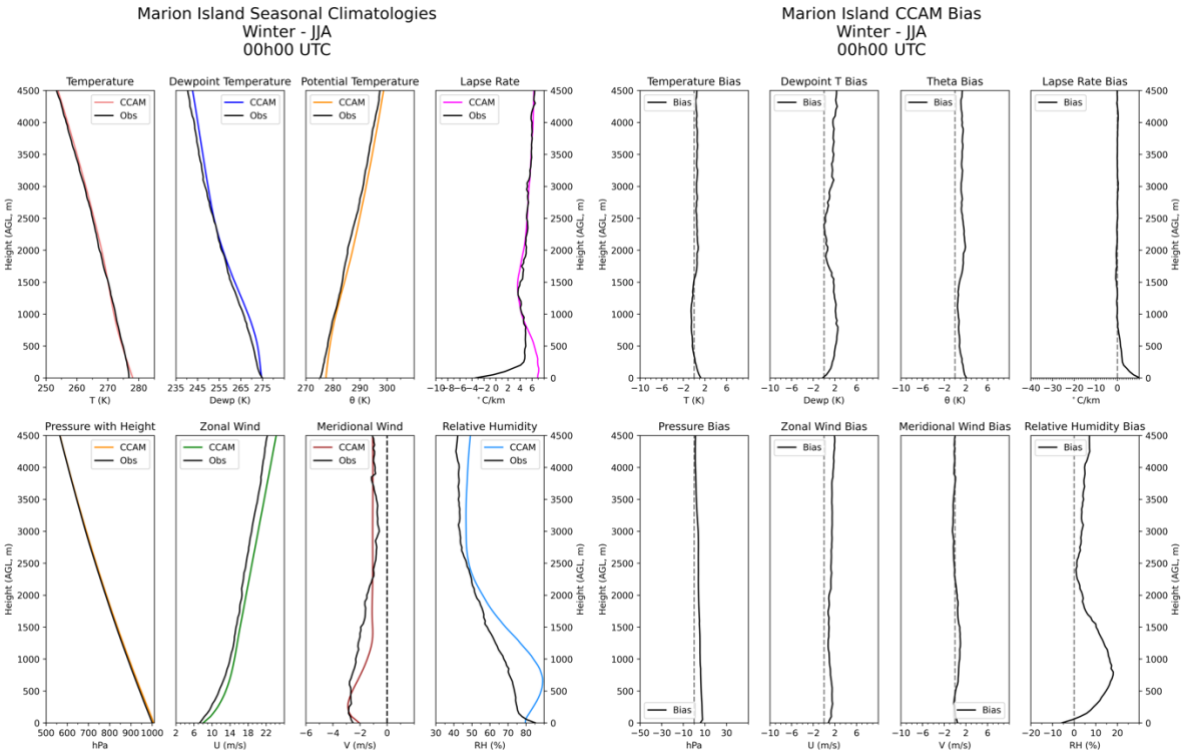

Figure 4.17: Marion Island 00h00 UTC austral winter seasonal mean CCAM and radiosonde vertical profiles, including the CCAM bias, of temperature, dewpoint temperature, potential temperature, lapse-rate, pressure, zonal wind, meridional wind, and relative humidity.

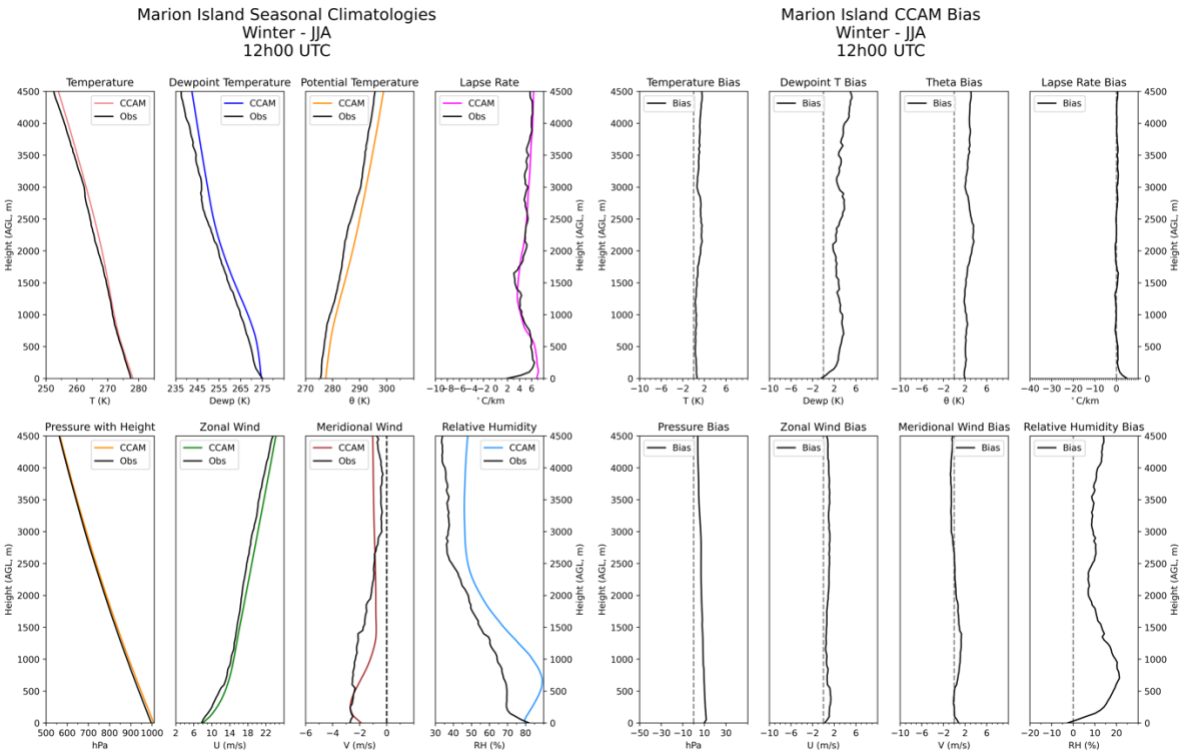

Figure 4.18: Marion Island 12h00 UTC austral winter seasonal mean CCAM and radiosonde vertical profiles, including the CCAM bias, of temperature, dewpoint temperature, potential temperature, lapse-rate, pressure, zonal wind, meridional wind, and relative humidity.

4.3.2.5. Climatology and seasonal variability of the ABLH for 00h00 and 12h00

The CCAM estimations indicate that the variability of the ABLH between 00h00 UTC and 12h00 UTC, and between the seasons is not as pronounced (see Figure 4.19). Radiosonde-based ABLH on the other hand indicates that this is only true for the spring and summer months, while winter 00h00 UTC has a capping inversion. As with the CCAM, radiosonde ABLH calculations indicate that the summer months of December, January and February, have the lowest seasonal mean values. The CCAM underestimates ABLH values for both 00h00 UTC and 12h00 UTC throughout the four seasons, except during winter at 00h00 UTC which indicates a positive bias by the CCAM (see Figure 4.20).

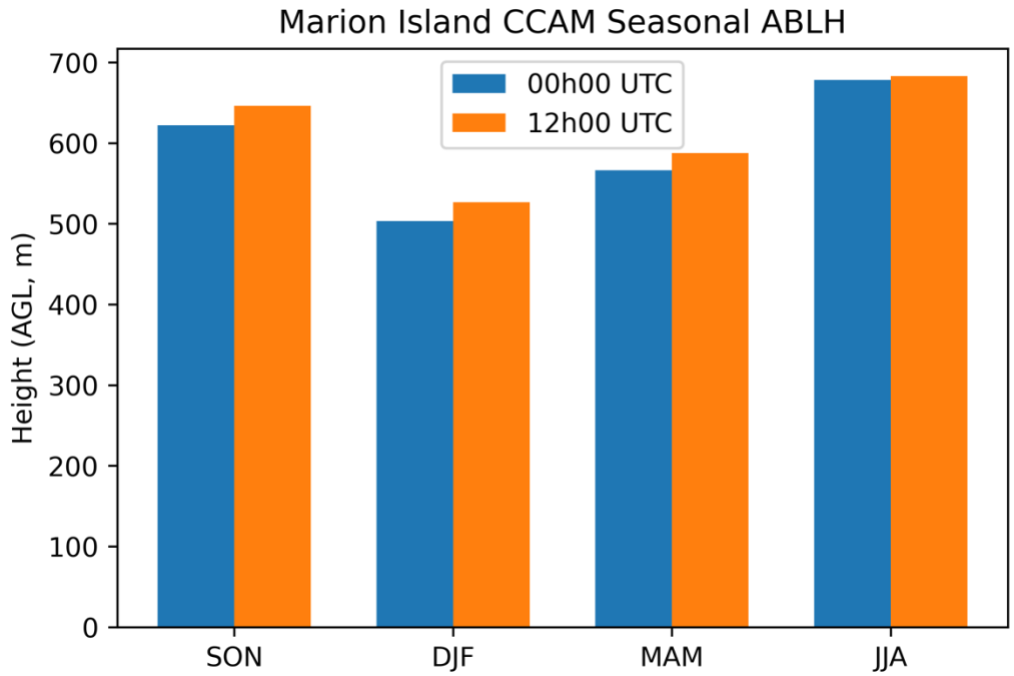

Figure 4.19: CCAM seasonal climatologies of the ABLH for 00h00 UTC (blue) and 12h00 UTC (orange) over Marion Island.

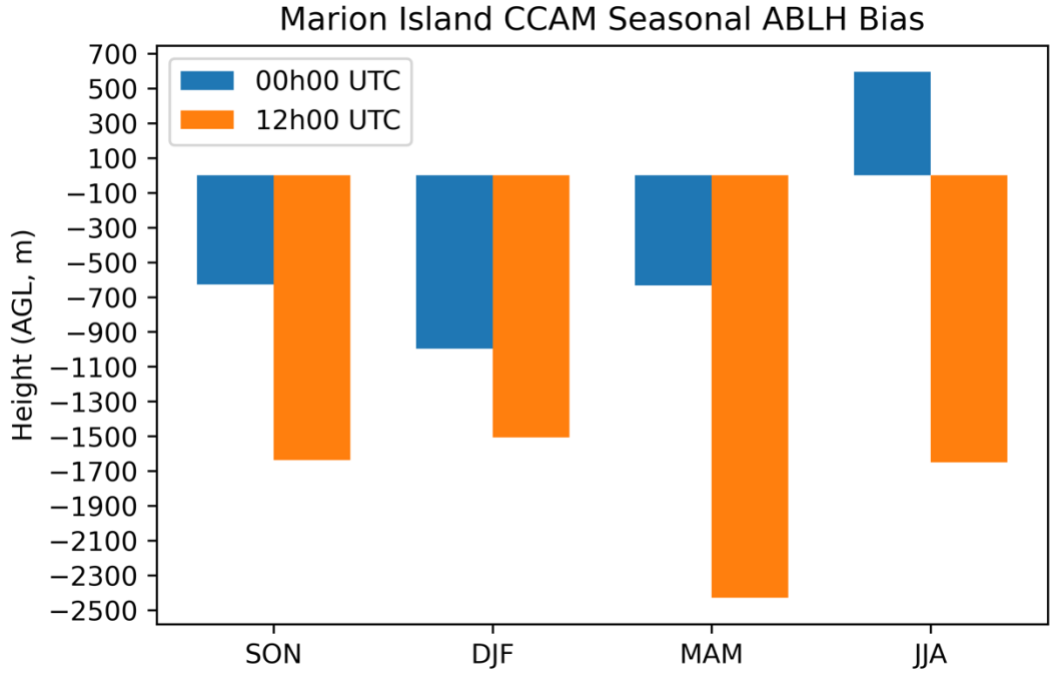

Figure 4.20: CCAM seasonal bias of the ABLH for 00h00 UTC (blue) and 12h00 UTC (orange) over Marion Island.

4.3.3. Syowa Station

4.3.3.1. The SON season and bias for 00h00 and 12h00

Analysis over Syowa during the spring months of September, October and November, for both 00h00 UTC and 12h00 UTC (see Figure 4.21 and Figure 4.22), indicates that there is positive bias throughout the lower troposphere for potential temperature, zonal wind and meridional wind. There is also negative bias for pressure. Relative humidity continues to indicate bias by the CCAM. However, unlike over Irene and Marion Island station, the relative humidity bias over Syowa during spring months is negative near the surface, and positive in the remaining two-thirds of the lower troposphere. This indicates that there is dry bias by the CCAM near the surface over Syowa during this season.

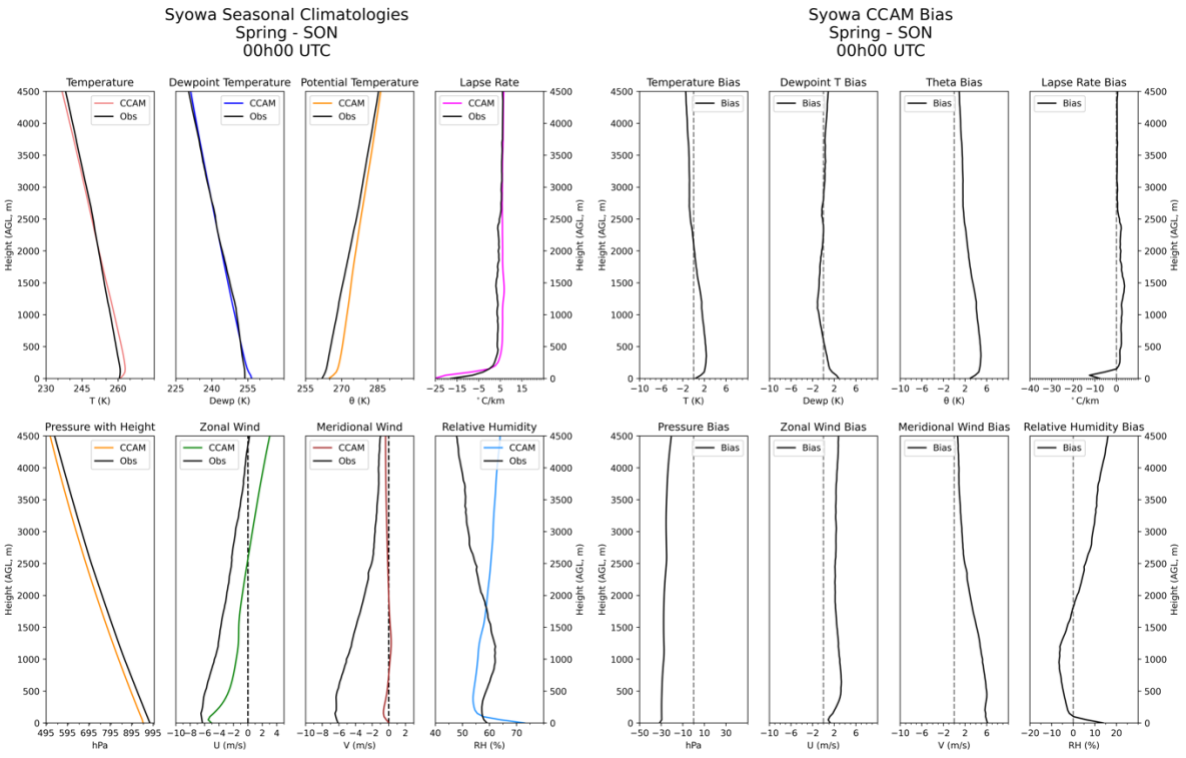

Figure 4.21: Syowa 00h00 UTC austral spring seasonal mean CCAM and radiosonde vertical profiles, including the CCAM bias, of temperature, dewpoint temperature, potential temperature, lapse-rate, pressure, zonal wind, meridional wind, and relative humidity.

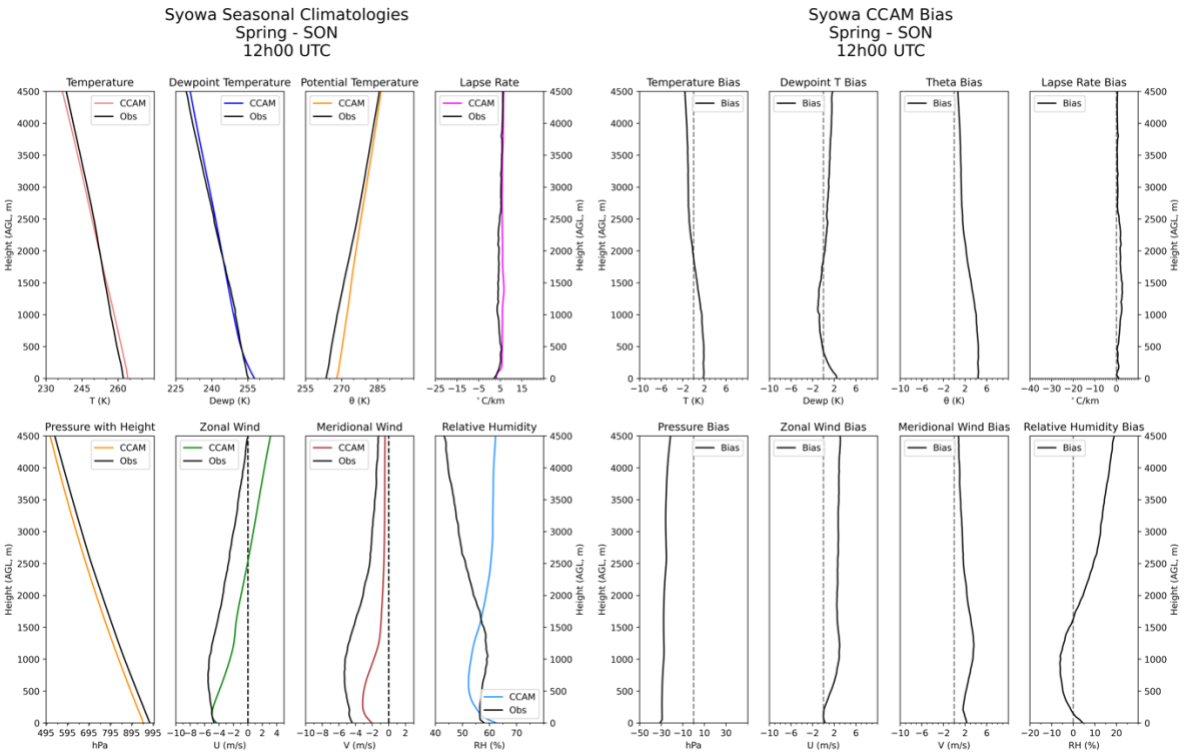

Figure 4.22: Syowa 12h00 UTC austral spring seasonal mean CCAM and radiosonde vertical profiles, including the CCAM bias, of temperature, dewpoint temperature, potential temperature, lapse-rate, pressure, zonal wind, meridional wind, and relative humidity.

4.3.3.2. The DJF season and bias for 00h00 and 12h00

During the summer months of December, January and February, the depiction of temperature, dewpoint temperature, and temperature lapse-rate by CCAM is similar to observations (see Figure 4.23 and Figure 2.24). CCAM continues to be negatively biased in representing pressure. There is also positive bias for potential temperature, zonal wind and meridional wind. It is interesting to now note that the relative humidity bias has shifted towards the surface, while values between 1000 m and 1500 m are almost similar to observations.

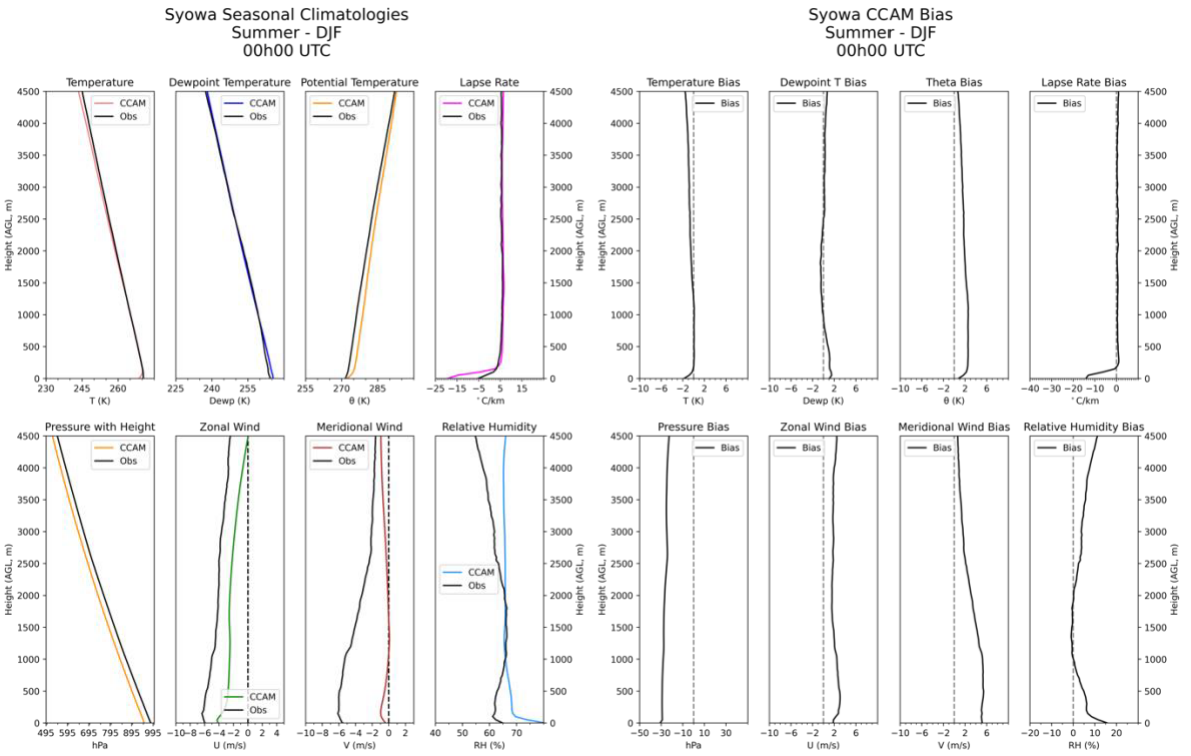

Figure 4.23: Syowa 00h00 UTC austral summer seasonal mean CCAM and radiosonde vertical profiles, including the CCAM bias, of temperature, dewpoint temperature, potential temperature, lapse-rate, pressure, zonal wind, meridional wind, and relative humidity.

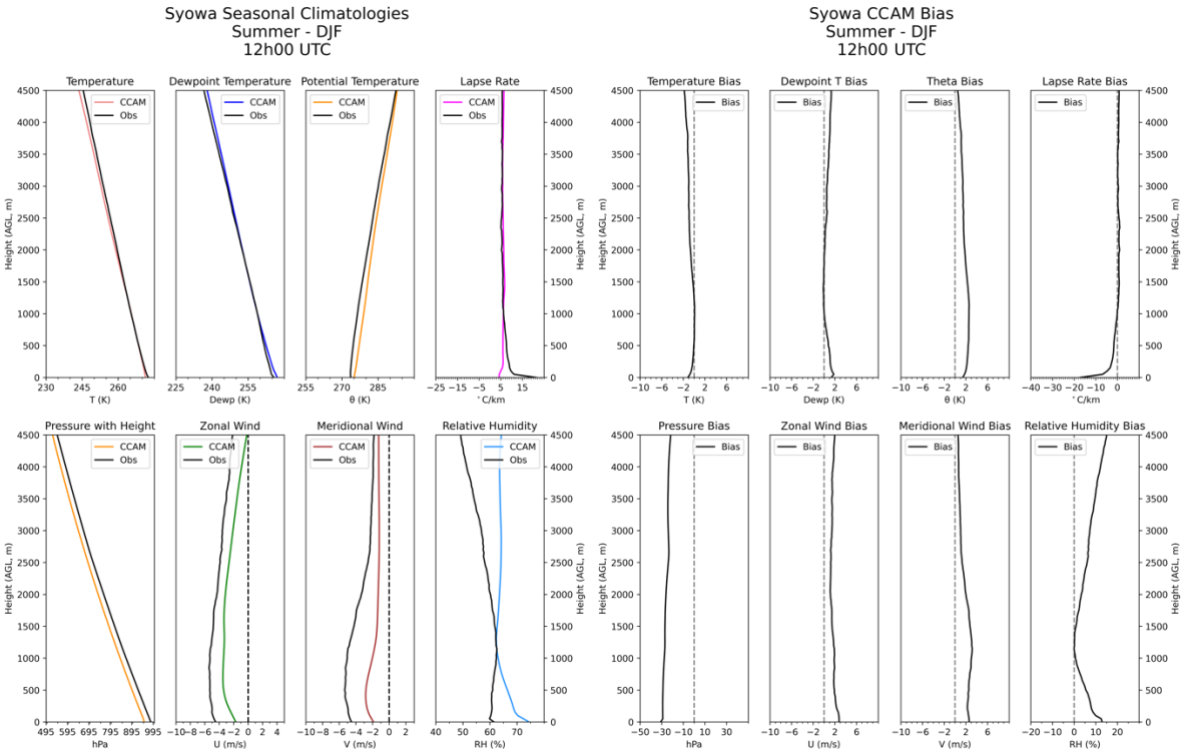

Figure 4.24: Syowa 12h00 UTC austral summer seasonal mean CCAM and radiosonde vertical profiles, including the CCAM bias, of temperature, dewpoint temperature, potential temperature, lapse-rate, pressure, zonal wind, meridional wind, and relative humidity.

4.3.3.3. The MAM season and bias for 00h00 and 12h00

During the Autumn months of March, April and May, at both 00h00 UTC and 12h00 UTC (see Figure 4.25 and Figure 4.26), the CCAM seems to struggle to represent zonal wind, meridional wind, and potential temperature, with all three being positively biased especially near the surface in the CCAM. The negative bias can also be seen for dewpoint temperature, and pressure. Relative humidity is as biased as with the other seasons.

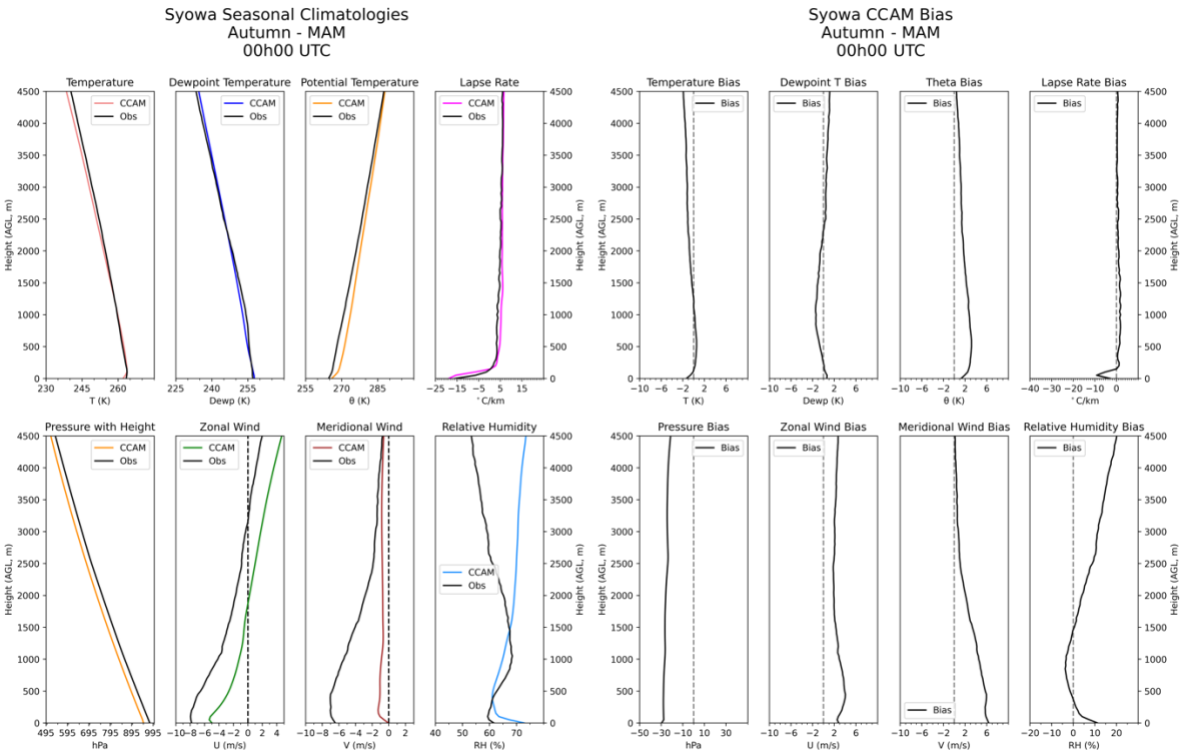

Figure 4.25: Syowa 00h00 UTC austral autumn seasonal mean CCAM and radiosonde vertical profiles, including the CCAM bias, of temperature, dewpoint temperature, potential temperature, lapse-rate, pressure, zonal wind, meridional wind, and relative humidity.

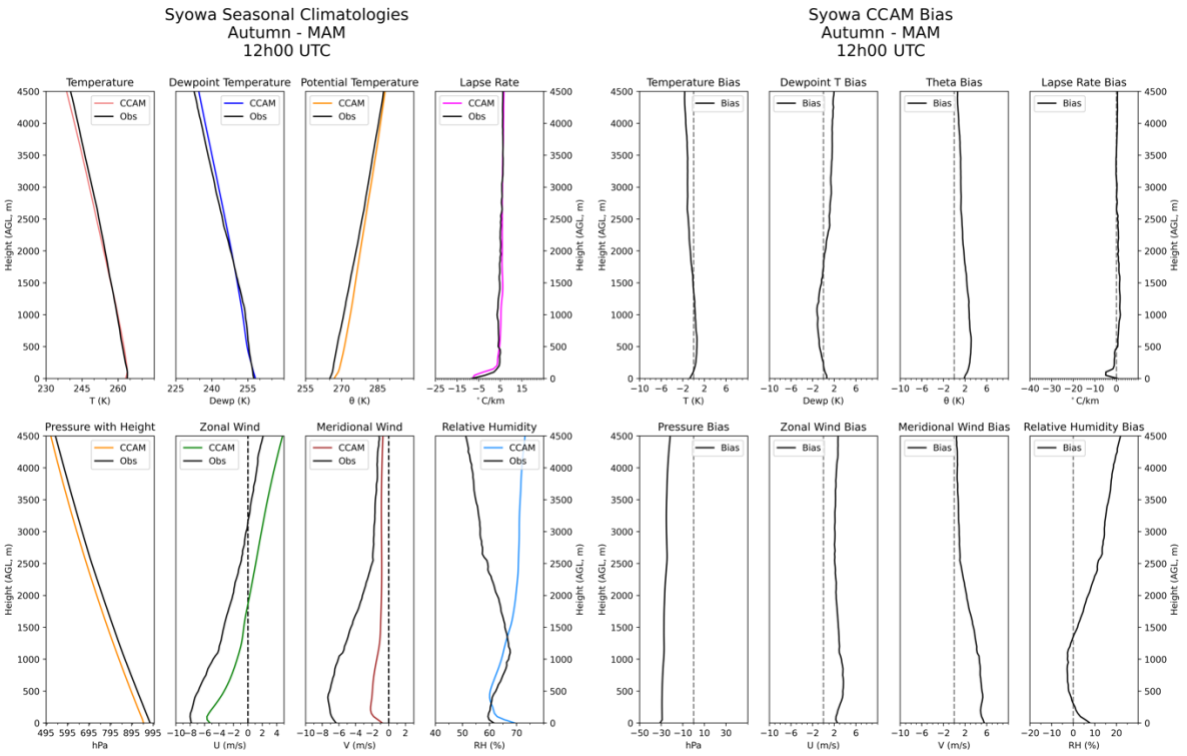

Figure 4.26: Syowa 12h00 UTC austral autumn seasonal mean CCAM and radiosonde vertical profiles, including the CCAM bias, of temperature, dewpoint temperature, potential temperature, lapse-rate, pressure, zonal wind, meridional wind, and relative humidity.

4.3.3.4. The JJA season and bias for 00h00 and 12h00

During the winter months of June, July and August, at both 00h00 UTC and 12h00 UTC (see Figure 4.27 and Figure 4.28), the CCAM continues to be negatively biased when it comes to representing dewpoint temperature, pressure and relative humidity. Positive biases were detected for potential temperature, zonal wind, and meridional wind. Relative humidity is negatively biased near the surface and positively biased from the mid-lower troposphere.

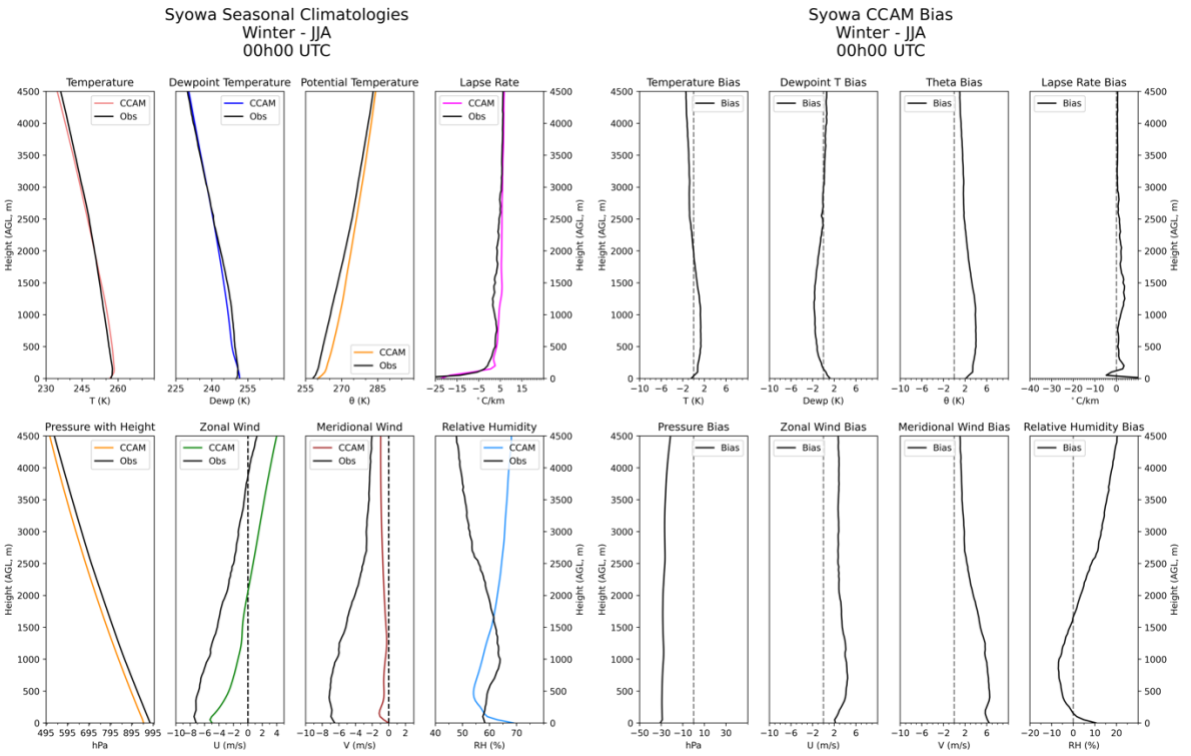

Figure 4.27: Syowa 00h00 UTC austral winter seasonal mean CCAM and radiosonde vertical profiles, including the CCAM bias, of temperature, dewpoint temperature, potential temperature, lapse-rate, pressure, zonal wind, meridional wind, and relative humidity.

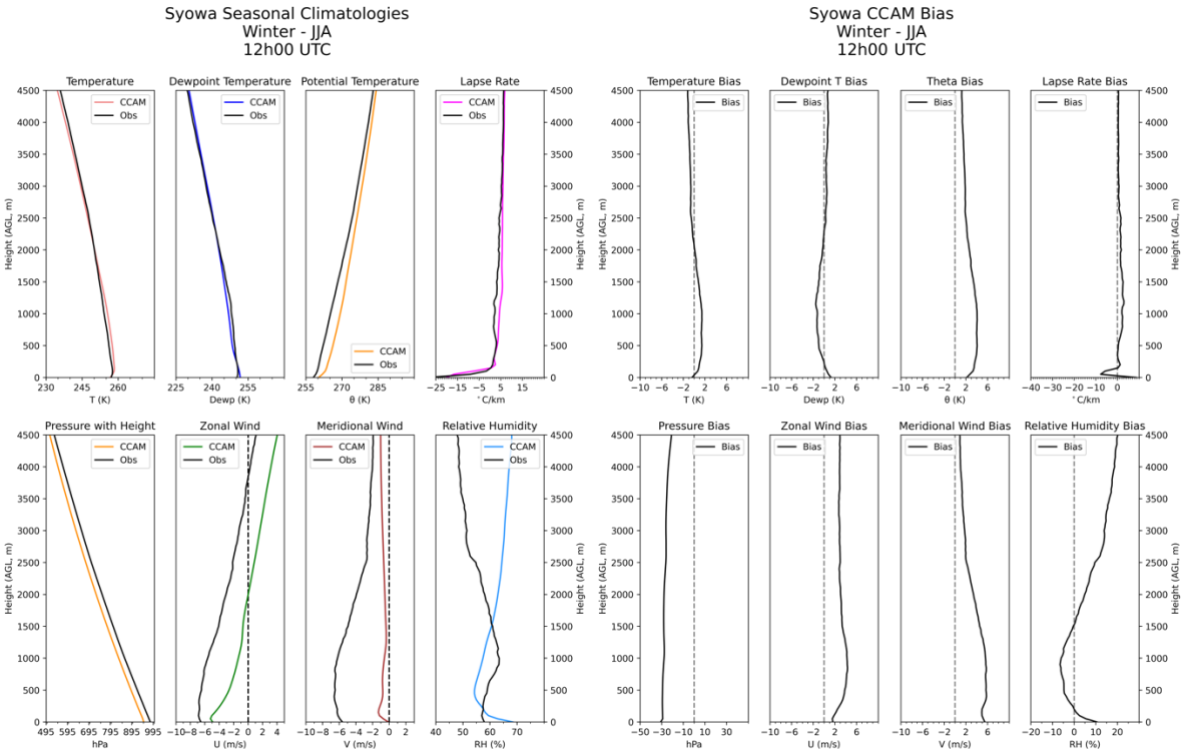

Figure 4.28: Syowa 12h00 UTC austral winter seasonal mean CCAM and radiosonde vertical profiles, including the CCAM bias, of temperature, dewpoint temperature, potential temperature, lapse-rate, pressure, zonal wind, meridional wind, and relative humidity.

4.3.3.5. Climatology and seasonal variability of the ABLH for 00h00 and 12h00

The CCAM values over Syowa indicates shallow ABLH, which are comparable with the calculated ones from radiosonde observation (see Figure 4.29 and Figure 4.30). This is especially true for 00h00 UTC values. The summer and winter months also indicate almost similar values at 12h00 UTC, while the spring and autumn months indicate negative bias by the CCAM. This is because the radiosonde data did not indicate surface-based inversion for those months, on a seasonal time-scale.

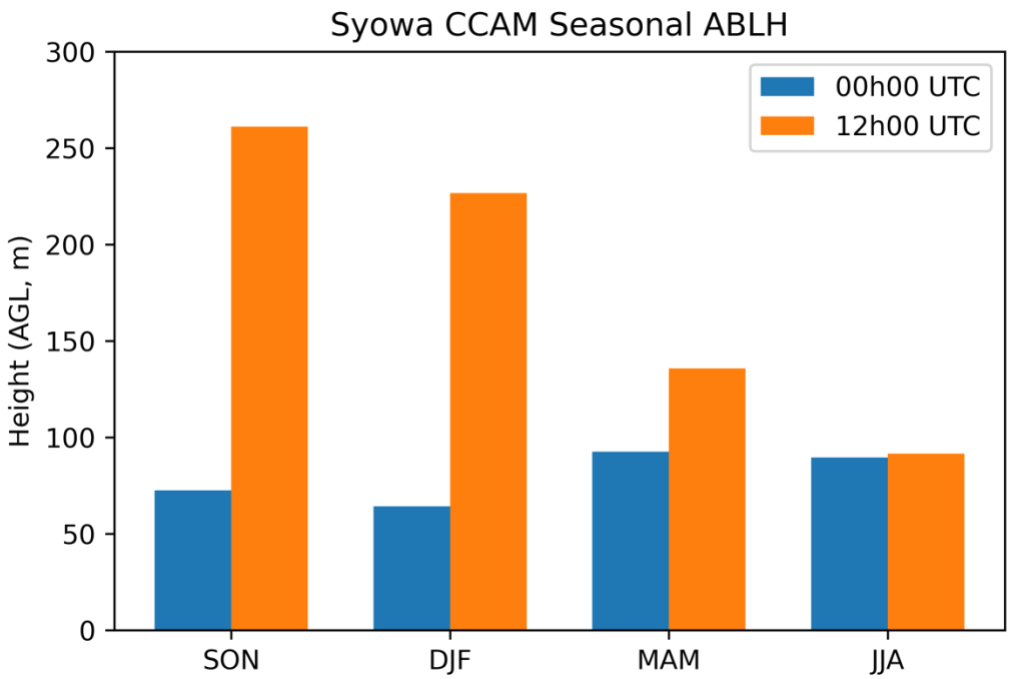

Figure 4.29: CCAM seasonal climatologies of the ABLH for 00h00 UTC (blue) and 12h00 UTC (orange) over Syowa.

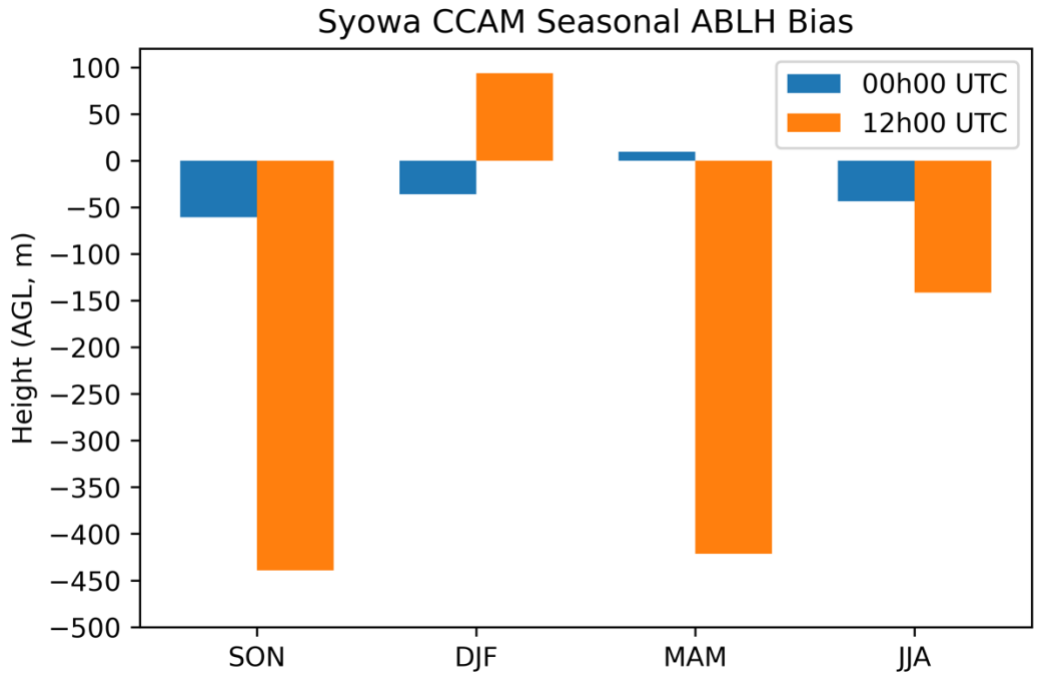

Figure 4.30: CCAM seasonal bias of the ABLH for 00h00 UTC (blue) and 12h00 UTC (orange) over Syowa.

4.4. SUMMARY OF THE RESULTS

The CCAM model data analysed and evaluated in this study has the following meteorological parameters: temperature, dewpoint temperature, potential temperature, pressure, zonal wind, meridional wind, relative humidity, and ABLH, for both 00h00 UTC and 12h00 UTC. We analysed how these meteorological parameters depict boundary layer attributes, over the four seasons of spring, summer, autumn and winter. We also looked at how they compare with observations.

It was found that over Irene, the CCAM model performs relatively well in depicting the fields of potential temperature, temperature lapse-rates, and the meridional wind, albeit with bias near the surface. This excludes potential temperature during spring at 12h00 UTC which is positively biased throughout the lower troposphere, while the biases of temperature and zonal wind varies with each season. It was also found that pressure is positively biased throughout the depth of the lower troposphere at both 00h00 UTC and 12h00 UTC hours.

It is interesting to note the similar pattern of persistent positive bias of moisture variables – dewpoint temperature and relative humidity. This is especially true for the spring and summer months over Irene, while autumn and winter months indicate pronounced negative bias near

the surface. Over Marion Island the positive bias of relative humidity is even more pronounced and persists through the four seasons at both 00h00 UTC and 12h00 UTC hours. This may be an indicator that the CCAM model is too moist above the surface over the two stations. Alternatively, if the LLJ hypothesis proposed in our observational analysis is true, then the CCAM may be overestimating the strength of it as also shown by the positive biases of the zonal and meridional winds during the same seasons and times. Other previous studies also found that various climate models widely used across the world, tend to have a warm bias near the surface over the Southern Ocean (Hyder et al. 2018). Some have consequently also been found to be too moist, as in my study. Performing further model sensitivity experiments with different boundary layer parameterisations (future work) would help in understanding the main sources of this bias.

On the contrary, over Syowa, there is an inverse of the bias pattern which indicates negative bias near the surface for the three seasons of spring, autumn and winter, while the summer season indicate positive bias near the surface and above the almost similar pattern in the mid-lower troposphere. This may indicate that the CCAM is too dry over Syowa during the indicated three seasons. The problem of global climate models being either too dry or too moist is known. For example, an analysis of temperature and humidity biases in global climate models by John and Soden (2007) found that on average, commonly used climate models simulated a large moist bias in the free troposphere while a dry bias was found to be present in the boundary layer.

CHAPTER 5: SUMMARY AND CONCLUSION

This research focused on the ABL, a part of the atmosphere humans spend most of their lives in contact with. The ABL plays an important role in the climate system as it helps to regulate the energy exchange between the various Earth surfaces and the atmosphere (Baede et al. 2001). Many different ABL parameterisation schemes are used by atmospheric models. However, in order to use a correct parameterisation scheme, there first need to be a recognition of the closure problem resulting from the turbulent nature of the mixing within the ABL (Holt and Raman 1988).

In this research project we undertake to evaluate simulations of Southern Hemispheric boundary layers by the CCAM global atmospheric model. To do this, we firstly determined a climatology of present-day ABL attributes from atmospheric soundings across three regions with vastly different climates in the Southern Hemisphere – viz: Irene in South Africa (subtropical continent), Marion Island in the mid-latitude,

and Syowa in the Southern Ocean (high-latitude). After determining the climatological attributes from radiosonde data, we secondly evaluated how the atmospheric model, CCAM, simulates attributes of the ABL climatology over the mentioned locations.

5.1. CLIMATOLOGICAL ANALYSIS FROM THE RADIOSONDE OBSERVATIONS

Data from each radiosonde measurement was quality controlled using criteria adapted from Seidel et al. (2010) and Sivaraman et al. (2013). The radiosonde data that passed the quality control were then vertically interpolated, linearly, to standard height levels before being used in climatological computations and seasonal variability analysis. The vertical linear interpolation algorithm used in this study determined the values of parameters corresponding to height values, which have been fixed from the surface up to 5000 m into the atmosphere. This was done at an interval of 50 m.

Our climatological analysis of the radiosonde data indicates that there persistently exists a temperature inversion over Irene at 00h00 UTC throughout all the months of the year. This inversion is more intense during the autumn and winter seasons, while it is not as pronounced during the spring and summer seasons. This agrees well with findings by Tyson et al. (1976), who also used radiosonde data to characterise temperature inversions in South Africa. Our results also affirm that of Tyson et al. (1976) in that they show that the environmental lapse rates correlate well with temperature inversions, with the autumn and winter months recording highly negative lapse-rates near the surface compared to the spring and summer seasons.

The radiosonde data analysis over Syowa also indicates the presence of surface-based inversion at 00h00 UTC for all the months of the year. The surface-based inversion was also observed for 12h00 during all the months except the summer months, May, October and November. This is expected as the Antarctic ABL is known to be frequented by surface-based inversions and has been found that this feature is stronger, deeper and frequent during the autumn and winter months (Zhang et al. 2011).

It was also found that monthly variability within the different seasons are prominently observed during the transitional seasons of autumn and spring, especially for thermodynamic variables. An interesting feature which was also observed over Irene and Syowa throughout all the seasons is a bulge in relative humidity above the surface. For Irene this is true for all the months of the year at 12h00 UTC, while for Syowa this bulge is observed for both 00h00 UTC and 12h00 UTC for all the month of the year. It is currently not known why this bulge exists, but we hypothesise that it is due to the presence of low-level jet (LLJ) (see Gimeno et al. 2016).

5.2. CLIMATOLOGICAL ANALYSIS FROM THE CCAM AND BIAS

The CCAM model data analysed and evaluated in this study has the following meteorological parameters: temperature, dewpoint temperature, potential temperature, pressure, zonal wind, meridional wind, relative humidity, and ABLH, for both 00h00 UTC and 12h00 UTC. We analysed how these meteorological parameters depict boundary layer attributes, over the four seasons of spring, summer, autumn and winter. We also looked at how they compare with observations.

It was found that over Irene, the CCAM model performs relatively well in depicting the fields of potential temperature, temperature lapse-rates, and the meridional wind, albeit with bias near the surface. This excludes potential temperature during spring at 12h00 UTC which is positively biased throughout the lower troposphere, while the biases of temperature and zonal wind varies with each season. It was also found that pressure is positively biased throughout the depth of the lower troposphere at both 00h00 UTC and 12h00 UTC hours.

It is interesting to note the similar pattern of persistent positive bias of moisture variables – dewpoint temperature and relative humidity. This is especially true for the spring and summer months over Irene, while autumn and winter months indicate pronounced negative bias near the surface. Over Marion Island the positive bias of relative humidity is even more pronounced and persists through our the four seasons at both 00h00 UTC and 12h00 UTC hours. This may be an indicator that the CCAM model is too moist above the surface over the two stations. Alternatively, if the LLJ hypothesis proposed in our observational analysis is true, then the CCAM may be overestimating the strength of it as also shown by the positive biases of the zonal and meridional winds during the same seasons and times.

On the contrary, over Syowa, there is an inverse of the bias pattern which indicates negative bias near the surface for the three seasons of spring, autumn and winter, while the summer season indicate positive bias near the surface and above the almost similar pattern in the mid-lower troposphere. This may indicate that the CCAM is too dry over Syowa during the indicated three seasons. The problem of global climate models being either too dry or too moist is known. For example, an analysis of temperature and humidity biases in global climate models by John and Soden (2007) found that on average, commonly used climate models simulated a large moist bias in the free troposphere while a dry bias was found to be present in the boundary layer.

5.3. A COMPARISON OF BOUNDARY LAYER HEIGHTS FROM SIMULATIONS AND OBSERVATIONS

To determine the ABLH from the interpolated radiosondes data we followed a well-established and widely used method, which defines the ABLH as the level of the maximum vertical gradient of potential temperature (Oke 1988, Stull 1988, Sorbjan 1989, Garratt 1992). However, there were two exceptions to this definition of the ABLH in our study. The first exception was when there exists a temperature inversion which is a clear indicator of a stable boundary layer immediately above the surface, with the top of it taken to represent the ABLH (Bradley et al. 1993). The second exception was when the bottom of the boundary layer was convective – that is when the potential temperature decreased with height immediately above the surface. In that case we use the parcel method to define the ABLH, which is also well established (Seibert et al. 2000).

Irene ABLH values based on calculations from observations were lower than values simulated by the CCAM at 12h00 UTC throughout the four seasons, with an overestimation of more than 900 m during spring. On the contrary, the CCAM underestimated ABLH values at 00h00 UTC for all the four seasons over Irene, with differences being only as much as 210 m for the winter season. The differences can be attributed to either the ABLH determination methods used, or the CCAM determination methods. Regardless, it is well-known that the method based on the potential temperature gradient tends to overestimate the boundary layer height (e.g. Seidel et al. 2010).

Over Marion Island, the CCAM consistently underestimated values of the ABLH for both 00h00 UTC and 12h00 UTC. An exception occurred at 00h00 UTC during the winter season, which indicates an overestimation of the ABLH by 550 m. Over Syowa, the differences between modelled and observed ABLH are not as pronounced as in both Irene and Marion Island. The smaller differences can be attributed to the presence of the surface-based inversion, which both the radiosonde and the CCAM can fairly well depict over Syowa.

5.4. RECOMMENDATIONS AND FUTURE WORK

Our study shows that the CCAM can simulate structures of the ABL with some skill, however, there are shortcomings in the simulations. We recommend that for future studies, the CCAM be tested with other types of ABL schemes and with more levels in the vertical. Further, some previous studies have shown that the simulated ABL changes with the model's horizontal

resolution. We recommend that further studies consider the performance of CCAM in simulating the ABL with different horizontal resolutions.

The next step of the research includes publishing the results in a journal. We also plan to build and expand on the spatial scale of these results. This will also include running the CCAM at 150 vertical levels and high resolution of about 4 km in the horizontal (and the grey-zone), as we get access to more computational capacity — with different boundary layer schemes.

LIST OF REFERENCES

Abdella, K., & Mcfarlane, N. (1997). A new second-order turbulence closure scheme for the planetary boundary layer. Journal of the Atmospheric Sciences, 54(14), 1850–1867. https://doi.org/10.1175/1520-0469(1997)054<1850:ANSOTC>2.0.CO;2

Allen, J. T. (2018). Climate Change and Severe Thunderstorms. In Oxford Research Encyclopedia of Climate Science (Issue June). https://doi.org/10.1093/acrefore/9780190228620.013.62

Anderson, J. D. (2005). Ludwig Prandtl's boundary layer. Physics Today, 58(12), 42–48. https://doi.org/10.1063/1.2169443

Andrews, D. G. (2010). An Introduction to Atmospheric Physics (2nd ed.). Cambridge University Press.

Antarctic Sea Ice Variability in the Southern Ocean-Climate System. (2017). In Antarctic Sea Ice Variability in the Southern Ocean-Climate System. https://doi.org/10.17226/24696

Baklanov, A. A., Grisogono, B., Bornstein, R., Mahrt, L., Zilitinkevich, S. S., Taylor, P., Larsen, S. E., Rotach, M. W., & Fernando, H. J. S. (2011). The Nature, Theory, and Modeling of Atmospheric Planetary Boundary Layers. Bulletin of the American Meteorological Society, 92(2), 123–128. https://doi.org/10.1175/2010BAMS2797.1

Baklanov, A. A., Grisogono, B., Bornstein, R., Mahrt, L., Zilitinkevich, S. S., Taylor, P., Larsen, S. E., Rotach, M. W., & Fernando, H. J. S. (2011). The nature, theory, and modeling of atmospheric planetary boundary layers. Bulletin of the American Meteorological Society, 92(2), 123–128. https://doi.org/10.1175/2010BAMS2797.1

Banks, R. F., Tiana-Alsina, J., Baldasano, J. M., Rocadenbosch, F., Papayannis, A., Solomos, S., & Tzanis, C. G. (2016). Sensitivity of boundary-layer variables to PBL schemes in the WRF model based on surface meteorological observations, lidar, and radiosondes during the HygrA-CD campaign. Atmospheric Research, 176–177, 185–201. https://doi.org/10.1016/j.atmosres.2016.02.024

Bélair, S., Mailhot, J., Strapp, J. W., & Macpherson, J. I. (1999). An examination of local versus nonlocal aspects of a TKE-based boundary layer scheme in clear convective conditions. Journal of Applied Meteorology, 38(10), 1499–1518. https://doi.org/10.1175/1520-0450(1999)038<1499:AEOLVN>2.0.CO;2

Beljaars, A. (1992). The parametrization of the planetary boundary layer. Meteorological Training Course Lecture Series, May 1992, 1–57.

Beljaars, A. C. M. (1995). The parametrization of surface fluxes in large-scale models under free convection. Quarterly Journal of the Royal Meteorological Society, 121(522), 255–270. https://doi.org/10.1002/qj.49712152203

Beljaars, A. C. M., & Betts, A. K. (1992). Validation of the boundary layer representation in the ECMWF Model. In ECMWF Seminar Proceedings: Validation of Models over Europe: Vol. Vol. II (pp. 159–195).

Betts, A. K. (1992). FIFE atmospheric boundary layer budget methods. Journal of Geophysical Research, 97(D17). https://doi.org/10.1029/91jd03172

Blamey, R., & Reason, C. J. C. (2007). Relationships between Antarctic sea-ice and South African winter rainfall. Climate Research, 33(2), 183–193. https://doi.org/10.3354/cr033183

Bopape, M. J. M., Engelbrecht, F. A., Randall, D. A., & Landman, W. A. (2014). Simulations of an isolated two-dimensional thunderstorm: Sensitivity to cloud droplet size and the presence of graupel. Asia-Pacific Journal of Atmospheric Sciences, 50(2), 139–151. https://doi.org/10.1007/s13143-014-0003-z

Bopape, M. J. M., Engelbrecht, F., Abiodun, B., Beraki, A., Ndarana, T., Ntsangwane, L., Sithole, H., Sovara, M., & Witi, J. (2019). Programme for the development of weather and climate numerical modelling systems in South Africa. South African Journal of Science, 115(5–6), 8–11. https://doi.org/10.17159/sajs.2019/5779

Bopape, M. J. M., Sithole, H. M., Motshegwa, T., Rakate, E., Engelbrecht, F., Archer, E., Morgan, A., Ndimeni, L., & Botai, J. (2019). A regional project in support of the SADC cyber-infrastructure framework implementation: Weather and climate. Data Science Journal, 18(1), 1–10. https://doi.org/10.5334/dsj-2019-034

Boutle, I. A., Eyre, J. E. J., & Lock, A. P. (2014). Seamless stratocumulus simulation across the turbulent gray zone. Monthly Weather Review, 142(4), 1655–1668. https://doi.org/10.1175/MWR-D-13-00229.1

Bracegirdle, T. J., Bertler, N. A. N., Carleton, A. M., Ding, Q., Fogwill, C. J., Fyfe, J. C., Hellmer, H. H., Karpechko, A. Y., Kusahara, K., Larour, E., Mayewski, P. A., Meier, W. N., Polvani, L. M., Russell, J. L., Stevenson, S. L., Turner, J., Van Wessem, J. M., Van De Berg, W. J., & Wainer, I. (2016). A multidisciplinary perspective on climate model evaluation for antarctica. Bulletin of the American Meteorological Society, 97(2), ES23– ES26. https://doi.org/10.1175/BAMS-D-15-00108.1

Bracegirdle, T. J., Shuckburgh, E., Sallee, J. B., Wang, Z., Meijers, A. J. S., Bruneau, N., Phillips, T., & Wilcox, L. J. (2013). Assessment of surface winds over the atlantic, indian, and pacific ocean sectors of the southern ocean in cmip5 models: Historical bias, forcing response, and state dependence. Journal of Geophysical Research Atmospheres, 118(2), 547–562. https://doi.org/10.1002/jgrd.50153

Brown, A. R., Beare, R. J., Edwards, J. M., Lock, A. P., Keogh, S. J., Milton, S. F., Walters, D. N., & Office, M. (2006). Upgrades to the boundary layer scheme in the Met Office NWP model. December, 1–31.

Bush, M., Allen, T., Bain, C., Boutle, I., Edwards, J., Finnenkoetter, A., Franklin, C., Hanley, K., Lean, H., Lock, A., Manners, J., Mittermaier, M., Morcrette, C., North, R., Petch, J., Short, C., Vosper, S., Walters, D., Webster, S., … Zerroukat, M. (2020). The first Met Office Unified Model-JULES Regional Atmosphere and Land configuration, RAL1.

Cheng-Ying, D., Zhi-Qiu, G., Qing, W., & Gang, C. (2011). Analysis of Atmospheric Boundary Layer Height Characteristics over the Arctic Ocean Using the Aircraft and GPS Soundings. Atmospheric and Oceanic Science Letters, 4(2), 124–130. https://doi.org/10.1080/16742834.2011.11446916

Chenoli, S. N., Ahmad Mazuki, M. Y., Turner, J., & Samah, A. A. (2017). Historical and projected changes in the Southern Hemisphere Sub-tropical Jet during winter from the CMIP5 models. In Climate Dynamics (Vol. 48, Issues 1–2). https://doi.org/10.1007/s00382-016-3102-y

Clark, P., Roberts, N., Lean, H., Ballard, S. P., & Charlton-Perez, C. (2016). Convection- permitting models: A step-change in rainfall forecasting. Meteorological Applications, 23(2), 165–181. https://doi.org/10.1002/met.1538

Dang, R., Li, H., Liu, Z., & Yang, Y. (2016). Statistical Analysis of Relationship between Daytime Lidar-Derived Planetary Boundary Layer Height and Relevant Atmospheric Variables in the Semiarid Region in Northwest China. Advances in Meteorology, 2016. https://doi.org/10.1155/2016/5375918

Díaz-Isaac, L., Lauvaux, T., & Davis, K. (2018). Impact of physical parameterizations and initial conditions on simulated atmospheric transport and CO2 mole fractions in the US Midwest. Atmospheric Chemistry and Physics, 18(20), 14813–14835. https://doi.org/10.5194/acp-18-14813-2018

Edwards, J. M., Beare, R. J., & Lapworth, A. J. (2006). Simulation of the observed evening transition and nocturnal boundary layers: Single-column modelling. Quarterly Journal of the Royal Meteorological Society, 132(614), 61–80. https://doi.org/10.1256/qj.05.63

Engelbrecht, C. J., Engelbrecht, F. A., & Dyson, L. L. (2013). High-resolution model-projected changes in mid-tropospheric closed-lows and extreme rainfall events over southern Africa. International Journal of Climatology, 33(1), 173–187. https://doi.org/10.1002/joc.3420

Engelbrecht, F. A., McGregor, J. L., & Rautenbach, C. J. D. W. (2007). On the development of a new nonhydrostatic atmospheric model in South Africa. South African Journal of Science, 103(3–4), 127–134.

Eresmaa, N., Härkönen, J., Joffre, S. M., Schultz, D. M., Karppinen, A., & Kukkonen, J. (2012). A three-step method for estimating the mixing height using ceilometer data from the Helsinki testbed. Journal of Applied Meteorology and Climatology, 51(12), 2172– 2187. https://doi.org/10.1175/JAMC-D-12-058.1

Eyring, V., Bony, S., Meehl, G. A., Senior, C. A., Stevens, B., Stouffer, R. J., & Taylor, K. E. (2016). Overview of the Coupled Model Intercomparison Project Phase 6 (CMIP6) experimental design and organization. Geoscientific Model Development, 9(5), 1937– 1958. https://doi.org/10.5194/gmd-9-1937-2016

Eyring, V., Gleckler, P. J., Heinze, C., Stouffer, R. J., Taylor, K. E., Balaji, V., Guilyardi, E., Joussaume, S., Kindermann, S., Lawrence, B. N., Meehl, G. A., Righi, M., & Williams, D. N. (2016). Towards improved and more routine Earth system model evaluation in CMIP. Earth System Dynamics, 7(4), 813–830. https://doi.org/10.5194/esd-7-813-2016

Feng, L., Smith, S., Braun, C., Crippa, M., Gidden, M., Hoesly, R., Klimont, Z., van Marle, M., van den Berg, M., & van der Werf, G. (2019). Gridded Emissions for CMIP6.

Fletcher, J. K., Bretherton, C. S., Xiao, H., Sun, R., & Han, J. (2014). Improving subtropical boundary layer cloudiness in the 2011 NCEP GFS. Geoscientific Model Development, 7(5), 2107–2120. https://doi.org/10.5194/gmd-7-2107-2014

Garratt, J. R. (1994). Review: the atmospheric boundary layer. Earth Science Reviews, 37(1–2), 89–134. https://doi.org/10.1016/0012-8252(94)90026-4

Garratt, J. R., Hess, G. D., Physick, W. L., & Bougeault, P. (1996). The atmospheric boundary layer - advances in knowledge and application. Boundary-Layer Meteorology, 78(1–2), 9–37. https://doi.org/10.1007/BF00122485

Geernaert, G. L. (2003). BOUNDARY LAYERS | Surface Layer. Encyclopedia of Atmospheric Sciences, 1988, 305–311. https://doi.org/10.1016/b0-12-227090-8/00092-0

Gierens, R., & Connor, E. O. (2015). Understanding the evolution of the boundary layer over the Highveld , South Africa. 64(013613879).

Han, J., & Pan, H. L. (2011). Revision of convection and vertical diffusion schemes in the NCEP Global Forecast System. Weather and Forecasting, 26(4), 520–533. https://doi.org/10.1175/WAF-D-10-05038.1

Hanna, S. R. (1969). The thickness of the planetary boundary layer. Atmospheric Environment (1967), 3(5), 519–536. https://doi.org/10.1016/0004-6981(69)90042-0

Ho, M., Kiem, A. S., & Verdon-Kidd, D. C. (2012). The Southern Annular Mode: A comparison of indices. Hydrology and Earth System Sciences, 16(3), 967–982. https://doi.org/10.5194/hess-16-967-2012

Holt, T., & Raman, S. (1988). A review and comparative evaluation of multilevel boundary layer parameterizations for first-order and turbulent kinetic energy closure schemes. Reviews of Geophysics, 26(4), 761–780. https://doi.org/10.1029/RG026i004p00761

Holtslag, B. (2006). Preface: GEWEX Atmospheric Boundary-layer Study (GABLS) on Stable Boundary Layers. Boundary-Layer Meteorology, 118(2), 243–246. https://doi.org/10.1007/s10546-005-9008-6

Holzworth, G. C. (1964). Estimates of Mean Maximum Mixing Depths in the Contiguous United States. Monthly Weather Review, 92(5), 235–242. https://doi.org/10.1175/1520- 0493(1964)092<0235:eommmd>2.3.co;2

Hong, S.-Y., Choi, H.-J., Han, J.-Y., & Kwon, Y.-C. (2017). PBL and precipitation interaction and grey-zone issues. Workshop on Shedding Light on the Greyzone. https://www.ecmwf.int/node/17781

Honnert, R. (2019). Grey-Zone Turbulence in the Neutral Atmospheric Boundary Layer. Boundary-Layer Meteorology, 170(2), 191–204. https://doi.org/10.1007/s10546-018- 0394-y

Horowitz, H. M., Garland, R. M., Thatcher, M., Landman, W. A., Dedekind, Z., Van Der Merwe, J., & Engelbrecht, F. A. (2017). Evaluation of climate model aerosol seasonal and spatial variability over Africa using AERONET. Atmospheric Chemistry and Physics, 17(22), 13999–14023. https://doi.org/10.5194/acp-17-13999-2017

Horowitz, H., Garland, R., Thatcher, M., Landman, W., Dedekind, Z., van der Merwe, J., & Engelbrecht, F. (2017). Understanding the seasonality and climatology of aerosols in Africa through evaluation of CCAM aerosol simulations against AERONET measurements. Atmospheric Chemistry and Physics Discussions,

May, 1–38. https://doi.org/10.5194/acp-2017-250

Hu, X. M., Nielsen-Gammon, J. W., & Zhang, F. (2010). Evaluation of three planetary boundary layer schemes in the WRF model. Journal of Applied Meteorology and Climatology, 49(9), 1831–1844. https://doi.org/10.1175/2010JAMC2432.1

Hurley, P. (2007). Modelling mean and turbulence fields in the dry convective boundary layer with the eddy-diffusivity/mass-flux approach. Boundary-Layer Meteorology, 125(3), 525–536. https://doi.org/10.1007/s10546-007-9203-8

Hyder, P., Edwards, J., Allan, R.P., Hewitt, H.T., Bracegirdle, T.J., Gregory, J.M., Wood, R.A., Meijers, A.J.S., Mulcahy, J., Field, P., Furtado, K., Bodas-Salcedo, A., Williams, K.D., Copsey, D., Josey, S.A., Liu, C., Roberts, C.D., Sanchez, C., Ridley, J., Thorpe, L., Hardiman, S.C., Mayer, M., Berry, D.I., Belcher, S.E. (2018). Critical Southern Ocean climate model biases traced to atmospheric model cloud errors. Nat Commun 9, 3625. https://doi.org/10.1038/s41467-018-05634-2

Jahn, D. E., & Gallus, W. A. (2018). Impacts of modifications to a local planetary boundary layer scheme on forecasts of the Great Plains low-level jet environment. Weather and Forecasting, 33(5), 1109–1120. https://doi.org/10.1175/WAF-D-18-0036.1

Jeričević, A., Kraljević, L., Grisogono, B., Fagerli, H., & Večenaj, Ž. (2010). Parameterization of vertical diffusion and the atmospheric boundary layer height determination in the EMEP model. Atmospheric Chemistry and Physics, 10(2), 341–364. https://doi.org/10.5194/acp-10-341-2010

Kendon, E. J., Ban, N., Roberts, N. M., Fowler, H. J., Roberts, M. J., Chan, S. C., Evans, J. P., Fosser, G., & Wilkinson, J. M. (2017). Do convection-permitting regional climate models improve projections of future precipitation change? Bulletin of the American Meteorological Society, 98(1), 79–93. https://doi.org/10.1175/BAMS-D-15-0004.1

Kidson, J. W. (1999). Principal modes of Southern Hemisphere low-frequency variability obtained from NCEP-NCAR reanalyses. Journal of Climate, 12(9), 2808–2830. https://doi.org/10.1175/1520-0442(1999)012<2808:PMOSHL>2.0.CO;2

KoHler, M., Ahlgrimm, M., & Beljaars, A. (2011). Unified treatment of dry convective and stratocumulus-topped boundary layers in the ECMWF model. Quarterly Journal of the Royal Meteorological Society, 137(654), 43–57. https://doi.org/10.1002/qj.713

Korhonen, K., Giannakaki, E., Mielonen, T., Pfüller, A., Laakso, L., Vakkari, V., Baars, H., Engelmann, R., Beukes, J. P., Van Zyl, P. G., Ramandh, A., Ntsangwane, L., Josipovic, M., Tiitta, P., Fourie, G., Ngwana, I., Chiloane, K., & Komppula, M. (2014). Atmospheric boundary layer top height in South Africa: Measurements with lidar and radiosonde compared to three atmospheric models. Atmospheric Chemistry and Physics, 14(8), 4263–4278. https://doi.org/10.5194/acp-14-4263-2014

Krishnamurti, T. N., Basu, S., Sanjay, J., & Gnanaseelan, C. (2008). Evaluation of several different planetary boundary layer schemes within a single model, a unified model and a multimodel superensemble. Tellus, Series A: Dynamic Meteorology and Oceanography, 60 A(1), 42–61. https://doi.org/10.1111/j.1600-0870.2007.00278.x

Lemone, M. A., Angevine, W. M., Bretherton, C. S., Chen, F., Dudhia, J., Fedorovich, E., Katsaros, K. B., Lenschow, D. H., Mahrt, L., Patton, E. G., Sun, J., Tjernström, M., & Weil, J. (2018). 100 Years of Progress in Boundary Layer Meteorology. Meteorological Monographs, 59, 9.1-9.85. https://doi.org/10.1175/AMSMONOGRAPHS-D-18-0013.1

Liu, S., & Liang, X. Z. (2010). Observed diurnal cycle climatology of planetary boundary layer height. Journal of Climate, 23(21), 5790–5809. https://doi.org/10.1175/2010JCLI3552.1

Lock, A. (2011). Stable boundary layer modelling at the Met Office Operational models at the Met Office Stable boundary layer parametrization sensitivities. ECMWF GABLS Workshop, November, 7–10.

Lock, A. P. (2001). The numerical representation of entrainment in parameterizations of boundary layer turbulent mixing. Monthly Weather Review, 129(5), 1148–1163. https://doi.org/10.1175/1520-0493(2001)129<1148:TNROEI>2.0.CO;2

Lock, A. P., Brown, A. R., Bush, M. R., Martin, G. M., & Smith, R. N. B. (2000). A new boundary layer mixing scheme. Part I: Scheme description and single-column model tests. Monthly Weather Review, 128(9), 3187–3199. https://doi.org/10.1175/1520- 0493(2000)128<3187:ANBLMS>2.0.CO;2

Manatsa, D., Morioka, Y., Behera, S. K., Mushore, T. D., & Mugandani, R. (2015). Linking the southern annular mode to the diurnal temperature range shifts over southern Africa. International Journal of Climatology, 35(14), 4220–4236. https://doi.org/10.1002/joc.4281

Marshall, G. J. (2003). Trends in the Southern Annular Mode from observations and reanalyses. Journal of Climate, 16(24), 4134–4143. https://doi.org/10.1175/1520- 0442(2003)016<4134:TITSAM>2.0.CO;2

Martin, G. M., Bush, M. R., Brown, A. R., Lock, A. P., & Smith, R. N. B. (2000). A new boundary layer mixing scheme part II: Tests in climate and mesoscale models. Monthly Weather Review, 128(9), 3200–3217. https://doi.org/10.1175/1520- 0493(2000)128<3200:ANBLMS>2.0.CO;2

Mbokodo, I., Bopape, M. J., Chikoore, H., Engelbrecht, F., & Nethengwe, N. (2020). Heatwaves in the future warmer climate of South Africa. Atmosphere, 11(7), 0–18. https://doi.org/10.3390/atmos11070712

McGregor, J. L., & Dix, M. R. (2008). An updated description of the conformal-cubic atmospheric model. High Resolution Numerical Modelling of the Atmosphere and Ocean, 2001, 51–75. https://doi.org/10.1007/978-0-387-49791-4_4

McGregor, J., Katzfey, J., Thatcher, M., Hoffmann, P., & Nguyen, K. (2013). An Update on CCAM Modeling Activities at CSIRO. 30th Annual Conference of the South African Society for Atmospheric Science, June 2017, 51–53.

Moeng, C. H., Sullivan, P. P., Khairoutdinov, M. F., & Randall, D. A. (2010). A mixed scheme for subgrid-scale fluxes in cloud-resolving models. Journal of the Atmospheric Sciences, 67(11), 3692–3705. https://doi.org/10.1175/2010JAS3565.1

Nielsen-Gammon, J. W., Powell, C. L., Mahoney, M. J., Angevine, W. M., Senff, C., White, A., Berkowitz, C., Doran, C., & Knupp, K. (2008). Multisensor estimation of mixing heights over a coastal city. Journal of Applied Meteorology and

Climatology, 47(1), 27–43. https://doi.org/10.1175/2007JAMC1503.1

O'Neill, B. C., Tebaldi, C., Van Vuuren, D. P., Eyring, V., Friedlingstein, P., Hurtt, G., Knutti, R., Kriegler, E., Lamarque, J. F., Lowe, J., Meehl, G. A., Moss, R., Riahi, K., & Sanderson, B. M. (2016). The Scenario Model Intercomparison Project (ScenarioMIP) for CMIP6. Geoscientific Model Development, 9(9), 3461–3482. https://doi.org/10.5194/gmd-9-3461-2016

Office, M., Road, L., & Kingdom, U. (1996). Unified Model Documentation Paper No 24 Subsurface , Surface and Boundary Layer Processes. 24.

Onufrey, V., & Mohiuddin, M. (1985). Radiation therapy in the treatment of me tastatic renal cell carcinoma. International Journal of Radiation Oncology, Biology, Physics, 11(11), 2007–2009. https://doi.org/10.1016/0360-3016(85)90285-8

Parkinson, C. L. (2019). A 40-y record reveals gradual Antarctic sea ice increases followed by decreases at rates far exceeding the rates seen in the Arctic. Proceedings of the National Academy of Sciences of the United States of America, 116(29), 14414–14423. https://doi.org/10.1073/pnas.1906556116

Pascoe, C., Lawrence, B., Guilyardi, E., Juckes, M., & Taylor, K. (2019). Designing and Documenting Experiments in CMIP6. Geoscientific Model Development Discussions, June, 1–27. https://doi.org/10.5194/gmd-2019-98

Randall, D. A., Bitz, C. M., Danabasoglu, G., Denning, A. S., Gent, P. R., Gettelman, A., Griffies, S. M., Lynch, P., Morrison, H., Pincus, R., & Thuburn, J. (2019). 100 Years of Earth System Model Development. Meteorological Monographs, 59, 12.1-12.66. https://doi.org/10.1175/amsmonographs-d-18-0018.1

Redelsperger, J. L., Guichard, F., & Mondon, S. (2000). A parameterization of mesoscale enhancement of surface fluxes for large-scale models. Journal of Climate, 13(2), 402–421. https://doi.org/10.1175/1520-0442(2000)013<0402:APOMEO>2.0.CO;2

Roode, S. de, Siebesma, P., & Jonker, H. (2017). On the use of a TKE equation to compute subgrid fluxes in the "Grey Zone." Workshop on Shedding Light on the Greyzone. https://www.ecmwf.int/node/17784

Samuelsson, P. (2017). Land surface-atmosphere interaction approaching high resolution. Workshop on Shedding Light on the Greyzone. https://www.ecmwf.int/node/17800

Sánchez, E., Yagüe, C., & Gaertner, M. A. (2007). Planetary boundary layer energetics simulated from a regional climate model over Europe for present climate and climate change conditions. Geophysical Research Letters, 34(1), 1–6. https://doi.org/10.1029/2006GL028340

Schmid, P., & Niyogi, D. (2012). A method for estimating planetary boundary layer heights and its application over the ARM southern great plains site. Journal of Atmospheric and Oceanic Technology, 29(3), 316–322. https://doi.org/10.1175/JTECH-D-11-00118.1

Seidel, D. J., Ao, C. O., & Li, K. (2010). Estimating climatological planetary boundary layer heights from radiosonde observations: Comparison of methods and uncertainty analysis. Journal of Geophysical Research Atmospheres, 115(16), 1–15. https://doi.org/10.1029/2009JD013680

Seidel, D. J., Ao, C. O., & Li, K. (2010). Estimating climatological planetary boundary layer heights from radiosonde observations: Comparison of methods and uncertainty analysis. Journal of Geophysical Research Atmospheres, 115(16), 1–15. https://doi.org/10.1029/2009JD013680

Seidel, D. J., Zhang, Y., Beljaars, A., Golaz, J. C., Jacobson, A. R., & Medeiros, B. (2012). Climatology of the planetary boundary layer over the continental United States and Europe. Journal of Geophysical Research Atmospheres, 117(17), 1–15. https://doi.org/10.1029/2012JD018143

Smith, E. N., Gibbs, J. A., Fedorovich, E., & Klein, P. M. (2018). WRF model study of the Great Plains low-level jet: Effects of grid spacing and boundary layer parameterization. Journal of Applied Meteorology and Climatology, 57(10), 2375–2397. https://doi.org/10.1175/JAMC-D-17-0361.1

Smith, R. N. B. (1993). Experience and developments with the layer cloud and boundary layer mixing schemes in the UK Meteorological Office Unified Model. In Proc. ECMWF/GCSS workshop on parameterisation of the cloud-topped boundary layer.

Sokolov, A., Kicklighter, D., Schlosser, A., Wang, C., Monier, E., Brown-Steiner, B., Prinn, R., Forest, C., Gao, X., Libardoni, A., & Eastham, S. (2018). Description and Evaluation of the MIT Earth System Model (MESM). Journal of Advances in Modeling Earth Systems, 10(8), 1759–1789. https://doi.org/10.1029/2018MS001277

Stratton, R. A., Senior, C. A., Vosper, S. B., Folwell, S. S., Boutle, I. A., Earnshaw, P. D., Kendon, E., Lock, A. P., Malcolm, A., Manners, J., Morcrette, C. J., Short, C., Stirling, A. J., Taylor, C. M., Tucker, S., Webster, S., & Wilkinson, J. M. (2018). A Pan-African convection-permitting regional climate simulation with the met office unified model: CP4-Africa. Journal of Climate, 31(9), 3485–3508. https://doi.org/10.1175/JCLI-D-17- 0503.1

Stull, R. B. (1988). An introduction to boundary layer meteorology. An Introduction to Boundary Layer Meteorology. https://doi.org/10.1007/978-94-009-3027-8

Stull, R. B. (1988). Turbulence Closure Techniques. An Introduction to Boundary Layer Meteorology, 197–250. https://doi.org/10.1007/978-94-009-3027-8_6

Subrahamanyam, D. B., Gultepe, I., Al-Yahyai, S., & Satyanarayana, A. N. V. (2015). Atmospheric boundary-layer processes and atmospheric modeling. Advances in Meteorology, 2015, 2–4. https://doi.org/10.1155/2015/985353

Sušelj, K., Teixeira, J., & Chung, D. (2013). A unified model for moist convective boundary layers based on a stochastic eddy-diffusivity/mass-flux parameterization. Journal of the Atmospheric Sciences, 70(7), 1929–1953. https://doi.org/10.1175/JAS-D-12-0106.1

Sušelj, K., Teixeira, J., & Kurowski, M. (2017). From small-scale turbulence to large-scale convection: a unified scale-adaptive EDMF parameterization. Workshop on Shedding Light on the Greyzone. https://www.ecmwf.int/node/17783

Swart, N. C., Gille, S. T., Fyfe, J. C., & Gillett, N. P. (2018). Recent Southern Ocean warming and freshening driven by greenhouse gas emissions and ozone depletion. Nature Geoscience, 11(11), 836–841. https://doi.org/10.1038/s41561-018-0226-1

Swart, S., Gille, S. T., Delille, B., Josey, S., Mazloff, M., Newman, L., Thompson, A. F., Thomson, J., Ward, B., Du Plessis, M. D., Kent, E. C., Girton, J., Gregor, L., Petra, H., Hyder, P., Pezzi, L. P., De Souza, R. B., Tamsitt, V., Weller, R. A., & Zappa, C. J. (2019). Constraining Southern ocean air-sea-ice fluxes through enhanced observations. Frontiers in Marine Science, 6(JUL), 1–10. https://doi.org/10.3389/fmars.2019.00421

Turner, J., Hosking, J. S., Bracegirdle, T. J., Marshall, G. J., & Phillips, T. (2015). Recent changes in Antarctic Subject Areas: Philosophical Transaction of The Royal Society A, 373(2045), 1–12.

Turner, J., Orr, A., Gudmundsson, G. H., Jenkins, A., Bingham, R. G., Hillenbrand, C. D., & Bracegirdle, T. J. (2017). Atmosphere-ocean-ice interactions in the Amundsen Sea Embayment, West Antarctica. Reviews of Geophysics, 55(1), 235–276. https://doi.org/10.1002/2016RG000532

Verheugen, G. (2005). European commission. Pharmaceuticals Policy and Law, 6, 1–2. https://doi.org/10.4324/9781849776110-28

Visbeck, M. (2009). A station-based southern annular mode index from 1884 to 2005. Journal of Climate, 22(4), 940–950. https://doi.org/10.1175/2008JCLI2260.1

Von Engeln, A., & Teixeira, J. (2013). A planetary boundary layer height climatology derived from ECMWF reanalysis data. Journal of Climate, 26(17), 6575–6590. https://doi.org/10.1175/JCLI-D-12-00385.1

Walters, D., Baran, A. J., Boutle, I., Brooks, M., Earnshaw, P., Edwards, J., Furtado, K., Hill, P., Lock, A., Manners, J., Morcrette, C., Mulcahy, J., Sanchez, C., Smith, C., Stratton, R., Tennant, W., Tomassini, L., Van Weverberg, K., Vosper, S., … Zerroukat, M. (2019). The Met Office Unified Model Global Atmosphere 7.0/7.1 and JULES Global Land 7.0 configurations. Geoscientific Model Development, 12(5), 1909–1963. https://doi.org/10.5194/gmd-12-1909-2019

Wang, X., & Wang, K. (2016). Homogenized variability of radiosonde-derived atmospheric boundary layer height over the global land surface from 1973 to 2014. Journal of Climate, 29(19), 6893–6908. https://doi.org/10.1175/JCLI-D-15-0766.1

Wyngaard, J. C. (2004). Toward numerical modeling in the “Terra Incognita.” Journal of the Atmospheric Sciences, 61(14), 1816–1826. https://doi.org/10.1175/1520-0469(2004)061<1816:TNMITT>2.0.CO;2